# APPLICATION OF THE LATTICE BOLTZMANN METHOD TO CAPILLARY SEALS AND DYNAMIC PHASE INTERFACES

A Dissertation

Presented to the Faculty of the Graduate School

of Cornell University

In Partial Fulfillment of the Requirements for the Degree of

Doctor of Philosophy

by

Caroline S. Poyurs

February 2010

# APPLICATION OF THE LATTICE BOLTZMANN METHOD TO CAPILLARY SEALS AND DYNAMIC PHASE INTERFACES

Caroline S. Poyurs

Cornell University 2010

The exact nature of the seals maintaining abnormally pressured compartments in sedimentary basins is not well understood, despite decades of research. We use the Lattice Boltzmann method for immiscible fluids to investigate a novel idea that capillary pressures alone are able to seal in the observed abnormal pressures. A capillary seal forms when a non-wetting fluid phase is generated within or introduced into grain sized layered sediment and the pressure drop across the coarse/fine interface is less than the capillary pressure. For such seals to maintain abnormal pressures, both phases must be blocked, the capillary pressure drops must be accumulative over many fine/coarse interfaces and the seals must be able to re-form after rupture. We show all three to be true, and hence lay the numerical foundation for the validity of capillary seals.

Lattice Boltzmann Method showed itself to be applicable to other problems of interest. The morphology of the meniscus between wetting and non-wetting fluids in a capillary tube when the fluids are in motion is controversial, for example. We also encountered instabilities and limitations in code as originally implemented. We investigated and instituted methodologies which drastically reduce the instabilities and worked around the encountered limitations.

# BIOGRAPHICAL SKETCH

Caroline S. Poyurs was born in London in 1975. After obtaining five 'A' levels in secondary school, she attended Cambridge University, reading Natural Sciences with a specialty in Physics. As part of the Natural Sciences curriuculum, Caroline choose to explore three other science courses. In addition to Chemistry and Math, she chose to explore Geology. She discovered that she loved Geology and realized that she eventually wanted to apply the physics to it. After graduating Cambridge in 1997 and teaching physics in Uganda, Caroline started a Ph.D. in Geophysics at Cornell University. During the pendency of her Ph.D., Caroline served as a Quality Analyst and subsequently a Validation Engineer at Exa Corporation, the leading provider of Lattice Boltzmann based digital wind tunnel software to the automotive industry.

Caroline steadily completed her Ph.D. every night after a full day's work and mothering three children, crowning her effort over the eight weeks of summer in 2009 when all the children went to camp.

To my family – to those who have done all they can to help me become a PhD:

My husband, Yeshaya

My mother, Sandra

Mt Grandmother, Mildred

My mother in law, Martha (“Mu”)

My daughters, Bracha, Shira and Batya

# ACKNOWLEDGMENTS

I would like to thank the Gas Research Institute and Global Basins for all of their financial support over the first five and half years. I'd especially like to thank my advisor Professor Larry Cathles, who was always available to discuss problems and to question me. Given that neither of us knew the Lattice Boltzmann Method existed when we started the thesis, I am all the more appreciative of his thoughtful and perceptive advice. Larry is indefatigable and his enthusiasm infectious. Thank you. I would like to thank my husband, for being my sounding board for many of the ruts that my PhD got into, for putting up with "I'm doing a PhD, sorry no family weekend trips away" and for then being the most sensitive diplomat in getting me to finish. I would like to thank my mother, grandmother and mother-in-law for being so supportive and thank my wonderful and special children, each of whom have enhanced my life indescribably. I would like to thank my colleagues at Exa Corp, from whom I again learnt the meaning of academic excellence, especially Hudong Chen, who tirelessly introduced me to the leaders of the Lattice Boltzmann field and gave me constant support for finishing up. I would also like to thank Adrienne Brown, without whom the final eight week push would have never had occurred.

Finally, throughout my time at Cornell and beyond, I have had the opportunity to meet and discuss problems with some outstanding people – all of whom have helped me tremendously, they are: Donald Turcotte, Bruce Boghansian, Jen Wang, Daniel Rothman, Rolf Verberg, Jean Yves Parlange, Chuck Alexander, Zhou Yong and Rick Shock.

# TABLE OF CONTENTS

# LIST OF FIGURES



**Figure 2.13:** The effect on wettability of decreasing the virtual non-wetting mass on solid nodes……..……...…….. 65

# LIST OF TABLES

# Chapter 1. Introduction

## 1.1 Background

After a decade of observation, Bradley and Powley [1] of Amoco formally asked the Gas Research Institute (GRI) to investigate the causes of pressure compartments in basins [2]. Pore fluids within these compartments maintain hydrostatic pressures which are under-pressured or over-pressured with respect to hydrostatic and different from the pressures in adjacent compartments. In order to preserve non-hydrostatic fluid pressures over millions of years the boundaries or seals that surround the pressure compartments must have permeabilities less than $10^{-23}$ $m^2$ [3]. Few lithologies have permeabilities this low, and some seals cross quite permeable lithologies.

In 1991 Cathles [4] proposed that capillary forces at fine-coarse interfaces produces the compartment seals and obtained funding from the Gas Research Institute to study the possibility. With this funding, an experiment was undertaken in 1996 by Shosa [5] to test the capillary seal hypothesis. This experiment shows that the flow of both hydrocarbon and aqueous fluids could be blocked in a porous media consisting of alternating fine and coarse-grained layers. The experimental pressure drops were additive across multiple layers and large enough that seals could easily form in common grain size layered sediments. Numerical modeling of the blockage phenomena proved difficult using standard techniques [6]. For this reason, it was decided to investigate immiscible fluid flow simulation using the Lattice Gas Automata method (LGA) and the Lattice Boltzmann Method (LBM). These methods have proven capable of addressing pore scale fluid phenomena that are very difficult to observe in the laboratory or model with continuum mechanical models.

As this thesis project developed we became aware that the method might be applied to other problems of interest. The morphology of the meniscus between wetting and non-wetting fluids in a capillary tube when the fluids are in motion is controversial, for example. The Lattice Boltzmann Method might be used to investigate this phenomenon. We also encountered instabilities and limitations in code as originally implemented. We investigated and instituted methodologies which drastically reduce the instabilities and work around the encountered limitations. This is all discussed in Chapter 2.

In this chapter, we first briefly review the evidence for and the characteristics of pressure compartments and then describe the capillary sealing hypothesis.

## 1.2 Pressure Compartmentation

In the 1960's and 1970's drilling engineers encountered pressures deep in basins that were either too high or low to be hydrostatic. It was found that pressure in many basins typically changes from normal to abnormal at ~3km depth. In some basins such as the Anadarko [7], the pressure returns to normal at depths of ~ 5-7km. In 1975 John Bradley [1] of Amoco suggested that abnormal pressures such as this were confined by seals surrounding the abnormally pressure zone. A good overall summary is published by Hunt [8].

Examples of pressure compartmentation in the Anadarko Basin are shown in Figures 1 and 2. This pressure data was analyzed and screened as part of a collection of over 28,400 pressure measurements. These measurements were collected from a variety of methods including: single zone completions or drill stem tests, tests of adequate duration and fluid recovery, and well-head shut in pressures measured after adequate shut-in durations. In both figures there is a rapid increase in fluid pressure

with respect to depth at approximately 3km. The pressure transition is normally only a few km thick, with pore fluids typically increasing to near lithostatic pressures at the base of the pressure transition. Within and below the transition hydrostatic pressure is elevated but segmented by many minor seals. The hydrostatic pressure is indicated in Figure 1 and 2 by pressure legs that parallel the hydrostatic gradient. These are offset by seal legs where the pressure increases rapidly with depth. Pressure measurements are indicated by data points. From such data it was concluded that pressure compartmentation occurs on many scales. Within compartments there are smaller compartments maintaining different degrees of overpressures. In 1990 Powley [9] documented that over 80% of the world's oil basins show some degree of pressure compartmentation, and that most of the world's oil was generated within over-pressured compartments.

Furthermore, it is known that pressure compartments exist for geologically extensive periods of time. Over-pressure compartments in the Anadarko basin, for example, have survived over 250 Myr [3]. There are many theories as to how the strata became impermeable [10-12]. The generation of hydrocarbons [11-13] and tectonic compression [1,14] have all been suggested. Good references are offered by Ortoleva et. al. [11], Osborne and Swarbrick [12], Mouchet and Mitchell [15] and Sibson et. al. [16].

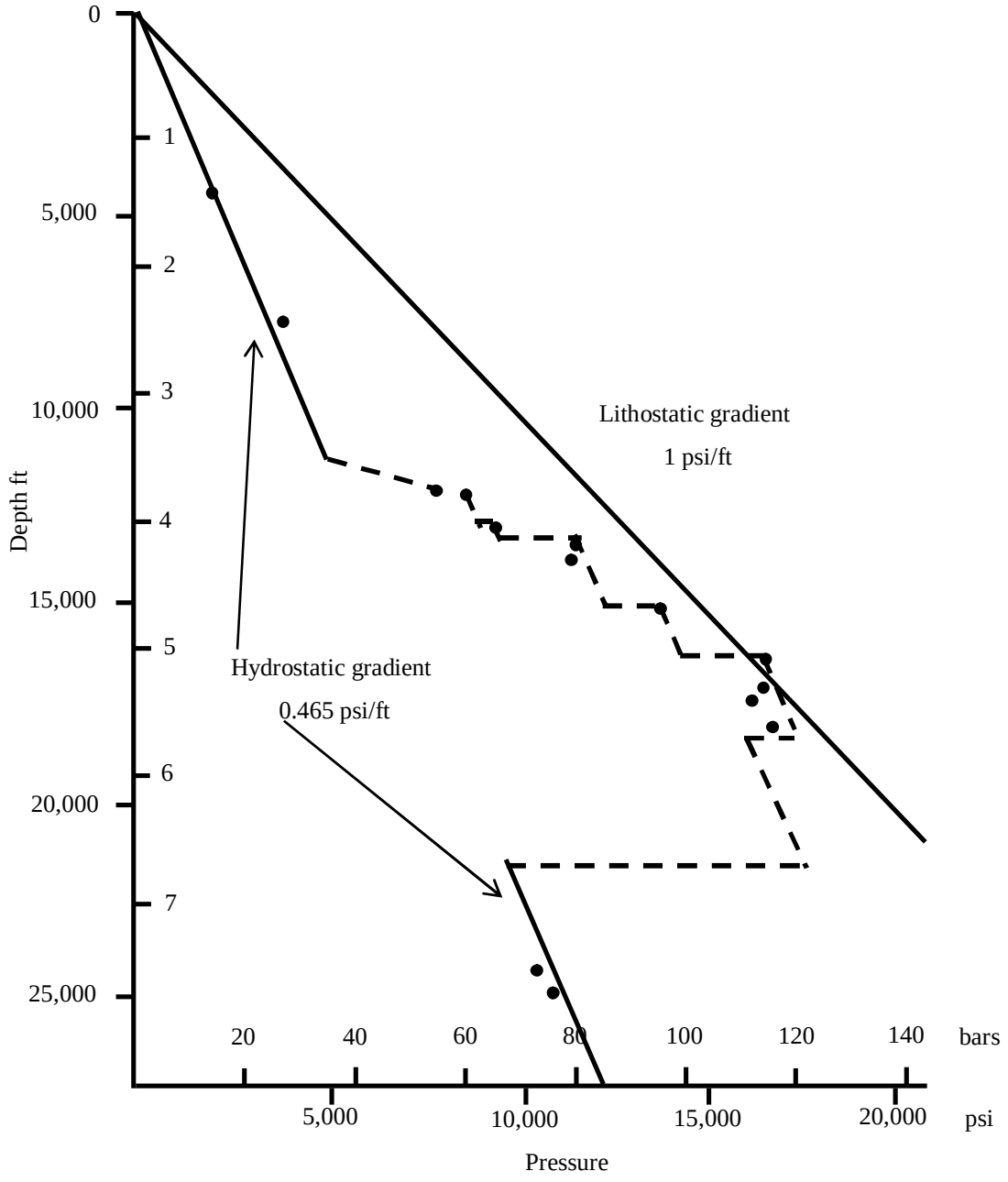


Figure 1.1: Example of a pressure depth graph taken from the Anadarko basin, indicating the presence of an over-pressured compartment [7].

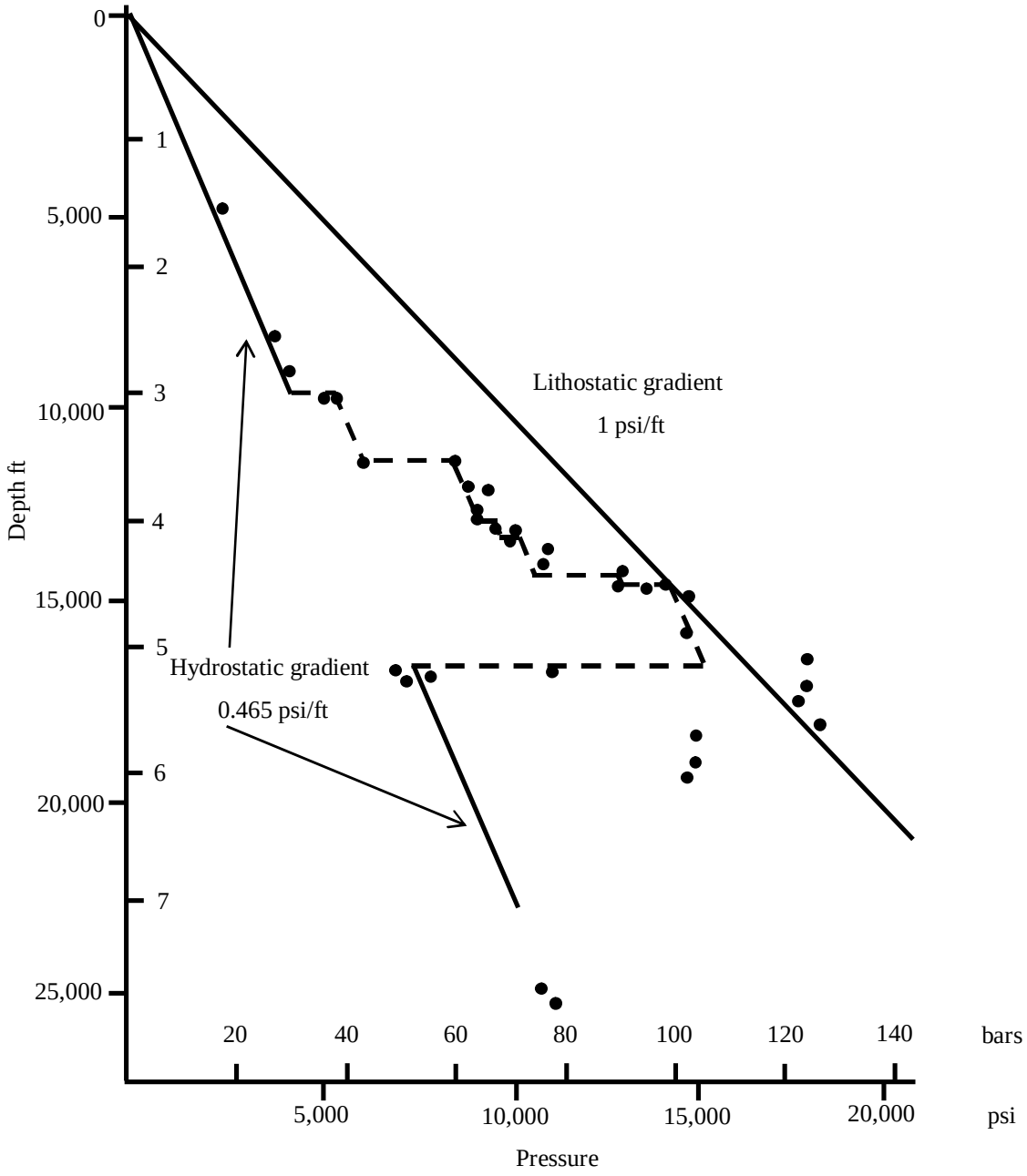


Figure 1.2: Another example of a pressure depth graph taken from the Anadarko basin, indicating the presence of an over-pressured compartment [7].

## 1.3 Compartmental Seals

The top and bottom seals of a compartments are commonly assumed to be very low permeable strata, such as an evaporate or shale [7,17]. The lateral seals of compartments are most often found associated with vertical or high angle faults [2,9,11], although these laterals seals have also been found in the absence of any faulting [11]. Other than very low permeability, seals do not have consistent lithologic properties [9]. Seals often cut across regional stratigraphy [7] which brings in to question the idea that a single low permeability lithologic unit could be the seal. According to Deming [3], for seal to exist for the observed time scales it would need a permeability of $10^{-23}$ to $10^{-25}$ $m^2$. Shale is thought to have permeabilities in the range $10^{-16}$ to $10^{-23}$ $m^2$ [16,17] based on laboratory measurements and $10^{-18}$ to $10^{-19}$ $m^2$ [18] based on in-situ measurements. The range of required seal permeabilities is lower than the lowest laboratory measurements for shale, and likely to be several orders of magnitude lower than average shale permeabilities measured in situ. Seals are known to rupture and re-heal periodically [8], and the top of overpressure must migrate upwards as sedimentation occurs if it is to be commonly encountered at ~ 3km depth [11,19]. Neither of these characteristics could be accommodated if the seal was simply a single low-permeability strata.

## 1.4 Capillary Forces as a Sealing Mechanism

The idea behind capillary forces as a sealing mechanism is simple. Once there are two immiscible phases within a layered sediment, provided that the pressure is less than the capillary entry pressure, a seal is formed. The non-wetting phase can be thought of as plugging each pore, preventing the flow of both the wetting and non-wetting phases, as illustrated in Figure 1.3.

Capillary Seals are not a novel idea. Soil scientists have studied capillary sealing as the cause of lateral diversion of downward percolating water [20-24]. Petroleum geologists have also observed that capillary seals trap hydrocarbons in basins [25,26]. However the concept has not been applied to over-pressured compartments, perhaps because the capillary pressure of a single layer of pores is insignificant compared to the overpressures maintained in compartments. However, if these pressures are additive over many coarse/fine grain layers, then the overall capillary pressures would be great enough to contain the observed overpressures.

Petroleum is generated as a super-critical mixture which separates into distinct oil and gas phases when temperature and pressure are reduced as the petroleum migrates upwards. This typically occurs in sedimentary basins at a depth of ~ 3km. Since the gas/water interfacial tension is about twice that of the oil/water interfacial tension, the capillary entry pressure for a given pore doubles once the gas exsolves. The depth at which phase separation occurs would be a logical place for capillary seals to form and it has been observed that this phase separation is broadly coincident with the top of overpressure compartments in the Gulf of Mexico [27].

A capillary seal can rupture when the pore pressure of the compartments becomes greater than the cumulative capillary entry pressure of the seals. The seal reforms once this pressure is reduced. Adding sediment to a basin, oil maturation, compaction and thermal expansion of water and gas all provide mechanisms for generating pressure. Capillary seals could occasionally rupture but still retain elevated pressures below. Furthermore, this periodic rupture and release allows the top seal to migrate upward, when the capillary seal is broken and immiscible phases escape. When the pressure is reduced so that it is less than the sum of the capillary entry pressures across all the fine-coarse interfaces in the seal, the seal will re-form.

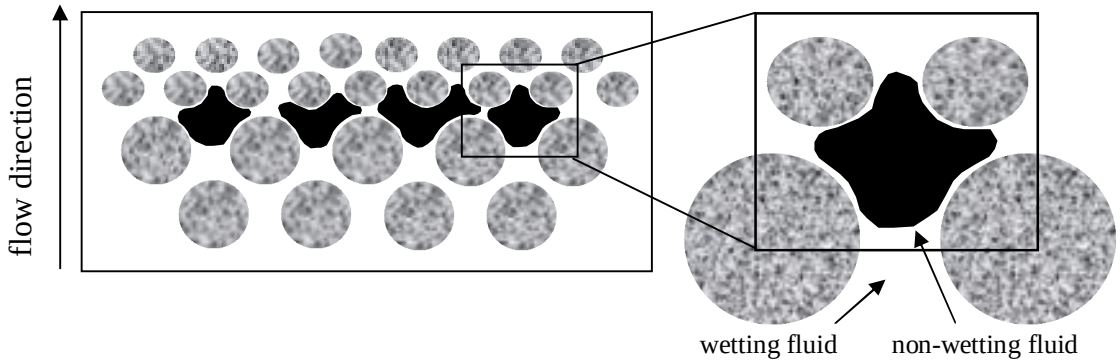


Figure 1.3: Idea behind the capillary seal: The capillary entry pressure for the non-wetting phase (black) is greater than the pressure drop across a pore. The non-wetting phase cannot enter the pore and the flow of both the non-wetting (gas) and wetting fluids is stopped.

## 1.5 Thesis Outline

The major objective of this thesis was to investigate capillary sealing using the Lattice Boltzmann Method. The intention was to address such matters as how much gas (non-wetting fluid) is required to form a seal, how a seal fails and leaks wetting and non-wetting fluids when the capillary entry pressure is exceeded, and how a seal re-forms when the pressure is reduced.

REFERENCES


1. Bradley, J.S., *Abnormal Pressure Formation.* AAPG Bull., 1975. 59(6):p.957-973.

2. Powley, D.E., *Abnormal Pressure Seals*. Gas Research Institute Gas Sands Workshop. 1987. Chicago.

3. Deming, D., *Factors Necessary to Define a Pressure Seal*. AAPG Bull., 1994. 78(6):p.1005-1009.

4. Cathles, L.M., *Gas Transport of Oil: It's Imprint on Sealing and the Development of Secondary Porosity.* 1991. Gas Research Institute.p.23.

5. Shosa, J., *Overpressure in Sedimentary Basins: Mechanisms and Mineralogical implications,* in Department of Earth and Atmospheric Sciences. 2000. Cornell University, Ithaca.

6. Erendi, A. *Computer Simulation of Geological Processes*, in Geological Sciences, 2000. Cornell University, Ithaca: p.174-202.

7. Tigert, V. and Z. Al-Shaieb, *Pressure Seals: Their Diagenic Banding Patterns.* Earth-Sci Reviews., 1990.29: p.227-240.

8. Hunt, J.M., *Generation and Migration of Petroleum from Abnormally Pressured Fluid Compartments.* AAPG Bull.,1990. 75:p.1-12.

9. Powley, D.E., *Pressures and Migration of Petroleum from Abnormally Pressured Fluid Compartments.* AAPG Bull., 1990. 29(1-4):p.215-226.

10. Bredehoeft, J.D., and B.B. Hanshaw, *On Maintenance of Anomalous Fluid Pressures 1. Thick Sedimentary Sequences.* Geological Society of America Bulletin, 1968. 79(9):p.1097-1106.

11. Ortoleva, P., Z. Al-Shaieb and J.Puckette, *Genesis and Dynamics of Basin Compartments and Seals.* Am. J. Sci., 1995. 295:p.345-427.

12. Osborne, M.J. and R.E. Swarbrick, *Mechanisms for Generating Overpressure in Sedimentary Basins: A Re-evaluation.* AAPG Bull., 1997. 81(6):p.1023-1041.

13. Holm, G., *How Abnormal Pressures Affect Hydrocarbon Exploration*, Oil and Gas J., 1998. 96(2):p.79-84.

14. Van Ruth, P. et. al., *The Origin of Overpressure in 'Old' Sedimentary Basins: An Example From the Cooper Basin, Australia.* GeoFluids, 2003. 3(2):p.125-131.

15. Mouchet, J.P. and A. Mitchell, *Abnormal Pressures While Drilling: Origins-Predicitons-Detection-Evaluation.* in Manuels Technique Elf Aquitaine, E.A. Editions, Editor, 1989. Boussens: p.264.

16. Sibson, R.H., J.M. Moore and A.H. Rankin, *Seismic Pumping – A Hydrothermal Fluid Transport Mechanism.* J. Geol. Soc. London, 1975. 131:p.653-659.

17. Perrodon, A., *Dynamics of Oil Gas Accumulations,* ed. E. Aquitaine, 1983. Paris:p.368.

18. Brace, W.F., *Reply: Discussion on "A Numerical model of Compaction Driven Groundwater Flow and Heat Transfer and its Application to the Paleohydrology of Intracratonic and Sedimentary Basins".* J. of Geophysical Research, 1988. 93:p.3500-3504.

19. Cathles, L.M., *Capillary Seals as a Cause of Pressure Compartmentation in Sedimentary Basins,* in GCSSEPM Foundation 21st Annual Research Conference: Petroleum Systems of Deep-Water Basins. 2001.

20. Steenhuis, T. and J. Y. Parlange, *Comment on the Diversion Capacity of Capillary Barriers.* Water Resources Research, 1991. 27(8):p.2155-2156.

21. Steenhuis, T et. al., *Flow Regimes in Sandy Soils with Inclined Layers,* in Tenth Annual American Geophysical Union Hydrology Days. 1990. Colorado State University, Fort Collins.

22. Ross, B., *The Diversion Capacity of Capillary Barriers.* Water Resources Research, 1990. 26(10):p.2625-2629

23. Miyazaki, T., *Water Flow in Unsaturated Soil in Layered Slopes.* J. of Hydrology, 1998. 102:p.201-214.

24. Kung, K.J.S., *Preferential Flow in a Sandy Vadose Zone: 1. Field Observations.* Geoderma, 1990. 46:p.51-58.

25. Schowalter, T.T., *Mechanics of Secondary Hydrocarbon Migration and Entrapment.* AAPG Bull., 1979. 64(5):p.723-760.

26. Berg, R.R., *Capillary Pressures in Stratigraphic Traps.* AAPG Bull., 1975. 59(6):p.939-956.

27. Meulbroek, P. *Hydrocarbon Phase Fractionation in Sedimentary Basins*, in Geological Sciences. 1997. Cornell University, Ithaca:p.345.

# Chapter 2. The Lattice Boltzmann and Lattice Gas Automata Methods in Fluid Dynamics

## 2.1 Introduction

"We have noticed in nature that the behavior of a fluid depends very little on the nature of the individual particles in the fluid. For example, the flow of sand is very similar to the flow of water or the flow of a pile of ball bearings. We have therefore taken advantage of this fact to invent a type of imaginary particle that is especially simple for us to simulate. This particle is a perfect ball bearing that can move at a single speed in one of six directions. The flow of these particles on a large enough scale is very similar to the flow of natural fluids."

*Richard Feynman on explaining the lattice gas phenomena.*

The modeling of multiphase flow in porous media is central in numerous areas of science and industry. It controls oil and gas migration and recovery, temperature distribution in shallow geothermal systems, and influences volcanic eruptions and environmental remediation programs, for example. However, the numerical solution of the equation governing fluid flow, the Navier-Stokes equation, becomes difficult and computationally costly when more than one fluid and complex boundaries are involved.

In this chapter we introduce and illustrate two relatively new and computationally efficient methods which greatly simplify modeling flow in porous media. These methods are the Lattice Gas Automata method (LGA) and the Lattice Boltzmann Method (LBM). The Lattice Boltzmann Method evolved from the Lattice Gas Automata (LGA) method, which in turn evolved from the Cellular Automata method (CA). The CA method was introduced by Ulam and used by von Neumann in the 1940's [1, 2] to model self-replication. Subsequently, the method was found to be applicable to a wide variety of problems in communication, computation, growth and

competition. In 1968, Kadanoff and Swift [3] used the CA method to model sound waves, but it was not until 1976 that Hardy, de Pazzis and Pomeau [4] suggested using the CA method to model fluid flow.

The efficiency of these methods stems from the fact that they are based upon a numerical ideal gas, rather than a discretized (finite difference or finite element) version of the Navier Stokes equation. The methods are simple because they go back to the basics of particle motion and handle boundaries the way nature does, with a large number of trials by many particles.

Our interest here is to explain the methodologies to a reader not familiar with these methods in sufficient detail that their essential features can be understood. In this chapter we will first describe the LGA method, then the LBM. We present additional schemes we introduced to broaden and stabilize the code. We then illustrate and explain some of the phenomological issues we found. Finally we present some simple validation tests. Detailed derivations are not repeated. They can be found in the following citations [4-19].

## 2.2 The Lattice Gas Automata Method

### A. Introduction

In the Hardy, de Pazzis and Pomeau Lattice Gas Automata method (known as the HPP after the author's initials) the links between lattice nodes form a square grid as shown in Figure 2.1. In the HPP method, each node can have up to 4 particles and these particles reside on the links surrounding the node. No more than one particle may reside on any link at any time. In addition to belonging to a node, each particle has a unit velocity defined by the link on which it resides. The direction of the velocity is always away from the particle's node.

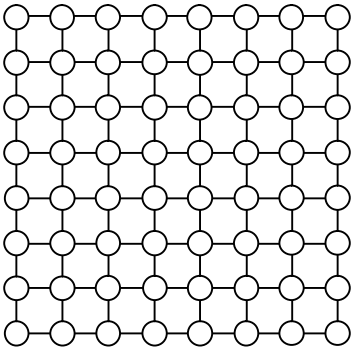

Figure 2.1: The HPP lattice.

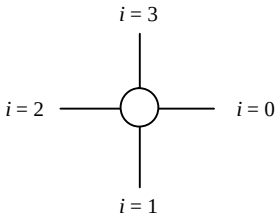


Figure 2.2: A single HPP node showing the indices of the links.

The particle mass and momentum of a node are defined as follows:

$$\rho = \sum_{i=1}^{b} n_i \qquad \ldots(2.1)$$

$$\rho u_\alpha = \sum_{i=1}^{b} n_i e_{i\alpha} \; . \qquad \ldots(2.2)$$

In these equations, $\rho$ is the particle mass at a node, $i$ is the link number (See Figure 2.2), b is the total number of links around a node (4 in the HPP case), $u_\alpha$ is the velocity (magnitude 1 only for the HPP lattice) in the $\alpha^{th}$ direction, $\rho u_\alpha$ is the momentum in the $\alpha^{th}$ direction, and $e_{i\alpha}$ gives the velocity of the particle on the $i^{th}$ link in the $\alpha$ direction ($\alpha$ may be x or y in 2D). For the HPP lattice the $e_{i\alpha}$ are given in Table 2.1 below. If there is a particle on the $i^{th}$ link of a node, $n_i$ is 1; if there is no particle residing on the $i^{th}$ link, $n_i$ is 0. Notice that Table 2.1 quantifies the convention that particle motion is always away from the node which owns the particle.

Generally the system is initialized such that the average number of particles residing at a node corresponds to a predefined nodal mass. Flow boundaries are usually taken to be periodic such that any particles leaving the grid are reintroduced into the other end of the grid. Supposed for example that grid has $L_x$ nodes in the x direction and $L_y$ nodes in the y direction, so the grid dimensions are $\{L_x, L_y\}$. Particles moving in the positive x-direction at $x = L_x$ are transferred to inbound links at x = 0 at the next iteration. This is coded such that the nodes at $x = L_x$ see the nodes at x = 0 as their immediate neighbors.

Table 2.1: Individual values of $e_{i\alpha}$ for the HPP lattice.

| | Coordinate (α) | |
|---|---|---|
| Link index (i) | *X* | *Y* |
| 0 | 1 | 0 |
| 1 | 0 | -1 |
| 2 | -1 | 0 |
| 3 | 0 | 1 |

The particles are moved in two computational stages, propagation and collision. During the propagation step, the particles on the links surrounding a node are moved along the link to the adjacent node. This is illustrated in the first pair of columns in Table 2.2. In the collision step, the particles are redistributed according to predefined "collision rules" that conserve momentum and mass. Only one collision rule is possible in the HPP lattice (second row of Table 2.2), since the possible particle motions can be re-arranged in only one way that conserves mass and momentum.

Kinetic equations can be written for the HPP lattice which allow their application to other lattice types. For example a propagation equation can be written which shows where a particle on the $i^{th}$ link at time t will be at time t+1:

$$n_i(\bar{x} + c_i, t+1) = n_i(\bar{x}, t) \qquad \ldots.(2.3)$$

Here $\bar{x} = \begin{Bmatrix} x \\ y \end{Bmatrix}$ is the position of the node analyzed. $n_i(\bar{x}, t) = 1$ if the node at position $\bar{x}$ has a particle on the $i^{th}$ link at time t. Otherwise $n_i(\bar{x}, t) = 0$. If the node at position

$\bar{x}$ has a particle on its $i^{th}$ link at time t, this particle will reside on the $i^{th}$ link of the node at position $\bar{x} + c_i$ at time t+1, where $c_i = \begin{Bmatrix} e_{ix} \\ e_{iy} \end{Bmatrix}$. For example, as can be seen from Figure 2.2, if the particle is on the 0th link ($i$ = 0) at time t, then $\begin{Bmatrix} e_{0x} \\ e_{0y} \end{Bmatrix} = \begin{Bmatrix} 1 \\ 0 \end{Bmatrix}$, and the particle will propagate to the next node in the x direction at time t+1: $n_0(\begin{Bmatrix} x \\ y \end{Bmatrix} + \begin{Bmatrix} 1 \\ 0 \end{Bmatrix}, t+1)$. In other words, the particle moves onto the 0th link of the node at $\bar{x} = \begin{Bmatrix} x+1 \\ y \end{Bmatrix}$.

The collision rule is applied using a collision operator. If particles reside on only the *i* and the *i + 2* links of a node, then the collision rule shown in Table 2.2 states that these links should be emptied and the particles transferred to the *i+1* and *i+3* nodes. The combined propagation and collision steps may be expressed in an evolution equation:

$$\Delta_i n = C_i(n) \qquad \ldots(2.4)$$

where $\Delta_i n$ denotes the change in $n_i$ affected by the collision operator, $C_i(n)$. The collision operator, $C_i(n)$, is defined for the HPP lattice as:

$$C_i(n) = n_{i+1} n_{i+3} (1 - n_i)(1 - n_{i+2}) - n_i n_{i+2} (1 - n_{i+1})(1 - n_{i+3}) \qquad \ldots.(2.5)$$

For example, in Table 2.2 after propagation we have a particle residing on the 0th and 2nd links and no particles on the 1st and 3rd links. Therefore: $n_0 = 1$; $n_1 = 0$; $n_2 = 1$; $n_3 = 0$, and the $C_i(n)$ in Eq. 2.5 have the following values:

$$C_0(n) = n_1 n_3 (1-n_0)(1-n_2) - n_0 n_2 (1-n_1)(1-n_3) = -1 \qquad \ldots.(2.5a)$$

$$C_1(n) = n_2 n_0 (1-n_1)(1-n_3) - n_1 n_3 (1-n_2)(1-n_0) = 1. \qquad \ldots(2.5b)$$

$$C_2(n) = n_3 n_1 (1-n_2)(1-n_0) - n_2 n_0 (1-n_3)(1-n_1) = -1 \qquad \ldots(2.5c)$$

$$C_3(n) = n_0 n_2 (1-n_3)(1-n_1) - n_3 n_1 (1-n_0)(1-n_2) = 1. \qquad \ldots(2.5d)$$

Applying these collision equations then removes particles from the $0^{th}$ and $2^{nd}$ links and adds them to the $1^{st}$ and $3^{rd}$ links, as illustrated in Table 2.2.

Table 2.2: Propagation and collision redistribution for the HPP lattice

The dark circle indicates which node "owns" the particles. The arrows indicate particles on a link and its velocity)

| | Propagation | | Collision | |
|---|---|---|---|---|
| Total Momentum | Before | After | Before | After |
| 1 | 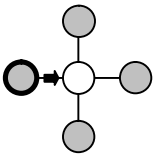 | 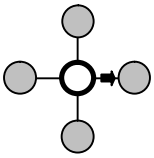 | No redistribution | 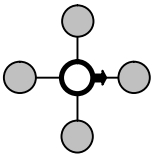 |
| 0 | 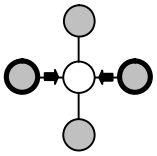 | 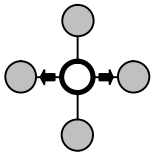 | 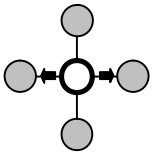 | 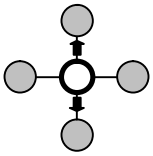 |

Table 2.2 continued

| | Propagation | | Collision | |
|---|---|---|---|---|
| Total Momentum | Before | After | Before | After |
| 1 | 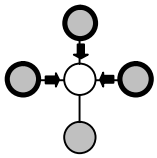 | 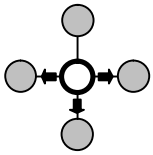 | No redistribution | 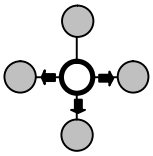 |
| 0 | 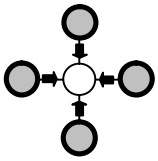 | 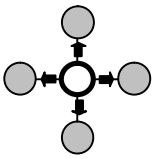 | No redistribution | 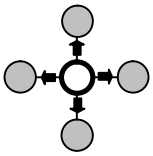 |

This type of CA method is known as Lattice Gas Automata (LGA). Through simulations, it has been shown that the HPP lattice can simulate sound waves and vorticity diffusion [20] [21]. However it cannot simulate general fluid flow as described by the Navier Stokes equation.

B. Rotational invariance of the HPP and FHP lattices

The limited functionality of the LGA method derives primarily from the fact that the HPP lattice does not have enough rotational degrees of freedom [13]. With only four directions of particle motion it is not possible to simulate flows described by the Navier Stokes equation. The LGA method really took off in 1986, when Frisch et. al. solved this problem [5, 22]. Frisch, Hasslacher and Pomeau [5] showed that a hexagonal lattice had sufficient rotational degrees of freedom [6] to simulate flow governed by the Navier Stokes equation.

They showed that in two dimensions, the six discrete directions of particle motion of the hexagonal lattice (rotations by a multiple of $2\pi/6$, or Z6 for short) can substitute for a continuum of directions. The 2D hexagonal lattice, shown in Figure 2.3, is known as the FHP lattice after Frisch, Hasslacher and Pomeau. The indexing convention for the links of a node on the FHP grid is shown in Figure 2.4. It was later shown that a 3D projection of the 4D Face Centered Hyper-Cubic (FCHC) lattice had sufficient rotational symmetry to solve three dimensional problems [23]. Collision and propagation rules for the first FHP lattice are given in Table 2.5.

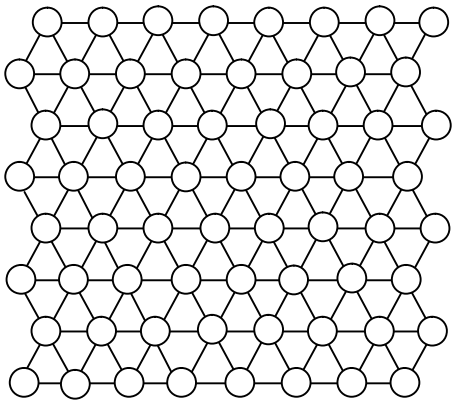

Figure 2.3: the FHP lattice.

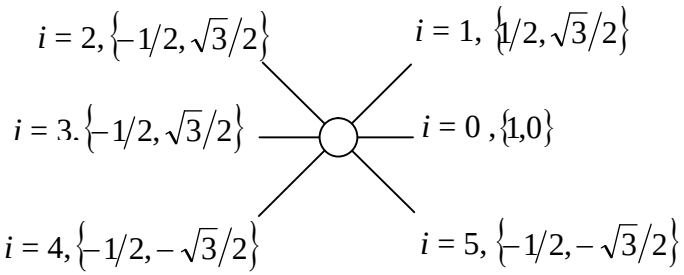


Figure 2.4: A single FHP node showing the indices of the links, and the momentum in the {x y} directions, given in curly brackets. The total momentum of all particles is 1.

C. Galilean invariance

The FHP lattice inherited other problems from the HPP lattice, which the increased rotational degrees of freedom did not solve. One problem is that LGA does not obey the principle of Galilean Relativity [6]. This principle says that everything is the same in a reference frame moving at a steady speed as in a reference frame at rest. In other words, the laws of motion are not affected by a frame of reference moving at a constant velocity. However, because the particles can have only a unit velocity, giving the entire grid a velocity of 1 will cause some particle velocities to equal 2, which is not possible within LGA rules.

The problem of Galilean invariance is solved by ensuring that the average particle velocity of the whole system is small. This velocity constraint is described in terms of the Mach number, M, where:

$$M = \bar{u}_\alpha / c_s \qquad \ldots.(2.6)$$

Here, $\bar{u}_\alpha$ is the average particle velocity in direction, α, and $c_s$ is the speed of sound for the lattice, where the speed of sound is defined by:

$$c_s = c/\sqrt{D}\,. \qquad \ldots(2.7)$$

Where D is the spatial dimension, which in this case is 2 for the 2D grid, and c is the velocity of a particle, in this case 1. The average velocity of all particles in any direction has to be much smaller than the speed of sound on the grid ($M << 1$), or:

$$\bar{u}_\alpha << \frac{c}{\sqrt{D}} = \frac{1}{\sqrt{2}} \qquad \text{for a 2D grid.} \qquad \ldots(2.8)$$

Pressure in a lattice gas can be defined from the speed of sound. In an ideal gas the speed of sound, $c_s$, is related to pressure, P, and density:

$$P = \rho c_s^2\,. \qquad \ldots(2.9)$$

Since in the FHP system c = 1 and $c_s = 1/\sqrt{2}$ in two dimensions, the lattice gas pressure in two dimensions is related to particle density: $P = \frac{\rho}{2}$.

D. Spurious conservations

Spurious conservations are physical artifacts produced by the discreteness of the underlying lattice. An example of such an artifact on the HPP lattice is that the numbers of particles traveling in the vertical and horizontal directions are always conserved. This is not true for a real fluid.

Once a spurious conservation is recognized, it is often easily resolved. By allowing a three-particle collision in the FHP lattice, as shown in the 8th row of Table 2.5, the spurious conservation of the same mass traveling in the vertical and horizontal directions in the HPP lattice was removed. Similarly solved was a spurious conservation associated with the FHP lattice known as "pair conservation". Any pair of particles coming into a node in opposite directions would always leave the node traveling in opposite directions. Adding rest particles and allowing collisions with three particles solved this type of spurious conservation [24-25]. Many spurious conservations were found to have a negligible effect in numerical simulation and they thus could be ignored.

E. Fluid viscosity

An important theoretical proof of the validity of the LGA method was presented in 1986 by Frisch et. al [5]. Using the conservation equations of mass and momentum, and applying perturbation theory on $n_i$, around $n_i^{eq}$, (the equilibrium distribution for a node), Frisch et. al. derived the equations of motion for the FHP method. These equations look exactly the same as the Euler and Navier Stokes equations except for a Galilean invariant prefactor [11]. This laid the theoretical foundation for the simulation of any fluid flow where viscous forces dominate, which is equivalent to the condition that the Galilean invariance term is insignificant. Furthermore, theoretical values of some of the transport coefficients were derived from their equations. For example, from the comparison of the macroscopic Navier Stokes equation and its analogue for the FHP lattice, a expression for kinematic viscosity was found [5]:

$$\upsilon = \frac{1}{28(\rho/7)[1-\rho/7]\left[1-8(\rho/7)\left(\frac{(1-\rho/7)}{7}\right)\right]} - \frac{1}{8} \qquad \ldots(2.10)$$

F. Collision rules, mass and momentum conservation for the FHP lattice

The full range of the collision rules for the FHP lattice are shown in Table 2.5. The procedure for simulating slow fluid flow on the FHP grid is similar to that described already for the HPP grid. The particles on each link are propagated to the adjacent node and the collision rules applied. Modifications are made at solid boundaries, which allow viscous effects. Other modifications allow inclusion of body forces and more than one fluid phase. Tables 2.3, 2.4 and 2.5 illustrate how mass and momentum are calculated and conserved in collision redistributions. For a given mass and momentum combination, if there is more than one post-collisional configuration and no other considerations, such as immiscibility, then the final configuration is randomly chosen. This possible configuration set also includes the original configuration. If there are two fluids, then the configuration which moves particles towards their own kind the most is applied. Forces are dealt with in Section G.

Table 2.3: Particle motions before and after a simple collision

| Total Momentum | Before | After |
|---|---|---|
| 1 | 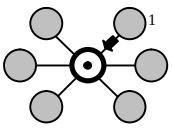  | 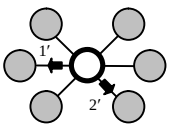  |

Table 2.4: Momentum in x and y directions for case shown in Table 2.3

| Particle # | 1 | 2 | Total momentum |
|---|---|---|---|
| momentum before collision | $\begin{Bmatrix} -1/2 \\ -\sqrt{3}/2 \end{Bmatrix}$ | $\begin{Bmatrix} 0 \\ 0 \end{Bmatrix}$ | $\begin{Bmatrix} -1/2 \\ -\sqrt{3}/2 \end{Bmatrix}$ |
| momentum after collision | $\begin{Bmatrix} -1 \\ 0 \end{Bmatrix}$ | $\begin{Bmatrix} 1/2 \\ -\sqrt{3}/2 \end{Bmatrix}$ | $\begin{Bmatrix} -1/2 \\ -\sqrt{3}/2 \end{Bmatrix}$ |

Table 2.5: The full range of the collision rules for the FHP lattice.

| | | Propagation | | Collision | |
|---|---|---|---|---|---|
| Total Momentum | row | Before | After | Before | After |
| 1 | 1 | 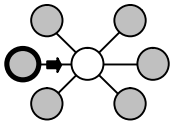 | 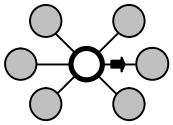 | No redistribution | 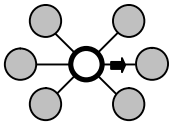 |

Table 2.5 continued

| | | Propagation | | Collision | |
|---|---|---|---|---|---|
| Total Momentum | row | Before | After | Before | After |
| 0 | 2 | 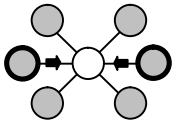 | 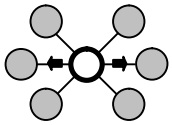 | 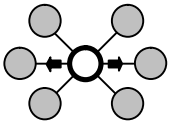 | 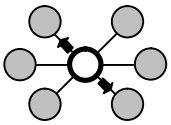 |
| 1 | 3 | 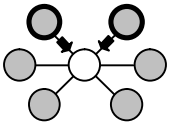 | 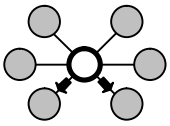 | No redistribution | 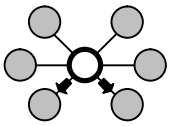 |
| 1 | 4 | 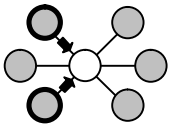 | 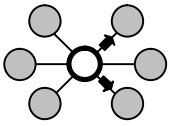 | 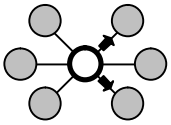 | 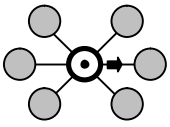 |
| 1 | 5 | 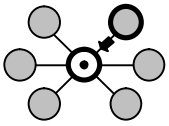 | 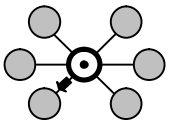 | 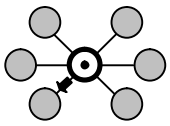 | 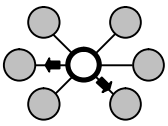 |

Table 2.5 continued

| | | Propagation | | Collision | |
|---|---|---|---|---|---|
| Total Momentum | row | Before | After | Before | After |
| 1 | 7 | 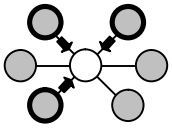 | 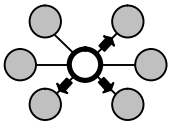 | 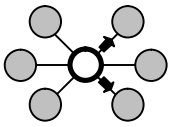 | 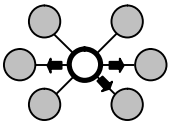 |
| 0 | 8 | 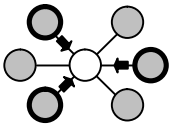 | 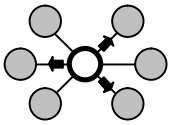 | 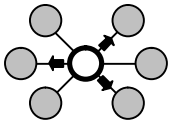 | 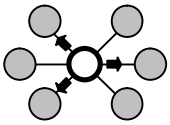 |
| 0 | 9 | 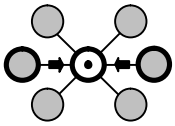 | 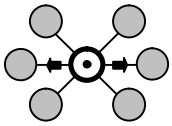 | 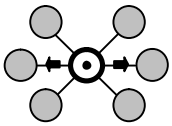 | 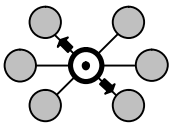 |
| $\sqrt{3}$ | 10 | 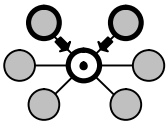 | 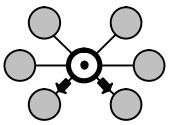 | No redistribution | 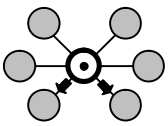 |

Table 2.5 continued

| | | Propagation | | Collision | |
|---|---|---|---|---|---|
| Total Momentum | row | Before | After | Total Momentum | row |
| 1 | 11 | 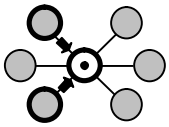 | 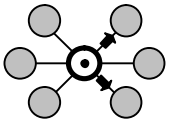 | No redistribution | 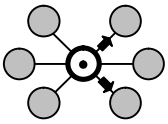 |
| 0 | 12 | 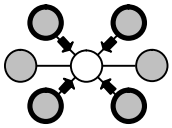 | 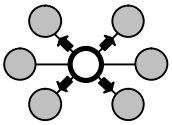 | 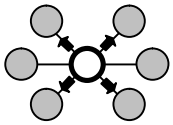 | 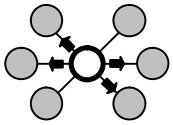 |
| $\sqrt{3}$ | 13 | 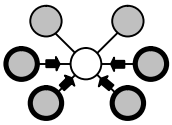 | 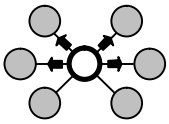 | No redistribution | 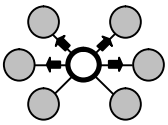 |
| 1 | 14 | 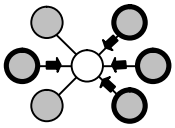 | 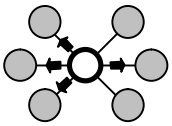 | 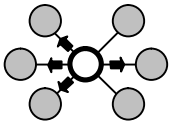 | 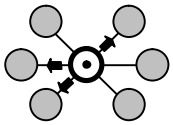 |

Table 2.5 continued

| | | Propagation | | Collision | |
|---|---|---|---|---|---|
| Total Momentum | row | Before | After | Total Momentum | row |
| 2 | 15 | 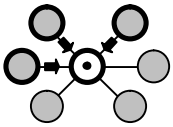 | 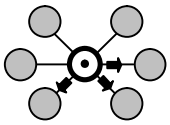 | No redistribution | 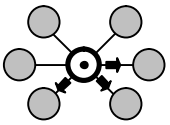 |
| 1 | 16 | 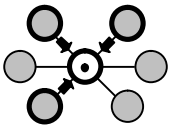 | 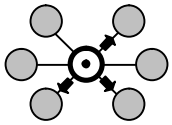 | 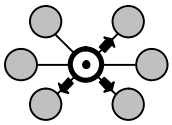 | 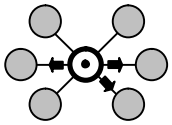 |
| 0 | 17 | 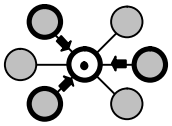 | 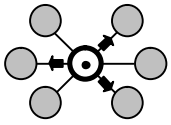 | 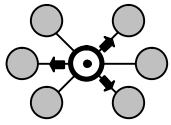 | 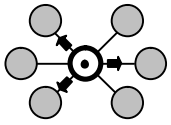 |
| 1 | 18 | 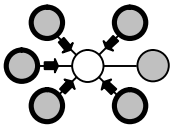 | 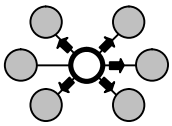 | No redistribution | 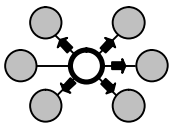 |

Table 2.5 continued

| | | Propagation | | Collision | |
|---|---|---|---|---|---|
| Total Momentum | row | Before | After | Total Momentum | row |
| 0 | 19 | 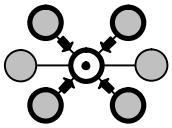 | 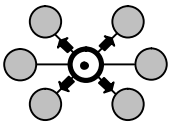 | 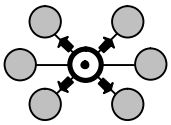 | 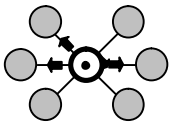 |
| $\sqrt{3}$ | 20 | 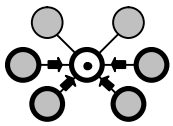 | 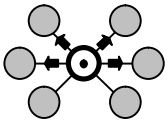 | No redistribution | 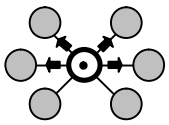 |
| 1 | 21 | 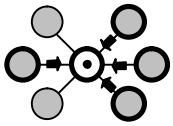 | 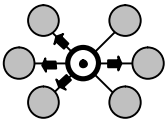 | No redistribution | 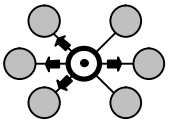 |
| 0 | 22 | 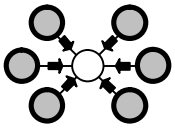 | 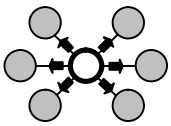 | No redistribution | 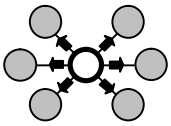 |

Table 2.5 continued

| | | Propagation | | Collision | |
|---|---|---|---|---|---|
| Total Momentum | row | Before | After | Total Momentum | row |
| 1 | 23 | 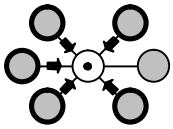 | 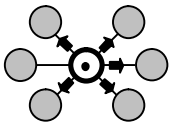 | No redistribution | 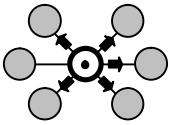 |
| 0 | 24 | 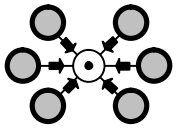 | 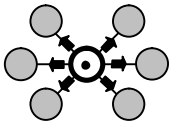 | No redistribution | 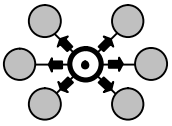 |

G. Body forces and pressure gradients

By Newtons's law, force is the change of momentum with time. Since the mass of each particle is 1 lattice mass unit, the momentum of a particle equals its velocity, and momentum change equals the change in particle velocity. A body force, *F*, can be applied to a particle by changing its velocity over a time step. The addition of momentum is illustrated for one particle velocity redistribution in Table 2.6 and 2.7. Table 2.8 shows all the ways the momentum at a node can be increased by one unit in the x-direction.

Table 2.6: Example of momentum change by application of a unit force in the x direction on the FHP lattice

| Total Momentum | Before | After |
|---|---|---|
| 1 | 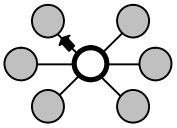 | 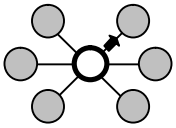 |

Table 2.7: Calculation of momentum change caused by application of a unit force in the x-direction on the FHP lattice

| momentum before force | momentum after force | Change in momentum |
|---|---|---|
| $\begin{Bmatrix} -1/2 \\ \sqrt{3}/2 \end{Bmatrix}$ | $\begin{Bmatrix} 1/2 \\ \sqrt{3}/2 \end{Bmatrix}$ | $\begin{Bmatrix} 1 \\ 0 \end{Bmatrix}$ |

Table 2.8: All the possible ways the x momentum of a particle can be increased by 1 unit

| Before | After |
|---|---|
| 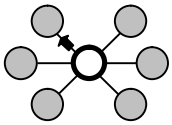 | 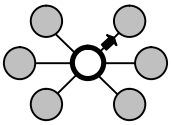 |
| 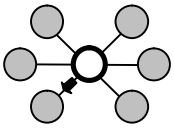 | 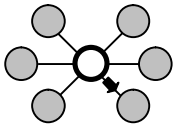 |
| 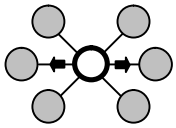 | 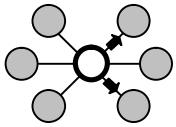 |
| 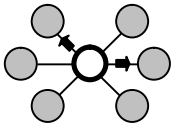 | 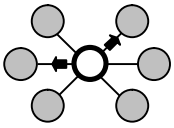 |
| 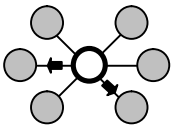 | 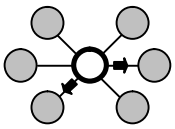 |

H. Immiscible fluids

Rothman and Keller [12] showed how an additional constraint on the collision rules allowed the simulation of the flow of two immiscible fluids. Their method was quickly applied to immiscible flow in porous media [26-28]. In their method the population of particles is split into two populations, labeled as 'blue' and 'red'. The propagation step is the same as before. Within the FHP system there is a choice of several post-collision particle configurations. Rothman and Keller chose the configuration that moved each particle towards the greatest density of its own kind. In their pivotal paper [12], they showed that the addition of this simple rule simulated fluid immiscibility. Their method also permitted the solid nodes to be assigned different degrees of wettability. By giving the solid nodes a predefined color density, particles of different color could be variably attracted to the solid. By changing this predefined color density, one could change the wettability of the solid surface.

I. Drawbacks of the LGA method

There remained some serious drawbacks to the LGA method, which we encountered as we sought to apply the method to cases of interest to us. The greatest problem is the statistical fluctuations associated with any particle method [13]. This problem was first recognized by Orszag and Yakhot [26] and later illustrated by numerical simulations [27]. Spatial and temporal averaging can reduce the statistical fluctuations, but this increases the computational time and computer memory requirements. The problem is magnified greatly in 3D simulations.

For these reasons, we turned to the Lattice Boltzmann Method (LBM), which removes statistical noise in a way that is as easily implemented and as effective in 3D as in 2D simulations.

## 2.3 The Lattice Boltzmann Method

### A. Introduction

The Lattice Boltzmann Method (LBM) was developed primarily to remove the inherent statistical fluctuations in the LGA simulations [17, 28]. Reducing these fluctuations by spatial and temporal averaging requires time and computational resources. To remove this noise more efficiently, McNamara and Zanetti [28] suggested using a distribution of particles on each link of each node, where the number of particles on the links of a node could be a fractional number of particles, $f_i(\bar{x},t) \equiv f_i$, where $f_i$ is the number of particles on the i$^{th}$ link of a node. Here the position of the node analyzed is $\bar{x} = \begin{Bmatrix} x \\ y \end{Bmatrix}$ in 2D or $\bar{x} = \begin{Bmatrix} x \\ y \\ z \end{Bmatrix}$ in 3D. Initially $f_i$ was thought to be the average number of integer particles on the i$^{th}$ link over a large number of trial iterations:

$$f_i = \langle n_i \rangle. \qquad \ldots(2.11)$$

Recalling the evolution equation for LGA (Eq. 2.4), we replace the collision operator $C_i(n)$ with $C_i(f)$:

$$\Delta_i f = C_i(f). \qquad \ldots(2.12)$$

This is the first Lattice Boltzmann equation. $\Delta_i f$ denotes the change in $f_i$ affected by the collision operator, $C_i(f)$. Here $\Delta_i f$ is equivalent to the $\Delta_i n$ in Eq. 2.4 and the $C_i(f)$ is equivalent to $C_i(n)$ in Eq. 2.5. We use exactly these same LGA equations for the collision operators, except that a link has a fill value of $f_i$ instead of 1 and an emptiness of $1 - f_i$ instead of 0.

Using fractional number of particles greatly reduced the statistical fluctuations [29]. McNamara and Zanetti [28] showed that even for very small lattices, the LBM simulates the Navier-Stokes equation well. Initially the form of the LBM was very similar to the form of the LGA method, but over time the LBM evolved into quite a different method. The method became known as the "Lattice Boltzmann Method" because of the similarity of the collision equation to the Boltzmann equation, and $f_i$ became known as the "particle density distribution function". Furthermore, it was quickly realized that the LBM could be greatly simplified. This simplification not only enhanced computational efficiency but it also solved the Galilean invariance problem rather than just minimizing it.

B. The Boltzmann equation

The Boltzmann equation, established by Lugwig Boltzmann in 1872, is the basis of kinetic statistical mechanics, the area of physics which studies how non-equilibrium processes relax to thermodynamic equilibrium. Statistical mechanics is based on a particle momentum distribution, $f(\bar{x}, p, t)$, where $\bar{x}$ is the position of a particle at time t, and p is its momentum. This momentum distribution function gives the probability of finding a particle at position $\bar{x}$ at time t with a momentum p. Lugwig Boltzmann was able to derive an evolution equation for $f(\bar{x}, p, t)$ based on particle interactions. This evolution equation is the Boltzmann equation:

$$\left[\partial_t + \frac{p}{m}\cdot\partial_x + F\cdot\partial_p\right] f(\bar{x}, p, t) = C^{12}. \qquad \ldots(2.13)$$

The left hand side of Eq. 2.13 describes how $f(\bar{x}, p, t)$ changes in time, space, and upon application of a force. $C^{12}$ describes the collision of two particles, where the

superscript 1 and 2 label the particles involved. The $C^{12}$ includes the two particle distribution function, $f^{12}$, which is the probability of finding particle 1 at $x_1$ with a momentum of $p_1$ and particle 2 at $x_2$ with a momentum $p_2$. However, the position and momentum of a particle depends on its previous collision, requiring the knowledge of a three particle distribution function, $f^{123}$. The $f^{123}$ distribution, in turn, depends upon the calculation of the $f^{1234}$ distribution and so on. This type of hierarchy is known as the BBGKY hierarchy, after the researchers who first described it; Bogoliubov, Born, Green, Kirkwood and Yvon [30]. From this it is clear that the $C^{12}$ term is unobtainable. In order to solve the equation, Boltzmann assumed the collision term only involves two particles. This can be justified if the particles are points with very small cross section and their motion is chaotic such that the motion of the particles are completely independent of each other prior to their collision. Under these conditions, particles spend most of time in free trajectories and only interact during an infinitely short period of time. The collision term now describes only the gains and losses in the numbers of particles traveling in different directions as a result of a collision.

Although the Boltzmann equation was then technically solvable, the solution is still difficult due to the complexity of the collision term. Therefore, for problems in statistical kinetics, the collision operator is often replaced by a class of simplified collision expressions which retain the conservation of mass and momentum of two body interactions. One operator, known as the BGK (after Bhatnager, Gross and Krook [31]) collision operator, is:

$$C^{BGK}(f) = -\frac{f - f^{eq}}{\tau}. \qquad \ldots(2.14)$$

$C^{BGK}$ is the BGK collision operator; $f^{eq}$ is the equilibrium distribution and $\tau$ is the time to relax to equilibrium.

With this brief background on the Boltzmann equation, we now discuss how the Lattice Boltzmann equation (Eq. 2.12), evolved to its present form through the simplification of the Lattice Boltzmann Collision equation.

C. The scattering matrix

The first simplification of the Lattice Boltzmann collision operator was obtained by Higuera et. al [16] who expanded the particle distribution function in a Taylor series expansion about its local equilibrium value. The resulting Lattice Boltzmann collision equation was:

$$\Delta_j f = C_{ij}(f_i - f_i^{eq}). \qquad \ldots(2.15)$$

$C_{ij}$ is the derivative of the collision operator with respect to the particle distribution function and may be thought of as another collision operator. $C_{ij}$ is known as the linearized collision matrix or the scattering matrix and can be analytically solved. Once it is calculated it can be used as a look-up table. This means that calculations can be made with much greater efficiency, and 3D lattices can be solved with a personal computer.

D. Enhanced collisions

The next stage in the evolution of the LBM really set it apart from the LGA. Higuera et al. [16] realized that unlike the LGA method, the collision matrix did not have to contain information pertaining to the individual collisions, allowing it to be vastly simplified. Consider an element, $C_{ij}$, of the collision matrix. $C_{ij}$ gives the rate

at which a distribution is redistributed from the $i^{th}$ link to the $j^{th}$ link. The only information necessary for this redistribution is the angle between the $i^{th}$ link and the $j^{th}$ link. Furthermore, since the collision matrix is symmetric and cyclic, it can be reformulated in terms of its eigenvectors and eigenvalues; where the eigenvectors are the basis set of vectors defining the grid geometry and the eigenvalues relate to some physical property of the system. For a 2D hexagonal grid there are six eigenvectors and six eigenvalues. The elements of the collision matrix can be found from relating them to the eigenvalues of the system [6]. Conservation of mass and momentum require that D+1 eigenvalues are zero [16], where D is the spatial dimension. Of these, D eigenvalues relate to the momentum conservation, and the last eigenvalue describes mass conservation. For example, in the case of the FHP lattice, there are 2 eigenvalues relating to the x and the y momentum and one relating to mass conservation. Of the remaining three non-zero eigenvalues, two are related to the decay of the distribution functions to equilibrium [11] and a third eigenvalue is related to the kinematic viscosity [14]:

$$\mu = \frac{c^2}{D}\left(\tau - \frac{1}{2}\right). \qquad \ldots(2.16)$$

Here $\mu$ is the viscosity of the fluid, c is the speed of particles along each of the links, D is the dimension of the system (in the FHP case D = 2), and $\tau = 1/\lambda$ and is known as the relaxation coefficient, where $\lambda$ is the eigenvalue.

The power of the LBM is that as long as the collision matrix continues to observe the conservation laws, the non-zero eigenvalues can be changed at the researcher's whim. In essence, we have removed all dependence on the choice of collision rules. There is no reason to be tied down to any particular equilibrium distribution either. By freely choosing the viscosity and the equilibrium distribution,

we effectively created an infinite range of collisions [32]. In other words, we have created an infinite number of ways momentum can be redistributed about each node. The whole issue of Galilean invariance automatically dissolves [32-35] since we have effectively created a continuum of velocities.

Since the equilibrium distribution was no longer tied to the lattice geometry, any lattice geometry could be chosen. Thus 3D simulations were greatly simplified by choosing the simpler cubic 3D lattice, instead of the cumbersome 4D Face-Centered Hyper Cubic (FCHC) lattice [14]. With the range of usable lattice-systems greatly increased, a nomenclature of describing the lattice by their dimensionality and the number of velocities was established [14]. For example: 3DQ19 is the 3D cubic lattice with 19 velocities. We use this convention from this point onwards. The letter 'Q' refers to the author of the classification terminology, Y. H. Qian [14].

Although the transport coefficients were no longer tied to the underlying microscopic dynamics, the range possible transport coefficients were still limited by stability constraints. For example in the case of the viscosity, stability constraints required that $\tau > 1/2$. Viscosity can not be zero or negative in Eq. 2.16.

E. The Lattice Boltzmann - Bhatnagar-Gross-Krook model

At this point, the LBM has two "free" parameters which allow researchers to adapt the method to fit the problem they are solving. These are the equilibrium particle distribution and the relaxation coefficient, $\tau$, which is related to the viscosity of the system though Eq. 2.10. The particle density equilibrium distribution, $f_i^{eq}$, is normally chosen to observe mass and momentum conservation [14, 34], so we are left with a system, which, except for boundary and initial conditions, has one free parameter, $\tau$. For a single fluid with no external forces, $f_i^{eq}$ is equivalent to an ideal gas equilibrium distribution, producing the ideal gas equation of state [14, 34]. The

ideal gas equation of state results in an equal number of particles on each node and, as discussed later, the same distribution of particles on each of the links around a node where the particle distribution depends on the number of links with different speeds around a node. Figure 2.5 provides a simple example of a pre- and post-collision node which is relaxing to the ideal gas equilibrium state on the 2D FHP grid. The equilibrium state has an equal number of particles on each link in the equilibrium state since all links are assigned the same speed.

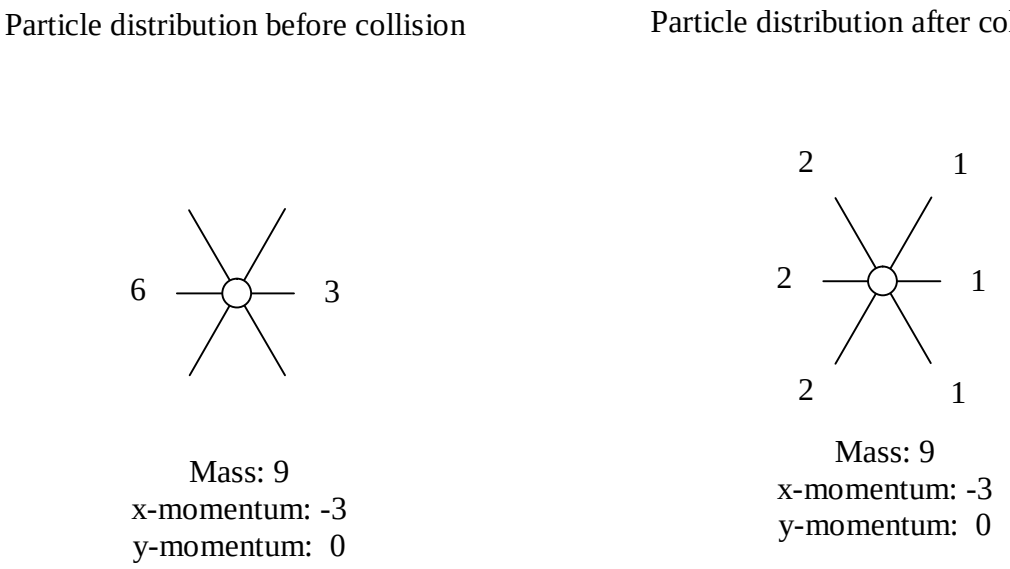


Figure 2.5: Example of the redistribution of particles as a result of the collision step.

Figure 2.5 shows how, at equilibrium, particles are redistributed such that mass and momentum are conserved and the particles settle to a distribution predicted by the ideal gas equation of state. In this case, any deviations from the equilibrium state is caused by the necessary conservation of momentum.

A common equilibrium distribution [16] which we use in our model, is:

$$f_i^{eq} = \rho a_{c_i}\left[1+\frac{D}{c^2}e_{i\alpha}u_\alpha + \frac{D^2}{2c^4}Q_{i\alpha\beta}u_\alpha u_\beta\right] + F_i \qquad \ldots(2.17)$$

$$Q_{i\alpha\beta} = e_{i\alpha}e_{i\beta} - \frac{c^2}{D}\delta_{\alpha\beta} \qquad \ldots(2.18)$$

Where $a_{c_i}$ is the coefficient of a link with velocity c, as discussed below, D is the dimension, $u_\alpha$ is the velocity of the system in the $\alpha^{th}$ direction, $e_{i\alpha}$ is the $\alpha^{th}$ component of velocity of a particle distribution on the $i^{th}$ link, and $F_i$ is the body force acting on all particles on the $i^{th}$ links. Eq. 2.17 gives the equilibrium distribution on a given node at link *i*.

At this stage, it became obvious to a number of researchers [14, 36, 37] that the relaxation parameter, $\tau$, could be incorporated into the collision operator (Eq. 2.15). The relaxation parameter then cleanly represents the rate at which the system approaches equilibrium, and the collision operator becomes a diagonal matrix:

$$C_{ij} \to -\frac{1}{\tau}\delta_{ij}, \qquad \ldots(2.19)$$

where, $\delta_{ij}$ is the Kroneckor delta and $\tau$ is the relaxation time to local equilibrium.

The final LBM-BGK equation is then:

$$\Delta_i f = -\frac{1}{\tau}(f_i - f_i^{eq}). \qquad \ldots(2.20)$$

This equation illustrates the beauty of the LBM. Although a lot of theoretical analysis was required, it was ultimately shown that Navier Stokes flow in a discrete system can

be simulated with an extremely simple collision equation. This led to an easy-to-implement, efficient methodology. Furthermore due to the locality of the collision step in LBM, the method lends itself to parallel processing, which can greatly reduce the computational expense and simulation time.

F. The numerical grid

Any actual simulation must be carried out on a particular grid. A commonly used grid, and the grid we shall use here, is a 3D cubic grid with 19 links called the 3DQ19 model. The base unit of this grid is shown in Figure 2.6. Table 2.9 gives the locations of the links with respect to the central node. Table 2.9 also gives the link lengths, which is equivalent to the speed of the particles residing on these links. Each link connects the central node to its 18 neighbor nodes. Each of these neighbor nodes, in its own turn, can be considered a center node.

Within this model there are three speeds: c = 0 (one distribution at i = 0), c = 1 (six distributions at i = 1,2,3,4,5,6), and c = $\sqrt{2}$ (12 distributions at i = 7,8,9,10,11,12,13,14,15,16,17,18). The resulting coefficients ( $a_{c_i}$ in Eq. 2.17) for the three speeds, $c_i$, are:

$$a_0 = \frac{1}{3}, \qquad a_1 = \frac{1}{18}, \qquad a_{\sqrt{2}} = \frac{1}{36} \qquad \ldots(2.21)$$

For the case of a single phase without external forces, these coefficients define the equilibrium distribution of particles around a node to be such that a third of the particles are located on the rest link ( $c_i = 0$ ), a third are located among the links with $c_i = 1$ and a third are located among the links with $c_i = \sqrt{2}$ .

Application of Eq. 2.20 to the lattice is simple. First one defines the average density of particles in the system. One then sets the density distributions at each node to be randomly distributed about the average density. The relaxation constant, $\tau$, is defined; normally we use $\tau = 1$. We compute $f_i^{eq}$ from Eq.s 2.17 and 2.18. We then calculate $\Delta_i f$ iteratively until $\Delta_i f \approx 0$; indicating that $f_i \approx f_i^{eq}$. The boundaries are normally defined as in the LGA system.

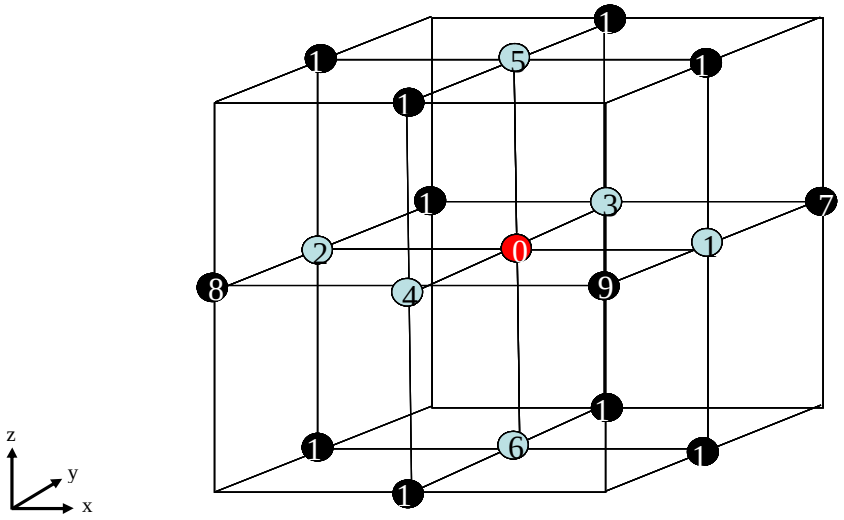


Figure 2.6: A single 3DQ19 cube of the LBM lattice is shown, with the locations of the 18 neighbor nodes, color coded by distance from the central node. The central node is red and is the location of the zero-velocity density distribution. The grey nodes are at the center of each of the faces of the cube, and the black nodes are at the middle of each of the edges of the cube.

G. Body forces

Body forces are added through the directionally-dependant force term in the equilibrium distribution, Eq. 2.17. This force term partially redistributes the particle motion at a node in the direction of the force term.

H. Boundary conditions

We either use constant pressure (no flow) or periodic (free flow) boundary conditions. Let us consider a grid of size $\{L_x, L_y, L_z\}$. As in the LGA method, the periodic boundary condition maps any particle leaving the grid in, for example, the positive x-direction at $x = L_x$, back into the other end of the grid at $x = 0$. The no-flow boundary condition bounces the particles off the boundary such that their momentum parallel to the boundary is conserved and the momentum perpendicular to the boundary is reversed. This process is illustrated in Figure 2.7. The constant pressure boundary condition is applied by removing the periodic nature of the boundary and maintaining a constant density at the boundary. Since the density is directly related to the pressure, this imposes a constant pressure at the boundary. A full discussion of this boundary condition and other implementations in our code, is given in Section 2.4


Figure 2.7: Illustration of the no-flow boundary condition

Table 2.9: Directions of the 19 links of the 3DQ19 model.

| | Location with respect to the central node | Distance from central node | Neighbor # | Location with respect to the central node | Distance from central node |
|---|---|---|---|---|---|
| $e_0$ | {0,0,0} | 0 | $e_{10}$ | {-1,1,0} | $\sqrt{2}$ |
| $e_1$ | {1,0,0} | 1 | $e_{11}$ | {1,0,1} | $\sqrt{2}$ |
| $e_2$ | {-1,0,0} | 1 | $e_{12}$ | {-1,0,-1} | $\sqrt{2}$ |
| $e_3$ | {0,1,0} | 1 | $e_{13}$ | {1,0,-1} | $\sqrt{2}$ |
| $e_4$ | {0,-1,0} | 1 | $e_{14}$ | {-1,0,1} | $\sqrt{2}$ |
| $e_5$ | {0,0,1} | 1 | $e_{15}$ | {0,1,1} | $\sqrt{2}$ |
| $e_6$ | {0,0,-1} | 1 | $e_{16}$ | {0,-1,-1} | $\sqrt{2}$ |
| $e_7$ | {1,1,0} | $\sqrt{2}$ | $e_{17}$ | {0,1,-1} | $\sqrt{2}$ |
| $e_8$ | {-1,-1,0} | $\sqrt{2}$ | $e_{18}$ | {0,-1,1} | $\sqrt{2}$ |
| $e_9$ | {1,-1,0} | $\sqrt{2}$ | | | |

I. Immiscible Fluids

To date, there are three main methods of modeling immiscible fluids. These methods are outlined below.

1. The color model of Gunstensen et. al.

Gunstensen et. al. [35] were the first to model immiscible fluids with LBM and did so in 1991. Their method was an adaptation of Rothman and Kellers' [12] earlier work with LGA. Two distinct density distributions are introduced into the lattice, each labeled by a color, either "red" or "blue". Each undergoes a collision, ignoring the other color. An additional step is then taken during which each color "feels" the surrounding color density distributions. A force is derived which pushes each distribution towards concentrations of its own color type, and away from concentrations of the other color distribution.

Gunstensen et. al.'s method produced a very thin interface (~1 node) between the two differently colored particles. It was observed [36] that such a thin interface is extremely sensitive to its orientation with respect to the lattice. This lead to nonphysical features such as faceted bubbles of one color, unphysical vortices near the interfaces, spatially ansiotropic interfacial tension, etc. An obvious way of alleviating these non-physical aspects of the model is by thickening the interface. Although a method was suggested [36], it produced more undesirable effects than it solved and violated Galilean invariance. Another criticism of the Gunstensen et. al.'s color method was that its calculations were computationally expensive.

2. The Shan and Chen model

Shan and Chen introduce a so-called "interaction potential" defined in Eq. 2.22, which defines the interaction between two phases.

$$V(x,x') = G_{\sigma\sigma'}(x,x')\psi^{\sigma}(x)\psi^{\sigma'}(x') \qquad \ldots(2.22)$$

Here, $V(x,x')$ is the interaction potential between $\psi^{\sigma}(x) = F(f^{\sigma}(x))$ and $\psi^{\sigma'}(x) = F(f^{\sigma'}(x'))$. $G_{\sigma\sigma'}(x,x')$ is a Green's function defining the distance dependant strength of the interaction between a phase at a central node and a phase at a neighboring node. In our code, we only use nearest neighbor interactions and following Shan and Chen, allow $\psi^{\sigma}(x) = \rho_{\sigma}(x)$ and $\psi^{\sigma'}(x) = \rho_{\sigma'}(x)$. Where $\rho_{\sigma}$ is the nodal density of the σ phase a the central node and Where $\rho_{\sigma'}$ is the nodal density of the σ phase at the central node. In this way a rate of momentum change can be defined as

$$\frac{dj_{\sigma}}{dt} = -\rho_{\sigma}(x)\sum_{\sigma'=1}^{S} G_{\sigma\sigma'}\sum_{i=0}^{b}\rho_{\sigma'}(x)(x'+e_i)e_i \qquad \ldots(2.23)$$

Where S is the number of phases in a system and b is the number of links. Eq. 2.23 can be simplified [37] so that:

$$\frac{dj_{\sigma}}{dt} = \rho_{\sigma}(g_{\sigma\sigma}\nabla\rho_{\sigma} + g_{\sigma\sigma'}\nabla\rho_{\sigma'}) \qquad \ldots(2.24)$$

Where $\nabla\rho_{\sigma}$ is the gradient of the σ phase surrounding the central node and $g_{\sigma\sigma}$ is the strength of the interaction between the σ phase in the surrounding nodes and the σ phase in the central node. Similarly, $\nabla\rho_{\sigma'}$ is the gradient of the σ′ phase surrounding the central node and $g_{\sigma\sigma'}$ is the strength of the interaction between the σ′ phase in the surrounding nodes and the σ phase in the central node. The negative sign is swallowed by the sign of g. If g < 0, the force is repulsive and if g>0 it is attractive.

The Shan-Chen method has been shown to replicate interfacial tension effects [37]. Additionally, it allows first order phase transitions to be modeled. Because of the addition of the force to the total momentum at each site, the method violates the conservation of local momentum. However, it has been shown [37] that the global momentum is still conserved.

3. The thermodynamically consistent model

The pressure of the LBM fluid is the same as for the LGA, namely that of an ideal gas,

$$P = \rho c_s^2 , \qquad \ldots(2.25)$$

where P is the pressure, $\rho$ is the density, $c_s^2$ is the square of the speed of sound for a LB fluid, and $c_s = c_{avg} / \sqrt{D}$. $c_{avg}$ is the averaged speed for the node, weighted by the coefficients $a_{c_i}$, such that $c_{avg} = 1$. Swift et.al. [38,39] pointed out that the equation of state for immiscible fluids is non-ideal and therefore models which superimpose a force on top of an ideal equation of state to produce immiscibility are thermodynamically inconsistent. They argue that the interfacial tension effects produced by earlier methods were phenomenicalogical and not based on valid physical principles. Swift et.al. proposed that, by adding a suitable term into the equilibrium distribution, one could change the equation of state into the van der Waals (non-ideal) equation of state. In this way interfacial tension effects would result from the kinematics of the fluids.

2.4: Implementation, Instabilities, Boundary Conditions, Initial Conditions and Wettability.

For our experiments, we implemented the Shan Chen method of immiscibility. During our simulations we found it necessary to expand the code as originally implemented. The expansion of the code primarily dealt with instability and a limited range of implementation boundary conditions, initial conditions and wettability.

A. Instabilities in the Shan-Chen method

Instabilities associated with the Shan-Chen method are well known [40]. The instabilities associated with the Shan Chen method appear to start off when negative masses exceed a threshold. We observed that small nodal negative masses $\rho > -0.5$ appear even in stable simulations. Therefore it appears that a critical negative nodal mass is required for the system to become unstable.

An understanding of the origin of these instabilities may be found from a detailed look into the Shan Chen [37] equations that impose phase segregation. The Shan-Chen [37] segregation force, detailed above in Eq 2.22 through Eq. 2.24, is applied as a change in momentum over a time step:

$$j'_{w\_SEGREGATION} = \rho_w u'_w = \rho_w u + \rho_w (g_{ww} \nabla \rho_w + g_{wn} \nabla \rho_n) \quad \ldots(2.26)$$

$$j'_{n\_SEGREGATION} = \rho_n u'_n = \rho_n u + \rho_n (g_{nn} \nabla \rho_n + g_{nw} \nabla \rho_w) \quad \ldots(2.27)$$

Here, $\rho_w u'_w$ is the wetting phase momentum after phase segregation forces are applied to the wetting fluid, $\rho_n u'_n$ is the same for the non-wetting fluid, $\rho_w u_w$ and $\rho_n u_n$ are the wetting and non-wetting phases prior to phase segregation. $u$ is the average velocity of both fluids, $g_{ww}$ and $g_{nn}$ are the degree to which each fluid is

cohesive and $g_{wn}$ and $g_{nw}$ interfacial tension coefficients of the wetting and the non-wetting phases respectively. $\rho_w$ and $\rho_n$ are the densities of the wetting and non-wetting phases respectively. Like Shan and Chen [37], we set $g_{wn} = g_{nw} = g$. We followed Shan and Chen's lead of setting $g_{ww} = g_{nn} = 0$ for our experiments with dynamic contact angles (Chapter 4), but found a stronger wettability behavior if we set $g_{ww}$ =0.5 in our capillary sealing experiments (Chapter 3).

Following Shan and Chen's suggestions, the equations become:

$$j'_{w\_SEGREGATION} = \rho_w u + \rho_w g \nabla \rho_n \quad \ldots(2.28)$$

$$j'_{n\_SEGREGATION} = \rho_n u + \rho_n g \nabla \rho_w \quad \ldots(2.29)$$

Following Ladd and Verberg [41], these velocity and density gradients are calculated in the x, y and z directions and then incorporated into the collision step as an adjusted momentum.

For each node, the mass and momentum for each fluid, σ, is calculated: $\rho_\sigma$, $j_{\sigma x}, j_{\sigma y}$ and $j_{\sigma z}$. The post-collision densities are the equilibrium densities with an adjustment to take into account immiscibility and any body forces. Following Ladd and Verberg [41] for the equilibrium distributions, we place $\rho_\sigma / 3$ in the rest particle distribution, $\rho_\sigma / 3$ is equally distributed between the six velocity = 1 distributions, which head out to the center of each of the six cubic faces. The last $\rho_\sigma / 3$ is equally distributed between the remaining twelve distributions, which all have a velocity = $\sqrt{2}$ and head out to the center of each of the cube's twelve edges. Figure 2.6 illustrate the velocity vectors of each of the 19 particle density distributions, and Table 2.8 gives the x, y and z velocity components, $e_i$, for each of the 19 particle density distributions. The resulting post-collision distributions are as follows:

For i = 0:

$$\rho_{\sigma 0\_coll} = \rho_{\sigma} / 3 \qquad \ldots(2.30)$$

For $1 \leq i \leq 6$:

$$\rho_{\sigma i\_coll} = (\rho_{\sigma} + e_{ix} j'_{\sigma x} + e_{iy} j'_{\sigma y} + e_{iz} j'_{\sigma z}) / 18 \qquad \ldots(2.31)$$

For $7 \leq i \leq 18$:

$$\rho_{\sigma i\_coll} = (\rho_{\sigma} + e_{ix} j'_{\sigma x} + e_{iy} j'_{\sigma y} + e_{iz} j'_{\sigma z}) / 36 \qquad \ldots(2.32)$$

Where $\rho_{\sigma k}$ is the density of the $\sigma^{th}$ phase for the $i^{th}$ particle density distribution and $j_{\sigma\alpha}$ is the α-momentum for the $\sigma^{th}$ phase, where $\alpha = \{x,y,z\}$, and where

$$j'_{\sigma\alpha} = \frac{\rho_{\sigma}}{\rho} \sum_{\sigma} j_{\sigma\alpha} + \rho_{\sigma} j'_{\sigma\alpha\_SEGREGATION} + \frac{\rho_{\sigma}}{\rho} F_{\alpha} \qquad \ldots(2.33)$$

Where $j'_{\sigma\alpha\_SEGREGATION}$ is the additional momentum due to immiscibility on fluid σ, aligned with the α-axis. We found that the first term on the right to be necessary in order for one phase to react to the flow of the other phase. Without this term a bubble of non-wetting fluid will not move with the flow of the non-wetting phase as it logically must. In regions where both fluids are significantly present, as in interfacial regions, this term allows the translation of momentum in one fluid to be proportionally translated into the other fluid's momentum. This translation of the momentum into the other fluid is then passed into the body of the other fluid with each time step. See Figure 2.8 for an illustration of our code with and without this first term.

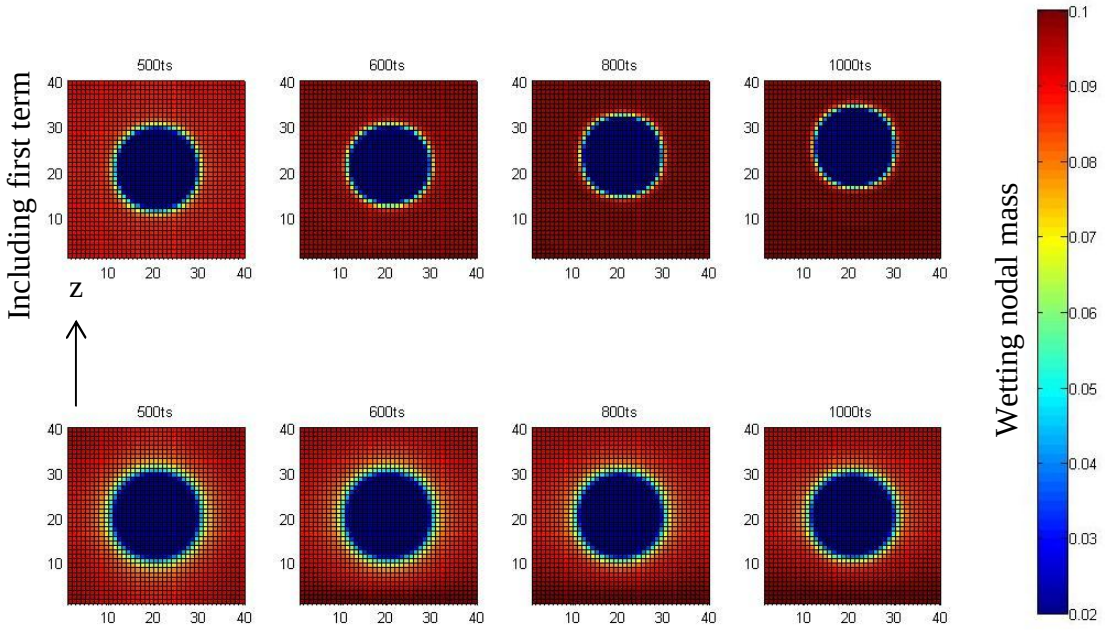


Figure 2.8: Illustrating the effect of the $\rho_\sigma / \rho \sum_\sigma j_{\sigma\alpha}$ term on the right of Eq. 2.33. A simulation is initialized with a non-wetting bubble in a box of side 40 lattice units. All boundaries are periodic until 500 time steps, to allow the bubble to come into equilibrium. At 500 time steps, the inlet and outlet for the wetting fluid become fixed pressure boundaries, with a pressure gradient of 0.017 pressure units/lattice units in the z direction. All non-wetting fluid boundaries remain as periodic. With the inclusion of the $\rho_\sigma / \rho \sum_\sigma j_{\sigma\alpha}$ term, the non-wetting bubble is pushed along, with the same velocity as the wetting fluid, as shown in the top row. Without the $\rho_\sigma / \rho \sum_\sigma j_{\sigma\alpha}$ in the adjusted momentum term, the non-wetting bubble is unaffected by the pressure gradient in the wetting fluid and the flow it induces in the wetting fluid, as illustrated in the bottom row.

The last term accounts for body forces. Since the momentum adjustment results in density being added or removed from a particle density distribution, the $\rho_\sigma / \rho$ term was needed to prevent a fluid density being added to node where there was insignificant amounts of phase σ in the pre-collision step. Note that the relaxation parameter, τ=1, in our version of the code.

Negative densities occur if the modulus of the adjusted momentum components for a given particle density distribution function, is greater than the density of the node, and is negative. For example, looking at i = 1:

If $\left| j'_{\sigma x} \right| > \rho_{\sigma z}$ and $j'_{\sigma x} < 0$, then

$$\rho_{\sigma 1\_coll} = (\rho_\sigma + j'_{\sigma x}) / 18 < 0 \qquad \ldots(2.34)$$

$$\rho_{\sigma 2\_coll} = (\rho_\sigma - j'_{\sigma x}) / 18 > 0 \qquad \ldots(2.35)$$

This would result is having a negative density on the i=1 particle density distribution function and a positive density on the i=2 particle density distribution function. During the next step when the gradient function would be calculated, this negative density would be propagated in the positive x direction, resulting in an even greater density gradient in the negative x direction. This greater density gradient translates into an even more negative adjusted x-momentum. This in turn creates a more negative $e_1$ particle density distribution function, and so the feedback mechanism is created. Swift et. al. [38] previously noted that instabilities are associated with large density gradients.

In our code we formulated four ways of tackling this instability:

1. Generalized scheme to remove negative densities.

*Removal of negative densities post-collision.*

A scheme was created in which the mass and momentum of each node post-collision was conserved, but each of the particle density distributions were adjusted so that all distributions were greater than zero. For example, if a negative particle distribution was located on i=1 {1,0,0} post collision, then the modulus of that density could be added onto i=2 {-1,0,0}, allowing a zero density on i=1. This would conserve the total mass and momentum of the node. However it was found that in the case of multiple particle density distributions having negative values, some negative particle densities distributions would persist, and the code was not unconditionally stable.

*Removal of negative densities during the collision step.*

Assuming that the original particle density distribution were all positive, by ensuring that the modulus of the total adjusted momentum was never greater than the mass of the node, then no particle density distribution would become negative. This was achieved by reducing the adjusted momentum components in question until the post collision particle density distribution was positive. However, while this methodology resulted in an unconditionally stable code, the non-systematic way in which the adjusted momentum was reduced in the interfacial regions caused violation of physical laws. For example it was observed that Laplace's law was not obeyed, and non-spherical bubbles were formed. Therefore when negative density removal schemes were used, we used the post-collision negative densities removal scheme.

2. Reducing g

In absence of a body force, the region in which the strongest adjusted momentum occurred was at the interface between two fluids, due to the relatively large density gradients. There seems to be a balance for most situations in which g is strong enough that phase separation occurs, but weak enough so that pathological instabilities do not occur. For the case in which the generalized negative density removal was not switched on, it was found that g could be any value up to g = -0.19 before pathological instabilities occurred. For the case in which a post-collision negative density removal scheme was switched on, the g could be increased to only g=-0.8.

3. Reducing the virtual wetting fluid mass in the corners.

The wettability of a solid was created by providing the solid nodes with a virtual wetting mass, which was then incorporated into the density gradients of the adjacent fluid nodes. It was found that in simulations where the solid had some (coarse) curvature, instability would invariably arise in a boundary fluid node surrounded by two solid nodes, termed a “corner node”. See Figure 2.9 below.

By reducing the influence of the double virtual wetting mass in the density gradients in these corner nodes, it was found that the instability was reduced. When calculating the density gradient at corner nodes, we reduced the virtual mass at the adjacent solid nodes by a factor of $\sqrt{7}$. This approach resulted in a stable code, but still seemed to allow a larger wetting mass to accumulate in these corner nodes. As we tested the virtual mass factor reduction for corner nodes, it was noticed that the density gradients about these corner nodes remained the same. Therefore it appeared that this apparent mass accumulation did not seem to affect to the overall flow pattern.

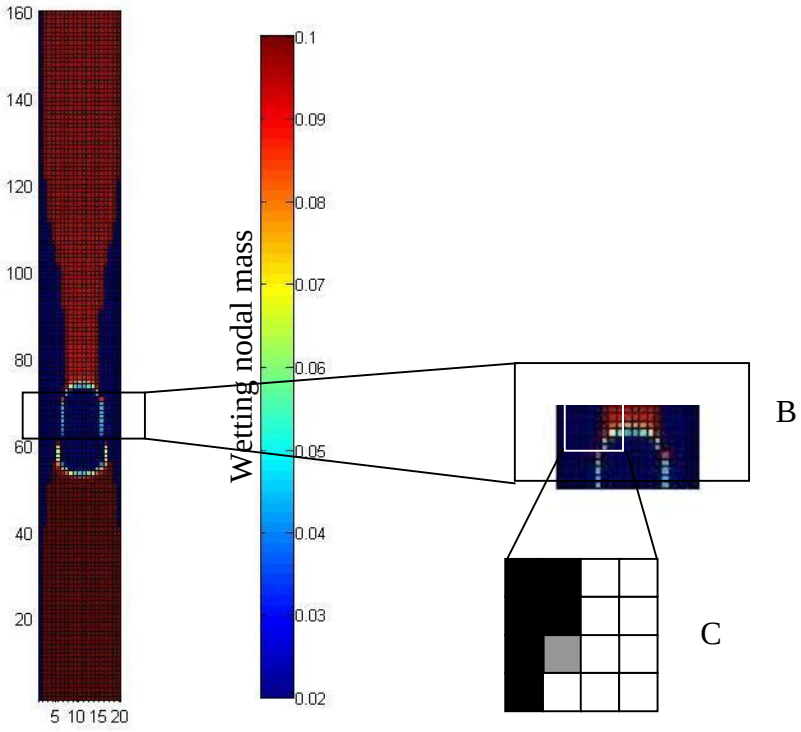


Figure 2.9: Illustration of a simulation involving a coarsely curved geometry. The concept of a corner node is illustrated in (C), where the solid nodes are black, the corner nodes are grey and the non-corner fluid nodes are white. Note the wetting mass accumulation in the corner nodes in (B), indicated by the relative redness of the fluid nodes with respect to its immediate fluid neighbors.

B. Boundary conditions

1. The implementation of the default boundary condition: periodic boundary conditions

Periodic boundary conditions, which appear to be the most common in the literature [32, 34], allow free flow of particle density distributions from the opposite boundaries. This is illustrated in Fig 2.10, where we have drawn the FHP 2D lattice for simplicity. The particle density distributions located on the inner links of the boundary layers came from the opposite boundary. Thus particles on links 1 and 2 that are leaving the bottom boundary (left bottom of Figure 2.10) in the translation step, move to the inner links of the top boundary (right top of Figure 2.10). Similarly the particle density distributions leaving the top wind up on the inner links of the bottom boundary nodes. Thus the numbered lower boundary particles wind up on the inner link of the top boundary, and the lettered top boundary particles wind up on the inner links of the bottom boundary, as shown in Figure 2.10. This boundary particle density distribution translation is a periodic boundary condition, where there is mass and momentum continuity between two opposite boundaries.

As a result of the translation step/periodic boundary condition implementation, the particle distribution arriving from the opposite boundary always land on the outer most layer of nodes. Non-periodic boundary conditions are simulated by over-writing the particle density distributions on these outer layers of nodes, after translation. When the density gradients are calculated for non-periodic boundary conditions, the outer most nodes use their own masses instead of those on the opposite boundary. This removes any continuity between the boundaries.

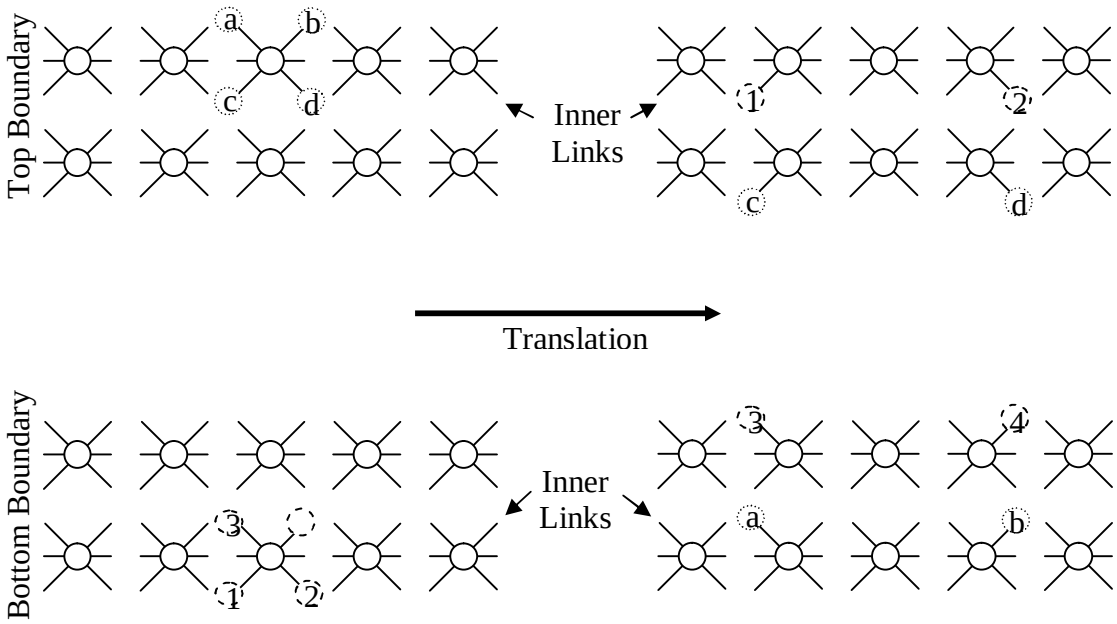


Figure 2.10: Illustration of particle density distributions translation at the top and bottom boundaries.

Periodic boundary conditions can not exist in conjunction with a pressure gradient, since a pressure gradient would require the maintenance of different particle densities at either end of the tube, yet the periodic boundary conditions would exert density continuity between the two ends. Therefore simulating flow through a system with periodic boundary conditions can only be imposed by applying a body force, or with some other boundary condition. A body force would not be appropriate for our capillary sealing simulations since gravity is negligible at these scales in natural settings, and such a body force may obscure the pore blockage. Therefore we investigated using other types of boundary conditions.

2. Mixed inlet, no-gradient outlet.

To create a physically real simulation, we implemented an inlet boundary condition in which a mixture of wetting and non-wetting fluid was continuously placed on the first layer of nodes, mimicking the continuous introduction of gas and water into the tube. The total particle density of the introduced mixture was greater than that in the rest of the system, causing this mixture to exert a pressure on the downstream fluid, stimulating flow. Figure 2.11 illustrates this process. Initially there is not enough non-wetting fluid to create a bubble. However once enough non-wetting fluid is introduced, a bubble is formed, we see the bubble being stretched downstream, eventually pinching off.

A zero pressure gradient was imposed at the exit end by copying all the particle distributions functions from the second layer upstream into the last layer. The density gradients for the last layer of nodes were also taken from the second-to-last layer of nodes upstream. In this way we simulated an outlet without a density gradient.

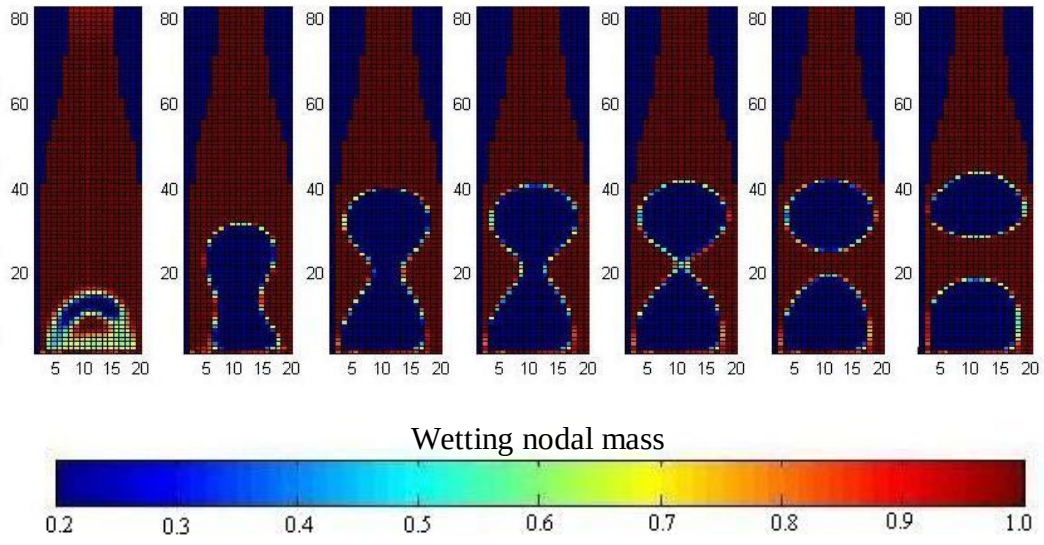


Figure 2.11: Illustration of the mixing inlet boundary condition.

3. Increasing pressure inlet.

In the same manner as with the mixed inlet boundary conditions, we implemented a boundary condition in which just the wetting fluid was continuously added into the system. Again, due to the relatively larger wetting mass of the first layer of nodes, this created a pressure gradient, stimulating flow through the system.

4. Fixed pressure inlet, outlet.

In order to investigate the durability of a capillary sealed pore, as well as its permeability to wetting fluid film flow, a stable pressure gradient needed to be established. The simplest way to create a stable pressure gradient was to fix the wetting densities at the inlet and outlet. In simulations where the non-wetting fluid density was very low at the inlet and outlet, such as in the capillary sealing simulations, we found that by fixing the non-wetting densities at the boundaries, we artificially introduced or removed non-wetting fluid from the system. In such cases, the most realistic behavior was found by imposing a periodic boundary condition on the non-wetting fluid.

C. Initial conditions

The code was designed by us to have a variety of possible initial conditions, enabling the user to choose the most suitable initial conditions for their simulation.

1. Mixed initial conditions

A mixed initial condition was one in which the fluid phases were mixed, in user-defined proportions within a user-defined region. This would allow the fluid to separate into an equilibrium configuration within a desired region. For example, in the capillary sealing simulations, we initialized the simulation with a mixture of both

fluids within a small region, just before the pore. We then allowed for a non-wetting bubble to segregate, which took less than 500 time steps. During this time, periodic boundary conditions were turned on in order to minimized any external forces on the bubble forming process. Once a bubble was formed, we then switched on the fixed pressure boundary conditions. The choice of allowing a bubble to form near the pore reduced simulation time in comparison with starting off with boundary/initial condition in which the bubble formed nearer the inlet.

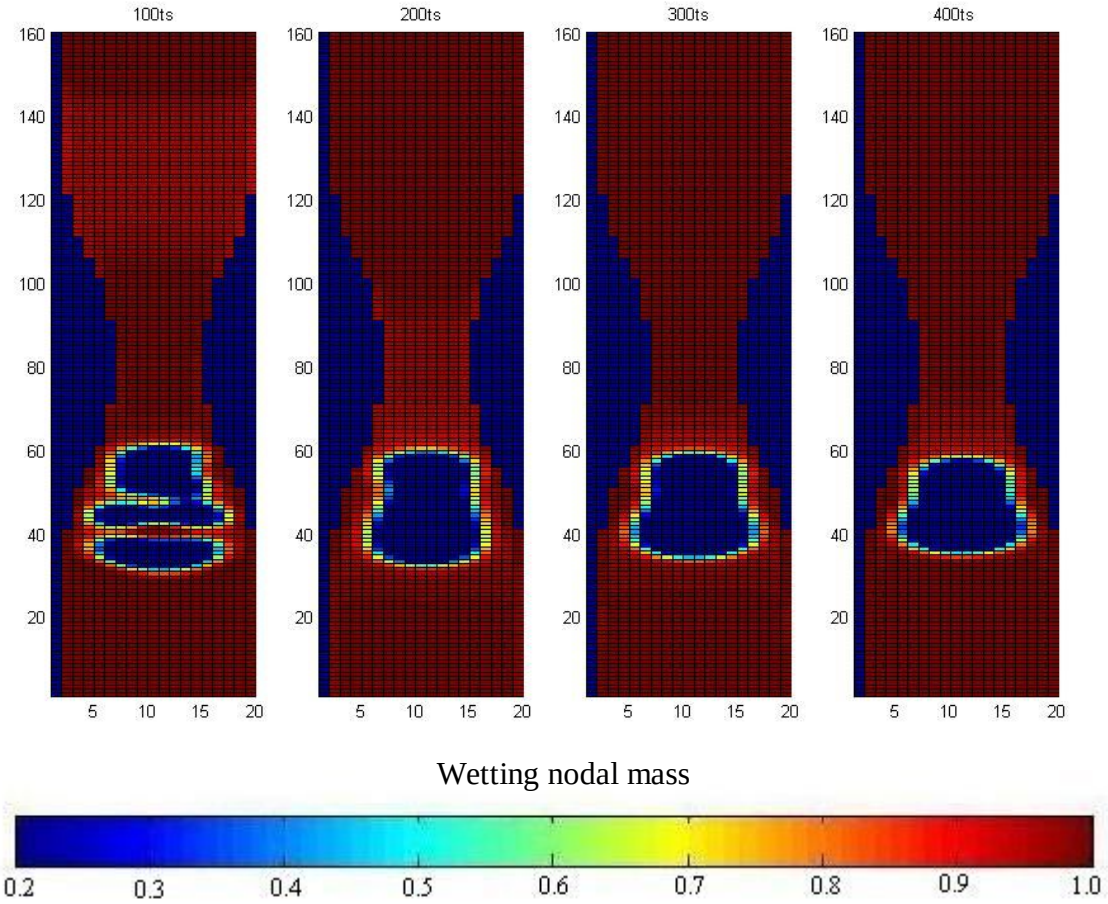


Figure 2.12. Illustration of mixed initial conditions. Here we specified that the mixture only occur between $30 \leq z \leq 60$.

We also allowed the simulation volume to initially be filled with only wetting or only non-wetting fluid. This was useful in simulations where the mixed inlet/infinite outlet boundary conditions were switched on.

We found that if we set the particle density distribution of the non-present fluid to be identically zero, then we created a numerical instability in which the mass of the non-present fluid slowly increased. It was observed that a minute mass of the initially non-present fluid $O(e^{-33})$ was present through the first layer of nodes. This was propagated downstream, increasing slightly with each time step, until it reached the outlet. At this point the mass of the non-present fluid would increase stay at the outlet, but still accumulate mass. This would continue so that after many thousands of time steps there was a significant initially non-present fluid mass infusion, which eventually lead to instabilities. This mass increase and propagation was removed by initializing the non-present fluid with a non-zero, albeit tiny ($O(e^{-10})$) value.

2. Divided phases

Initializing the simulation with only wetting fluid in part of the system and only non-wetting fluid in the other part proved useful in some situations for example investigating the dynamic contact angle in Hele Shaw cells (Chapter 4).

3. Bubble

For the Laplace experiments, we initialized the simulations by placing a predefined non-wetting bubble in the middle of a sea of wetting fluid. Although the size and density of the bubble still needed to adjust to get into equilibrium with the surrounding wetting fluid, this took less computational time then allowing a mixture of the fluids to separate.

D. Wettability

As previously mentioned, the wettability of the solid was created by allowing the solid nodes to assume some virtual wetting mass in the density gradient calculation of the adjacent fluid nodes. Interestingly, we found that a stronger wettability effect is not created when the wetting mass is increased on the solid nodes; rather, a stronger wettability effect is created when the non-wetting fluid is given a negative virtual mass on solid nodes. Note that this negative virtual mass is stationary – it does not get propagated into the fluid, and so larger and larger density gradients are not created, as in instability feedback mechanism. However it appears that having a negative non-wetting mass at the solid node maintains a positive non-wetting density gradient away from the wall, thus ensuring that the adjusted non-wetting fluid momentum is always pointing away from the wall.

We found significant improvement from having $\rho'_{sn} = 0$ to $\rho'_{sn} = -1$, as shown in Figure 2.13 below. We also saw a decreasing improvement as we decreased $\rho'_{sn}$. One can see that the wetting particle density distributions increase slightly between the non-wetting bubble and the vertical solid walls from $\rho'_{sn} = -1$ to $\rho'_{sn} = -5$. A small increase in wetting density can be seen from $\rho'_{sn} = -5$ to $\rho'_{sn} = -10$ along the walls above and below the closest point of the non-wetting bubble. In our simulations we use $\rho'_{sn} = -10$.

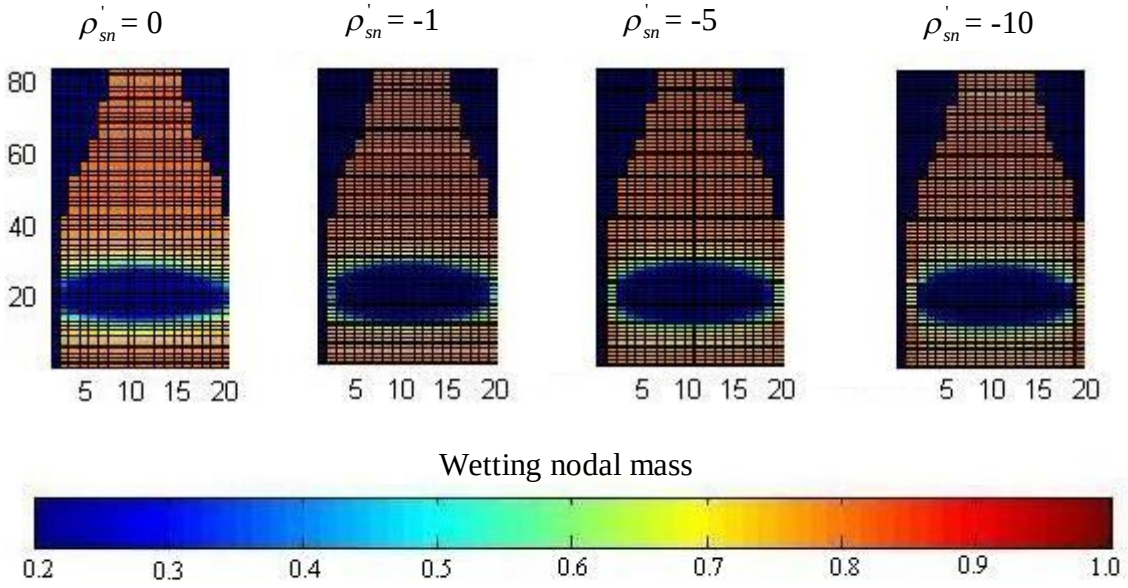


Figure 2.13: The effect on wettability of decreasing the virtual non-wetting mass on solid nodes. Each image was taken at 300 time steps, with a virtual wetting mass at the solid nodes, $\rho'_{sw}$ = 1. The virtual non-wetting mass at the solid nodes, $\rho'_{snw}$ is varied. Note that as $\rho'_{snw}$ is made negative, the wetting behavior of the fluid appears to improve. There is a marginal improvement as $\rho'_{snw}$ is decreased from -5 to -10. In our calculations, we keep $\rho'_{snw}$ = -10.

## 2.5 Phenomenological Issues

### A. Z-momentum banding

Repetitive lines of high and low momentum along the z-axis, or banding, appears in the z-momentum distribution apparently whenever the z-momentum becomes small, as occurred for example whenever a non-wetting bubble became lodged in a constriction. The banding can be in Figure 2.14 particularly at 45,000 time steps but also at all subsequent times as differences in color (z-momentum) in adjacent horizontal bands above the lodged bubble. The color contrast of the adjacent bands is most intense just above (downstream) of the bubble.

Note that the banding appears once the z-momentum is very small, and appears to oscillate about zero. The wavelength of the oscillation appears to be 2 lattice lengths – leading to the idea that the banding is numerical in nature. To investigate this idea, we took a closer look at the x, y and z-momentum distributions for the wetting fluid in the blocked flow simulation at 200,000 time steps.

Figure 2.15 shows that the same high frequency momentum oscillations are observed in the x and y directions. Again the wavelength of each of the oscillation is 2 lattice lengths. Given that there are no forces in the x or y direction, this gives further evidence that the oscillations are numerical and not the manifestation of any physical motion. Furthermore since the momentum field oscillates about zero and there is no flow in the x or y directions, we could postulate that where banding occurs, the actual x, y and z momentum values should be taken to be the mean of the oscillation.

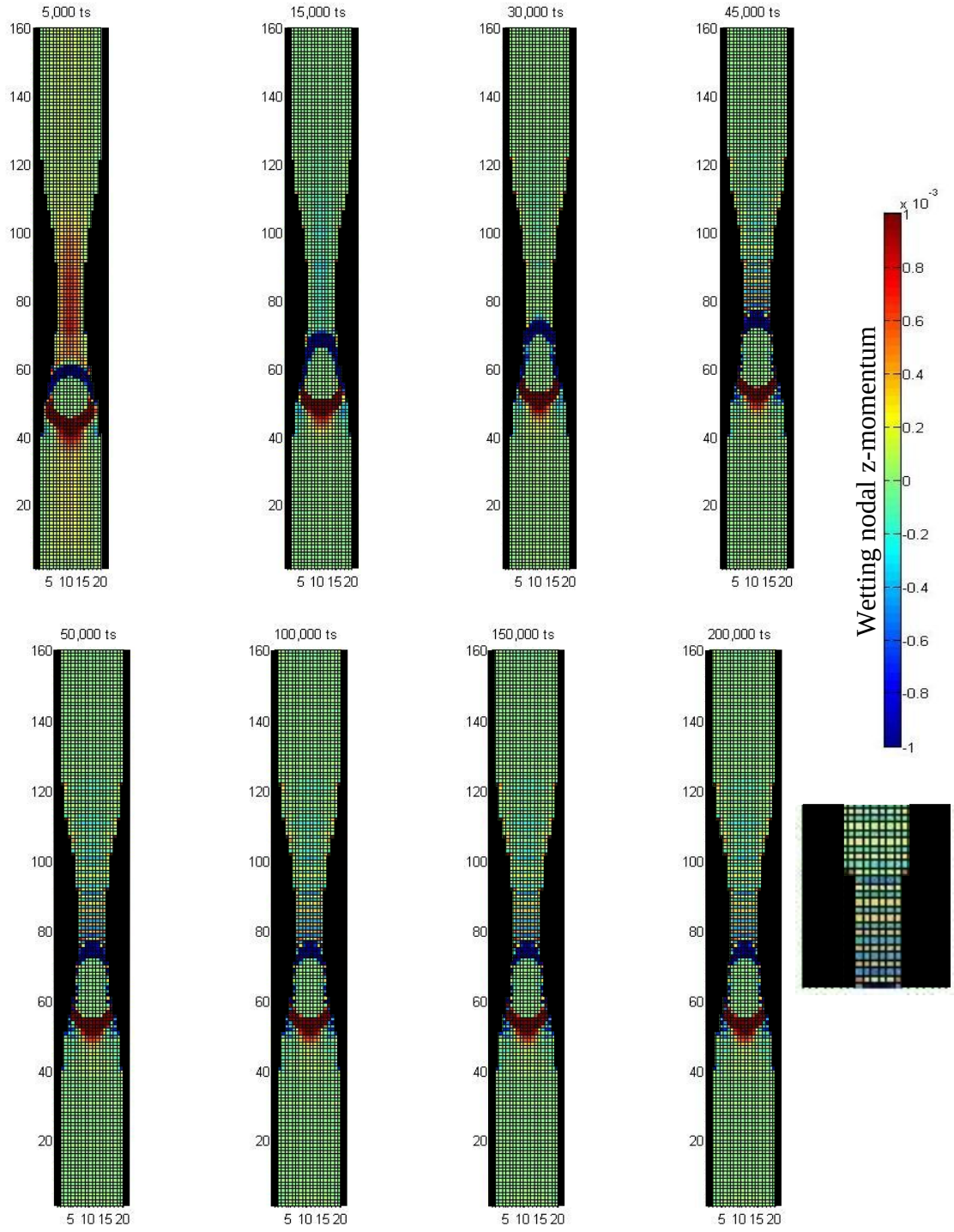


Figure 2.14: Z-momentum results for the capillary seal experiment, reproduced from Chapter 3, Figure 3.10. All z-momentum are snap-shots taken through the central z plane of the tube.

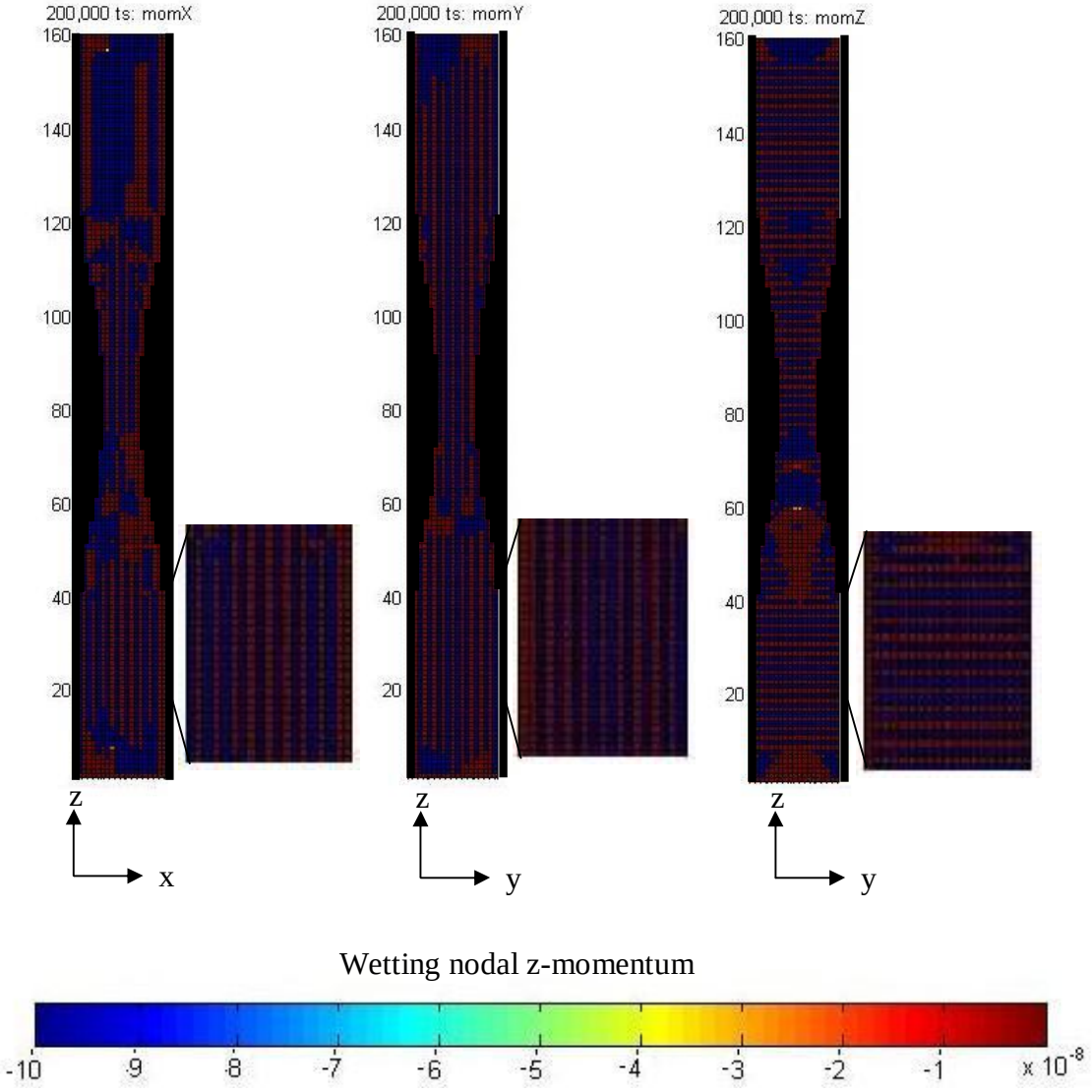


Figure 2.15: The x, y and z-momentum of the wetting fluid taken at 200,000 time steps, through the center plane.

B. Interfacial momentum caps

For all simulations there are distinct regions of strong z-momentum distributions which are appear to be against the flow of the fluid and which always seem to appear at interfacial regions. For example, in Figure 2.14 these regions can be seen as caps on the non-wetting bubble. We expect that the wetting fluid should show z-momentum directed away from the non-wetting bubble, but as shown in Figure 2.14, the reverse is true. The wetting fluid z-momentum indicates that the wetting fluid is being pushed towards the bubble.

These inverse z-momentum regions may be understood through a detailed look at how and when the momentum values are calculated. Following Ladd and Verberg [42], the momentum is calculated from the post-translation, pre-collision particle density distributions in the following manner:

$$\rho u_\alpha = \sum_{i=1} f_i e_{i\alpha} \qquad \ldots(2.37)$$

Where α is x, y or z, $f_i$ is the particle density distribution in the $i^{th}$ direction and $e_{i\alpha}$ is the α component of the velocity vector in the $i^{th}$ direction.

The reversed z-momentum in interfacial regions may be explained by the post translational particle density distributions not yet having taken into account the other particle's density gradient. Figure 2.16 illustrates this. In Figure 2.16b the post-translational density gradient of the central node is the inverse of the global density gradient prior to translation (Figure 2.16a). Using Eq. 2.37 the z-momentum for the post-translational node would point downwards, since the downwards pointing link have a greater density than the upwards pointing links. After the collision, the particle density distributions are adjusted by the presence of the other fluids density gradient.

Where the other fluid's density gradient is strong, the central node's density gradient and therefore the nodal z-momentum is reversed as shown in Figure 2.16c.

In regions where the density gradient of the other fluid is small, the momentum vector shouldn't switch directions between the translation and collisional steps.

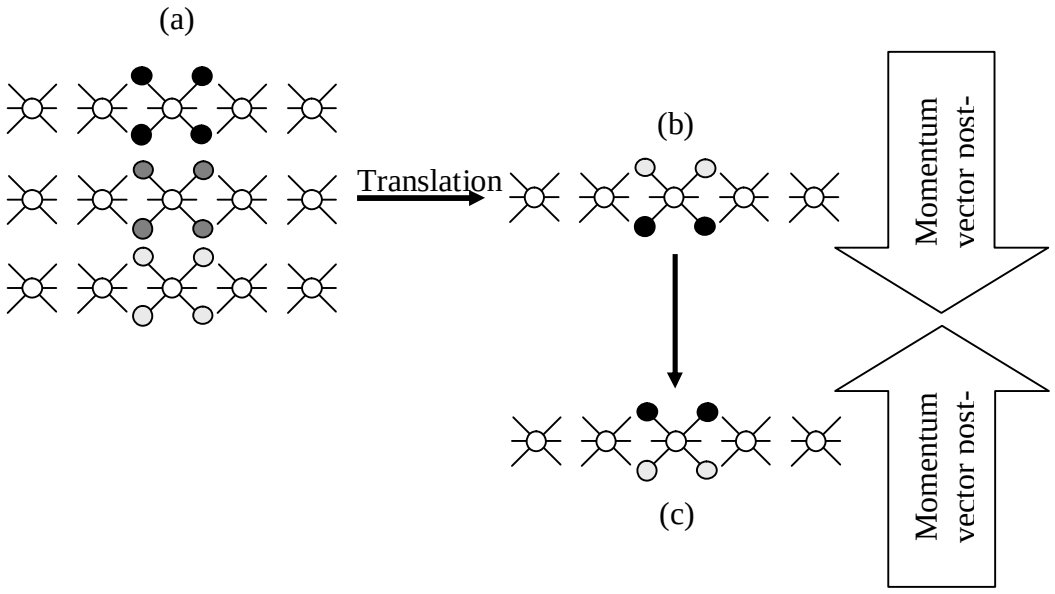


Figure 2.16: Illustration of the momentum vector calculations post translation (recorded) and post-collisional (actual), using the 2D FHP grid for simplicity. Gray scale reflects the particle density (darker means a higher particle density distribution).

C. Re-circulation about the inlet and outlets

Figure 2.15 brings into focus an additional question concerning the z-momentum of the wetting fluid once the pore has become blocked. Other than the banding, Figure 2.15 also shows a positive wetting fluid z-momentum in the middle of the tube at both the inlet and outlet, and a negative wetting fluid z-momentum at the interface of the boundaries with the solid.

Similar patterns are observed in for the x and y momentum components. Such x,y and z distributions lead to the hypothesis that a recirculation flow has built up at the boundaries.

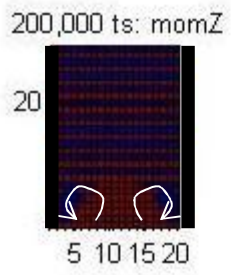


Figure 2.17: Zoom in on the detailed z-momentum at the inlet at 200,000 time steps, through the center plane. The white arrows indicate the apparent recirculation flow direction.

This density pattern can be understood to result from the applied fixed pressure boundary conditions. These conditions are applied by placing the same particle density distributions on all the links of the node. Those links having velocities with both perpendicular and parallel components (radial) to the boundary would be given a radial momentum which is largely absence in the rest of the fluid body. Therefore as these particle distributions are propagated to the next layer of nodes, the increased

radial momentum is also shifted outwards. The re-circulation observed above could be the stable consequence of this imposed and increased radial momentum. It was found that by reducing the imposed radial densities on the boundary links, the recirculation pattern was reduced. However the pressure at the boundaries was also reduced in a less well defined way.

Since this recirculation appeared to be numerical and local in nature, it does not affect any of the overall results obtained with the fixed pressure boundary condition.

## 2.6 Validation Tests

We use the LBM Shan and Chen model for our simulations. In order to show that our model behaves as a fluid we undertook some validation tests. We first tested the fluid dynamics of a single phase by replicating Poiseuille flow. We also showed that two fluids, initially mixed separate as expected. Finally, we replicated Laplace's law and showed how the interfacial tension depends on g.

### A. Poiseuille flow

The equation governing Poiseuille flow (i.e. flow through a tube under a pressure gradient) states that:

$$Q = -\frac{\pi r^4}{8\mu}\frac{dP}{dz}, \qquad \ldots(2.38)$$

where Q = total flow through each plane, r is the radius of the tube and $\mu$ is the viscosity. By replicating Poiseuille flow we obtained empirical values for Q and the

pressure gradient which allowed us to calculate $\mu$. We then compare our empirically determined value of $\mu$ to the theoretical value as given in Eq. 2.16.

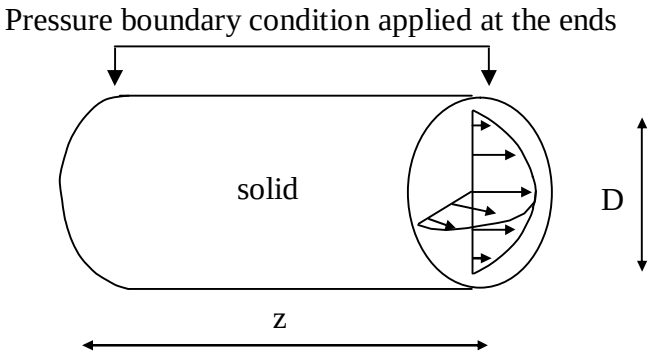


Figure 2.18: The grid used to simulate Poiseuille Flow

We use a tube of radius 9 lattice lengths and length 40 lattice lengths in which we placed a single-phase fluid of mean density = 10 lattice mass unit per node, $g_{ww}$ = $g_{nn}$ = 0 and g = -0.05. We applied the non-periodic pressure boundary conditions as described in Section 2.4B. The resulting density variation across the tube is shown in Figure 2.9. Figure 2.19 shows the average density in each of the planes cutting perpendicularly across the tube. Since $P = \frac{1}{3}\rho$ (in a 3D system, see Eq. 2.22), this indicates that the pressure gradient decreases linearly from end to the other, and that the pressure gradient is given by: $dP/dz = \frac{1}{3}d\rho/dz$.

The flow across the tube is given by the total number of particles moving from one plane into the next at each time step. This is equivalent to the total momentum at each plane at a given time step as shown in Figure 2.20.

From Figure 2.19 we obtained a value for $dP/dz = 0.001$. From Figure 2.20 we obtained a value of Q = 15.43. Using a radius of 9 lattice lengths, we then calculated a viscosity $\mu_{experiment}$ = 1.6698 from Eq. 2.37 as compared to a theoretical value $\mu_{theory}$ = 1.6667, using Eq. 2.16.

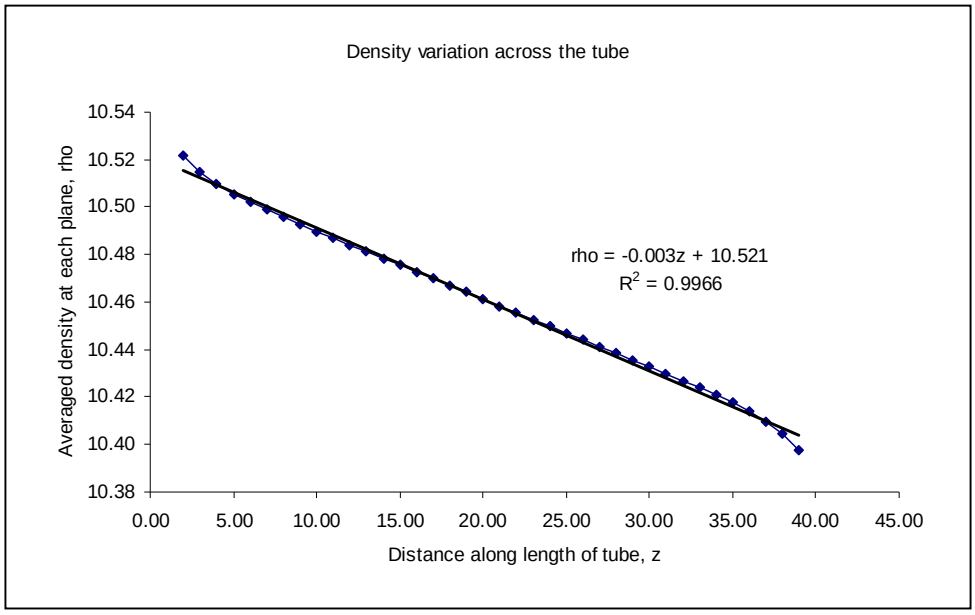


Figure 2.19: Graph showing the density variations across the tube as a result of the fixed density boundary conditions

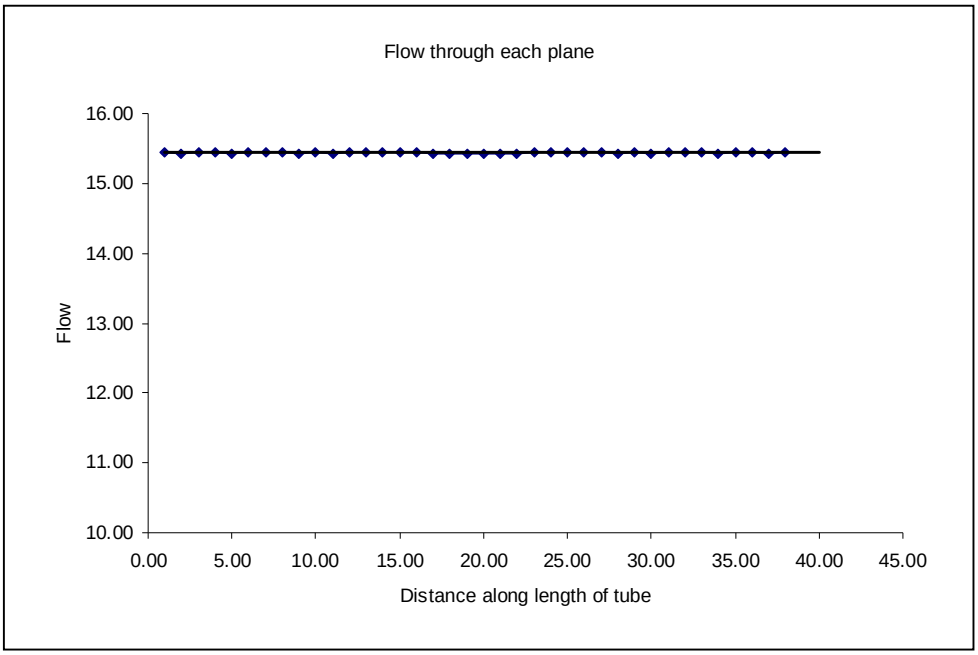


Figure 2.20: Total momentum at each plane, or, equivalently the number of particles passing each plane, each time step.

B. Illustration of separation of initially mixed fluids

We then implemented the Shan-Chen procedure for simulating immiscible fluids, using two identical fluids both of mean density = 10 lattice mass unit per node, $\tau$ =1, and $g_{ww} = g_{nn} = 0$ and g = -0.05. The grid consisted of a cube 30 lattice units on a side. Initially the wetting and non-wetting particles were randomly distributed within the system and all boundaries were defined as being periodic. The system then evolved over 1,000 time steps, as shown in Figure 2.21. This figure shows the density of only one fluid, where dark indicates a high density and light indicates low density (i.e. the other fluid). Initially the sections are gray because the two fluids are mixed. Over time, we see the fluids separate into layered phases. Layers are the equilibrium state for immiscible fluids in a periodic box [12]. There are no inherent differences between the fluids, and imposed interaction with the solid boundary determines which phase is the wetting fluid and which phase is the non-wetting fluid. In the absence of any solid boundaries, there is no reason one phase should form a bubble and not the other. Thus planar layers are formed. From this one can see that interfacial tension is really a phenomenological effect rather than a result of any inherent aspect of the fluids themselves. A real non-wetting fluid introduced into a wetting fluid will form a bubble regardless of how distant the container walls.

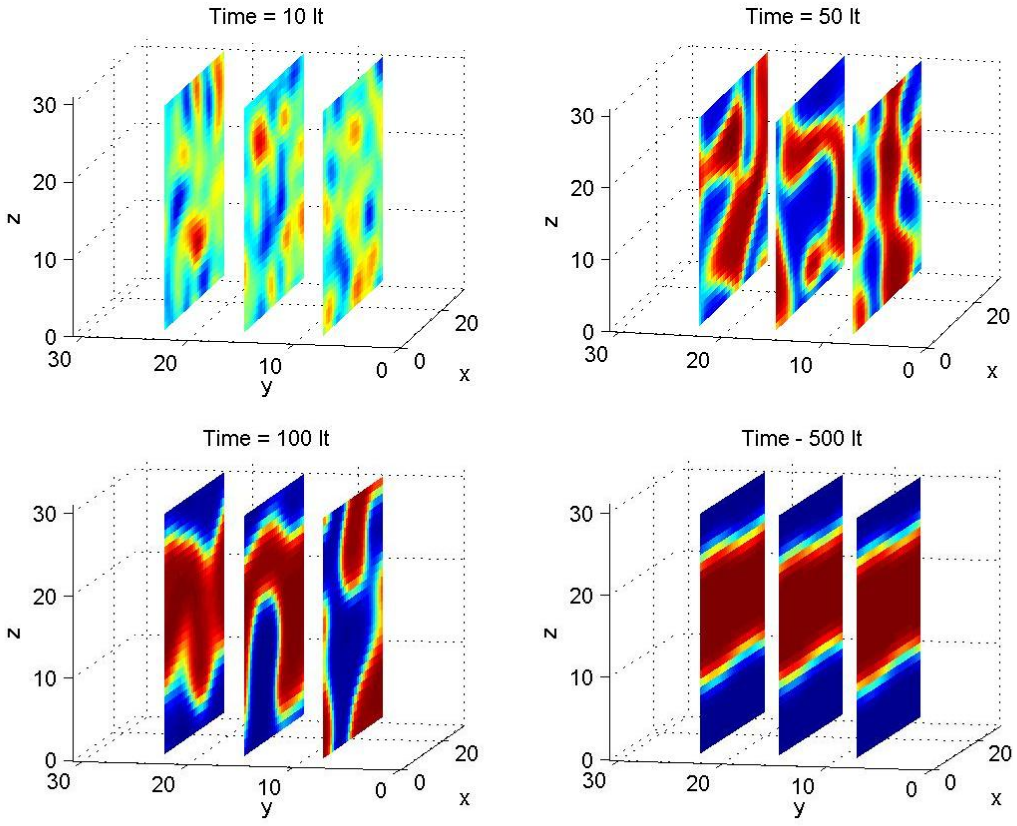


Figure 2.21: Illustration of the separation of two immiscible fluids.

C. Laplace's law

Finally we show that Laplace's law is obeyed. We placed a sphere of the non-wetting fluid in the center of a box filled with wetting fluid of dimension 20 lattice units. Both fluids had a mean nodal mass = 0.1 units, $\tau$ =1, $g_{ww} = g_{nn} = 0$ and we vary $-0.8 \leq g \leq -1.05$. A series of experiments were undertaken, each time a non-wetting sphere with a different diameter was placed into the box. After equilibrium is reached (~ 1,000 time steps) we measured the number of nodes containing the modal wetting and non-wetting densities outside and inside the bubble respectively. These modal densities were generally the maximum densities of each fluid. From these densities, the average pressure inside and outside of the bubble was calculated using Eq. 2.22. The bubble radius coincided with the center of the interfacial region. This radius was estimated by a two stage process:

-The spherical volume of the non-wetting fluid bubble was found from the number of nodes containing the modal non-wetting density. The non-wetting fluid estimate of the radius was then derived from this volume.

-The number of nodes containing the modal wetting fluid density was counted. This was removed from the total number of nodes to find the volume of the spherical void left by the modal wetting fluid. The wetting fluid estimate of the radius was then derived.

The actual radius of the non-wetting bubble was calculated to be the average of these radii. This is illustrated in Figure 2.22 below.

Using these definitions of the densities and the radius, we then calculated the capillary pressure ( $P_c = P_{wetting\ fluid} - P_{non-wetting\ fluid}$ ) and plotted this against 1/r, as in Laplace's law. An example of the results for g =-1.05 is shown in Figure 2.23. The remaining results are shown in Appendix C. In all cases, the linear relationship

between $P_c$ and 1/r was replicated. Figure 2.24 illustrates the relationship between the calculated interfacial tension and the value of g.

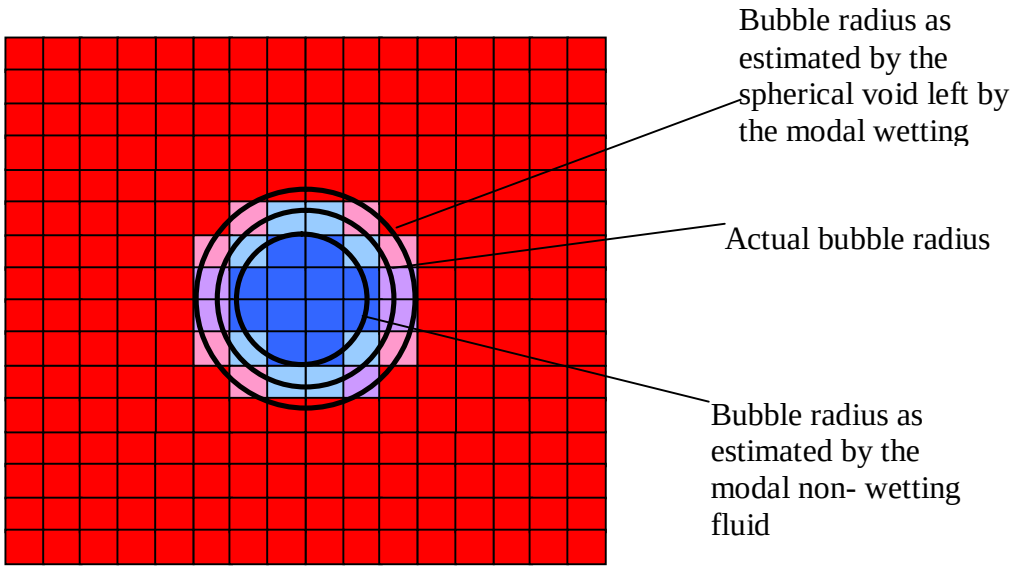


Figure 2.22: Illustration of bubble radius calculation. The bubble radius, shown by the middle black circle is taken to be the average of the radius as estimated by the non-wetting fluid (inner black circle) and that estimated by the wetting fluid (outer black circle).

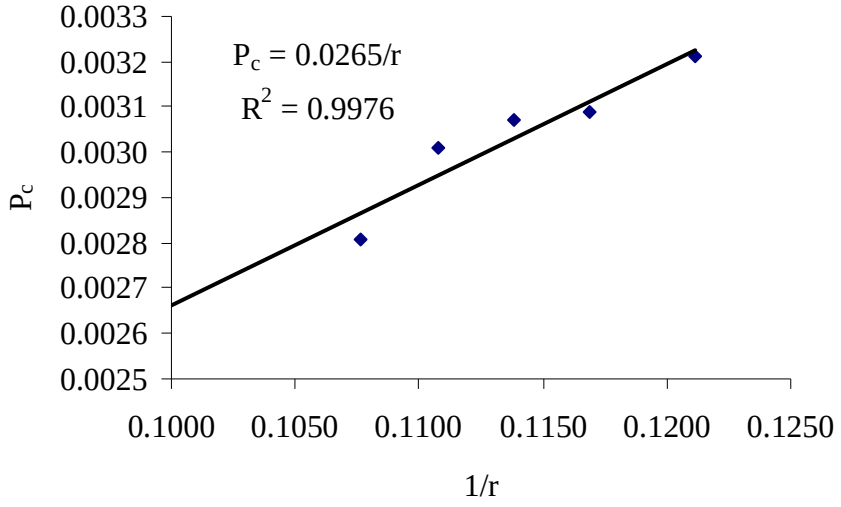


Figure 2.23: Illustration of Laplace' for g = -1.05.

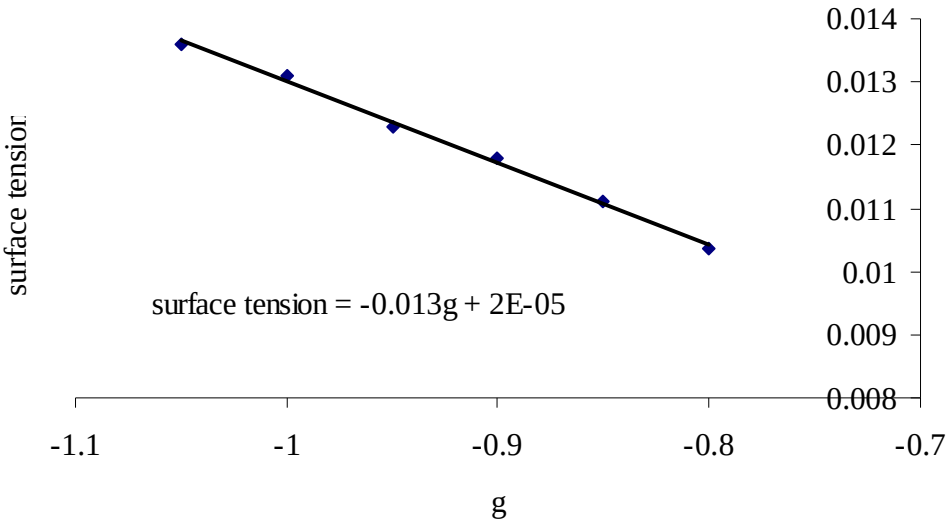


Figure 2.24: Correlation between g and interfacial tension.

# REFERENCES


1. Von Neumann J., *Theory of Self Reproducing Automata*, ed. Bucks A. W. 1966: Univ. of Illinois Press.

2. Von Neumann J., *Essays on Cellular Automata*. 1970: Univ. of Illinois Press.

3. Kadanoff L. P. and Swift J., *Transport Coefficients Near Critical Point: A Master Equation Approach.* Phys. Rev., 1968. 165: p. 310-322.

4. Hardy J., de Pazzis O., and Pomeau Y., *Molecular Dynamics of a Classical Lattice Gas: Transport Properties and Time Correlation Functions.* Phys. Rev. A, 1976. 13: p. 1949-1961.

5. Frisch U., Hasslacher B., and Pomeau Y., *Lattice-Gas Automata for the Navier Stokes Equation.* Phys. Rev. Lett., 1986. 56.(14): p. 1505-1508.

6. Wolfram S., *Cellular Automaton Fluids: Basic Theory.* J. of Stat. Phys., 1986. 45(3-4): p. 471-526.

7. Wolfram S., *Statistical-Mechanics of Cellular Automata.* Rev. Modern Phys., 1983. 55(3): p. 601-644.

8. Wolfram S., *Theory and Applications of Cellular Automata*. 1988: World Scientific.

9. D'Humieres D., Lallemand P., and Frisch U., *Lattice Gas Models for 3D Hydrodynamics.* Europhys. Lett., 1986. 2(4): p. 291-297.

10. D'Humieres D. and Lallemand P., *Numerical Simulations of Hydrodynamics with Lattice Gas Automaton in Two Dimensions.* Complex Sys., 1987. 1: p. 599-632.

11. Frisch U., et al., *Lattice Gas Hydrodynamics in Two and Three Dimensions.* Complex Sys., 1987. 1: p. 649-707.

12. Rothman D. and Keller J. M., *Immiscible Cellular Automaton Fluids.* J. Stat. Phys., 1988. 52( 3-4): p. 1119 -1127.

13. Succi S., *The Lattice Boltzmann Equation for Fluid Dynamics and Beyond*. 1 ed. 2001, Oxford: Oxford University Press.

14. Qian Y. H., d'Humieres D., and Lallemand P., *Lattice BGK Models for Navier-Stokes Equation.* Europhyics Letters, 1992. 17(6): p. 479-483.

15. Qian Y. H. and Orszag S. A., *Lattice BGK Models for the Navier-Stokes Equation - Nonlinear Deviation in Compressible Regimes.* Europhysics Letters, 1993. 21(3): p. 255-259.

16. Higuera F. J., Succi S., and Benzi R., *Lattice Gas Dynamics with Enhanced Collisions.* Europhys. Lett., 1989. 9(4): p. 345-349.

17. Higuera F. J. and Jimenez J., *Boltzmann Approach to Lattice Gas Simulations.* Europhys. Lett., 1989. 9: p. 663-668.

18. Chen S., et al., *Optimal Initial Conditions for Lattice Gas Hydrodynamics.* Phys. Rev. A, 1989. 39: p. 2725-2727.

19. Chen S. and Doolen G., *Lattice Boltzmann Method for Fluid Flows.* Annu. Rev. Fluid Mech., 1998. 30: p. 329-364.

20. Hardy J., Pomeau Y., and de Pazzis O., *Thermodynamics and Hydrodynamics for a Modeled Fluid.* J. Math. Phys., 1972. 13(7): p. 1042.

21. Hardy J., Pomeau Y., and de Pazzis O., *Time Evolution of a 2-Dimensional Model System. 1. Invariant States and Time Correlation-Functions.* J. Math. Phys., 1973. 14(12): p. 1746-1759.

22. Benzi R., Succi S., and Vergassoa M., *The Lattice Boltzmann Equation-Theory and Applications.* Phys. Rep., 1992. 222(3): p. 145-197.

23. D'Humieres D. and Lallemand P., *Flow of a Lattice Gas Between Two Parallel Plates- Development of the Poiseuille Profile.* C. R. Acad. Sci. Paris, 1986. 302(16): p. 983.

24. Kadanoff L. P., McNamara G. R., and G. Zanetti, *From Automata to Fluid Flow-Comparisons of Simulation and Theory.* Phys. Rev. A, 1989. 40(8): p. 4527-4541.

25. Rothman D., *Macroscopic Laws for Immiscible Two-Phase Flow in Porous Media: Results from Numerical Experiments.* J. Geophys. Res., 1990. 95(B6): p. 8663-8674.

26. Orszag S. and Yakhot V., *Reynolds Number Scaling of Cellular Automaton Hydrodynamics.* Phys. Rev. Lett., 1986. 56: p. 1691.

27. Succi S., Santangelo P., and Benzi R., *High Resolution Lattice Gas Simulation of Two-Dimensional Lattice Gas Turbulence.* Phys. Rev. Lett., 1988. 60: p. 2738.

28. McNamara G. R. and Zanetti G., *Use of the Boltzmann Equation to Simulate Lattice Gas Automata.* Phys. Rev. Lett., 1988. 61: p. 2332-2335.

29. Dahlburg D., Montgomery D., and Doolen G. H., *Noise and Compressibility in Lattice-Gas Fluids.* Phys. Rev. A, 1987. 36(5): p. 2471-2474.

30. Huang K., *Statistical Mechanics*, ed. Wiley. 1987, New York.

31. Bhatnagar PL., Gross EP., and Krook M., *A Model for Collision Processes in Gases 1: Small Amplitude Processes in Charged and Neutral One Component System.* Phys. Rev., 1954. 94: p. 511-525.

32. Chen H., Chen S., and Matthaeus W. H., *Recovery of the Navier-Stokes Equations using a Lattice-Gas Boltzmann Method.* Phys. Rev. A, 1992. 45(8): p. R5339-R5342.

33. Qian Y. H., d'Humieres D., and Lallemand P., *Advances in Kinetic Theory and Continuum Mechanics, Book in Honor of H. Cobannes,*, Gatignol R. and Soubbaramayer J. B., Editors. 1991, Springer Verlag. p. 127.

34. Ladd A., *Numerical Simulations of Particulate Suspensions via a Discretized Boltzmann Equation. Part 1: Theoretical Foundations.* J. Fluid Mech., 1994. 271: p. 285.

35. Gunstensen A. K., et al., *Lattice Boltzmann Model of Immiscible Fluids.* Phys. Rev. A, 1991. 43(8): p. 4320-4327.

36. D'Ortona U., et al., *Two-Color Nonlinear Boltzmann Cellular Automata: Surface Tension and Wetting.* Phys. Rev E, 1995. 51: p. 3718-3728.

37. Shan X. and Chen H., *Lattice Boltzmann Model for Simulating Flows with Multiple Phases and Components.* Phys. Rev E., 1993. 47: p. 1815-1819.

38. Swift M., Osborn W.R., and Yeomans J. M., *Lattice Boltzmann Simulation of Nonideal Fluids.* Phys. Rev. Lett., 1995. 75(5): p. 830-833.

39. Swift M., et al., *Lattice Boltzmann Simulation of Liquid Gas and Binary Fluid Systems.* Phys. Rev. E., 1996. 54(5): p. 5041-5052.

40. Hazi G., et al., *Lattice Boltzmann Methods For Two Phase Flow Modeling.* Annuals of Nuclear Energy, 2002. 29: p. 1421-1453.

41. Ladd, A.J.C and R. Verberg, *Lattice-Boltzmann Simulations of Particle-Fluid Suspensions.* J. Stat. Physics, 2001. 104(516):p.1191-1251.

# Chapter 3. Capillary Sealing

## 3.1 Abstract

The exact nature of the seals maintaining abnormally pressured compartments in sedimentary basins is not well understood, despite decades of research. We use the Lattice Boltzmann method of Shan and Chen [1] for immiscible fluids to investigate a novel idea that capillary pressures alone are able to seal in the observed abnormal pressures. A capillary seal forms when a non-wetting fluid phase is generated within or introduced into grain sized layered sediment and the pressure drop across the coarse/fine interface is less than the capillary pressure. For such seals to maintain abnormal pressures, both phases must be blocked, the capillary pressure drops must be accumulative over many fine/coarse interfaces and the seals must be able to re-form after rupture. We show all three to be true, and hence lay the numerical foundation for the validity of capillary seals.

## 3.2 Introduction

Over 80% of the world's oil basins show some degree of over pressuring or under pressuring [2]. In the mid 1970's Bradley [3] suggested that the abnormal (non-hydrostatic) pressures found deep in sedimentary basins were actually seals surrounding hydrostatically over or under pressured fluids confined in compartments. Many ideas have been put forward as to the cause of the abnormally pressured compartments: generation of hydrocarbons [4-6] rapid sedimentation or erosion of impermeable strata [4, 5, 7], tectonic compression or dilation [3, 8]. In 1987 Powley [9] asked the Gas Research Institute (GRI) to verify in the public literature that compartments and seals exist, and to investigate the causes of this pressure compartmentation. In the following decade, a general consensus developed that

abnormally pressured compartments exist and strongly influence the migration and trapping of hydrocarbons in basins [2, 3, 10-15]. However, the nature of the seals that surround the compartments has remained enigmatic. Top seals are commonly assumed to be low permeability strata, such as shale [16, 17]. However, top seals are generally encountered at ~3km depth and thus must move upwards as sediments are deposited [2]. Seals have also been shown to cut across regional stratigraphy [16]. These characteristics are incompatible with a seal being a single lithologic unit. Furthermore it has been shown that the seal permeability required to maintain the observed overpressures over geological time [18] is lower than laboratory measurement of sediments such as shale. Low permeability units exposed to chemical alteration was another hypothesis. However, an unreasonable volume of fluid flow is necessary to sufficiently alter the strata to achieve the necessary permeability [19].

Cathles [20] suggested that the capillary pressures may be sufficient to seal in the observed abnormal pressures. As a thought experiment, take a sedimentary environment in which there is a gas/water mixture. Due to capillary forces, gas would be expelled from the fine grained pores, with water being drawn in. Conversely gas would be drawn into the coarse grained sediment and water expelled. Once this occurred within many pores, fluid flow would be diverted through the remaining unblocked pores. Even if the non-wetting fluid saturation is small, once the non-wetting phase is brought to a pore, it too would become blocked. This process would continue until all pores are blocked and a seal is formed. The addition of such capillary pressure drops across many coarse/fine layers could form strong seals. This concept is different from the capillary barriers under which hydrocarbons are commonly trapped. Here, hydrocarbons columns are trapped below anticlinal structures that are a small fraction of the total area of the stratigraphic horizon. Consequently, there are many places along the horizon which only contain only water.

Whilst water may be blocked within the pores containing two phases, water is not blocked from pores containing just water. The concept that flow will bring a small amount of non-wetting fluid to all the fine pores in a layer and that the resulting capillary barriers will be a seal for both non-wetting and wetting phases is novel. These capillary seals, if formed, could answer many of the enigmas surrounding what is known about the abnormally pressured compartments.

If a seal could form from the presence of two phases within a fine/coarse interface, then this would allow the seal to re-heal if ruptured, and the sealing location could rise through the stratigraphy as sedimentation occurs. The seal could cut through multiple lithologies, since the formation of the seal is based upon relative pore sizes rather than absolute pore sizes. It has been noted [21] that in some basins, the top of the over pressure (TOOP) broadly coincides with the depth (~3km) at which gas exsolves from a super critical gas/oil-water mixture. Cathles noted [20] that since the interfacial tension of gas/water is about twice that of supercritical gas-oil/water; the presence of gas/water could form a seal at the TOOP, whilst the presence of the supercritical oil-gas/water mixture could give rise to the weaker internal compartmentation, providing a possible explanation of the formation of the "megacomplex" compartmentation observed in the Anadarko Basin, as described by Al Shaieb [22, 23].

The hypothesis we investigate here is that seals result from the presence of more than one fluid phase in grain-size layered sediment. When two immiscible phases are located in layered sediment, the non-wetting phase is blocked at the smaller pore throats of the fine layer and we hypothesize that this prevents the movement of both phases, unless the pressure across the fine layer exceeds that required to push the non-wetting phase through. We investigate the ability of the capillary seals to re-heal, the additive nature of the capillary pressure drop over multiple pores in series, and the

minimum non-wetting saturation required for a seal to form.

Shosa [19, 24] undertook an experiment to investigate capillary pressure as a sealing mechanism. An 0.5m long stainless steel tube with an inner diameter 12.7mm was filled with coarse-grained quartz (45 $\mu m$ - coarse silt size) and, in three separate experiments, 2, 5 and 8 layers of fine-grained quartz (2 $\mu m$ - very fine silt to clay size) were placed in the middle of the tube. At the beginning of each experiment the tube was evacuated and then filled with $CO_2$, displacing any residual air. The tube was then evacuated again and filled with water, which was then displaced with water saturated with $CO_2$. This procedure ensured that there was only one fluid phase in the tube at the beginning of each experiment. The pressure across the tube was then reduced and $CO_2$ allowed to exsolve, forming two phases. Once equilibrium had been reached (after ~ 1 hour), for a gas saturation of ~ 50%, no detectable flow was observed over the rest of the experimental period of up to three weeks.

Shosa found that the permeability of this layered porous media could easily be reduced by over seven orders of magnitude by simply exsolving a non-wetting phase. Furthermore, the pressure drop across each interface was just that required to force gas into the finer layers, and the total pressure drop across the tube increased linearly with the number of the fine layers. The experiment verified that the pressure drop across fine/coarse interfaces is cumulative. (See Figure 3.2). Shosa also measured the temperature dependence of the pressure drops across the tube. She found that the temperature dependence of the overall pressure drop agreed exactly with the temperature dependence of the water-$CO_2$ interfacial tension. This result provides strong evidence that the sealing mechanism is capillary and not a relative permeability effect.

The flow blockage was modeled successfully using Laplace's Law. As shown in Figure 3.1, capillary forces cause the non-wetting pressure in a capillary tube to

exceed that of the wetting fluid by $2\sigma/r$, where $\sigma$ is the interfacial tension and *r* is the radius of the tube. Thus forcing non-wetting fluid into a fine pore will require a pressure difference across the pore, $\delta P_i$:

$$\delta P_i = 2\sigma\left(1/r_{fine} - 1/r_{coarse}\right), \qquad \ldots(3.1)$$

and flow across fine layers will require a pressure drop across each fine layer as illustrated in Figure 3.2. The overall pressure drop across the tube shown in Figure 3.2 is the sum of the pressure drops across each fine layer:

$$\Delta P = \sum_i \delta P_i \ . \qquad \ldots(3.2)$$

Eqs. 3.1 and 3.2 account for all aspects of Shosa's experiment, including the temperature-dependence of the pressure drop [23].

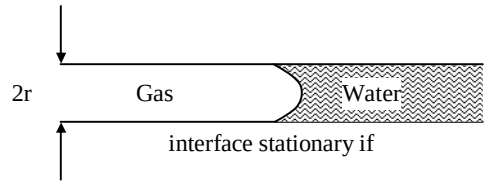


$$P_{gas} - P_{water} = \frac{2\sigma Cos\theta}{r} \approx \frac{2\sigma}{r}$$

Figure 3.1: The pressure conditions in the gas and water phases that must pertain if an interface between them is stationary.

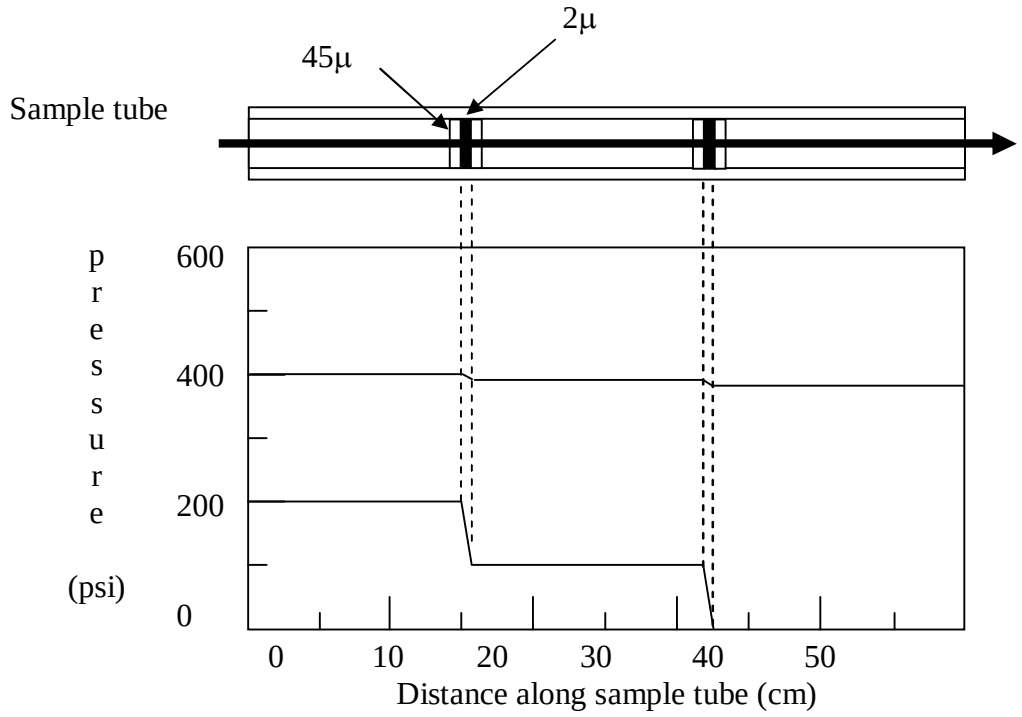


Figure 3.2: Experimental results from the Shosa experiment. Reproduced from Shosa 2000 [19].

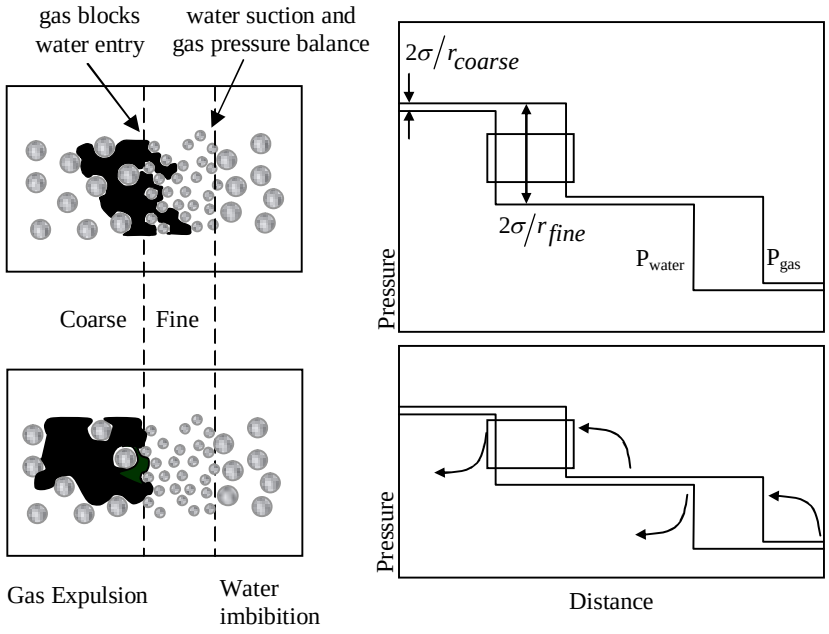


Figure 3.3 Flow is backward when pressure is reduced across a capillary seal, suggesting there can be no flow through such a seal.

The Shosa experiment showed that there was no detectable flow of either fluid through the layered sedimentary system over a period of at least three weeks. Using a physical argument, Shosa and Cathles [24] suggested that there was, in fact, no flow through the system. Non-wetting fluid that is unable to cross a fine layer may still partially penetrate it, as shown by the left top diagram in Figure 3.3. If the pressure across the layer is reduced, capillary suction will cause the fine layer to imbibe water and expel gas as shown in the bottom left diagram in Figure 3.3. The right hand diagrams sketch the pressure profiles of both fluid phases across the fine layers. The discontinuity in the water pressure at the high pressure side of the fine interface (left curve on the right hand diagram in Figure 3.3.) is caused by non-wetting fluid blocking the flow of the wetting fluid. The discontinuity of the pressure in the non-

wetting fluid at the low pressure side of the interface (left curve in the right panels of Figure 3.3) results from capillary forces pulling wetting fluid into the fine layer (but not into the course). The crux of the Shosa and Cathles argument that there is no flow is that if the pressure across a blocked system is reduced, water is drawn into the fine grained media and gas is expelled at the high pressure side, as shown by the arrows in the lower right hand panel. Since the net flow of both the fluids is up the pressure gradient when the pressure is relaxed, e.g., the flow is reversed when pressure across an interface is reduced, the flow must be totally blocked.

The idea that capillary pressures could result in total blockage of both phases is important if non-hydrostatic pressure are to be maintained over millions of years, but the idea that the flow blockage is total has been met with skepticism. The main criticism is that, from a relative permeability perspective, there must always be some, small, flow through the wetting layer that surrounds all mineral grains, even when the thickness of these layers is reduced by a gas bubble pressing against them. The two perspectives seemed at odds, and it was therefore decided to turn to Lattice Boltzmann simulations to seek insights that might resolve the impasse. The Lattice Boltzmann Method (LBM) is well known for the ease at which it models immiscible fluid flow in porous media. Using the LBM, we can observe the velocities and the distribution of the phases through a simplified numerical version of the Shosa experiment. The LBM simulation allows us to determine the minimum amount of gas required for sealing, and to investigate the conditions under which a breached seal can re-heal when pressure is reduced. The simulations reported here suggest that the flow is totally blocked and supports the capillary sealing hypothesis.

## 3.3 The Lattice Boltzmann Method (LBM)

The LBM solves the Navier Stokes equation by computing the movement of distributions of particles on a 2D or 3D cubic lattice. It has been validated extensively whilst being applied for ideal and non-ideal fluids [25–31], for high and low Reynolds number flows [32-34] as well as flows in complex geometries [29, 35-37]. The Lattice Boltzmann Method can be thought of occurring in two steps; translation and collision.

*Step 1 - Translation:* Each cube in the lattice consists of a center point, known as a "node" on which resides $i$ groups of fractional numbers of particles, known as particle density distributions, $f_i$. Each $f_i$ can be thought of residing on the $i^{th}$ link of the central node, where the $i^{th}$ link provides a direct path between the node and its nearest neighbor node in the $e_i$ direction. Each node can be thought of as a center node in its own right.

At the beginning of each time step, $f_i$ moves to the closest node in the $i^{th}$ direction. In our case we use the 3DQ19 lattice, which is a 3D lattice with 19 velocity vectors, including a rest particle density distribution, $f_{i=0}$. The rest particle density distribution has zero velocity and so remains at the node after the translation has occurred. Six of the eighteen velocities are directed towards the center node on the faces of the cube, and twelve are directed to the center node on each of the cube's edges, as is illustrated in Fig 3.4.

*Step 2: Collision:* After translation, the particle density distributions arriving on the same node collide and are redistributed in a manner that conserves mass and momentum. If the fluid is single phase, the choice of redistribution is made randomly. If the fluid is two phases, the redistribution choice for a particle is that which directs a particle toward the greatest adjacent concentration of its phase.

Body forces are applied by changing the overall particle momentum at a node.

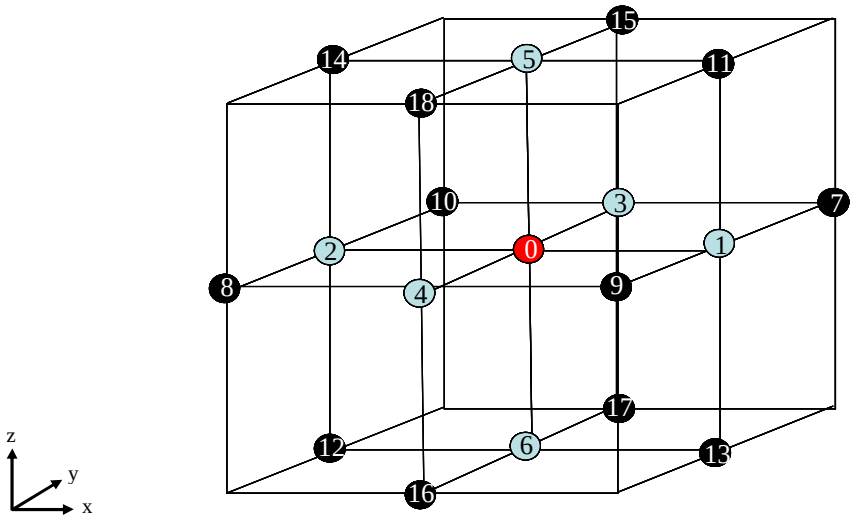


Figure 3.4: A single cube of the LBM lattice is shown, with the locations of the 18 neighbor nodes, color coded by distance from the central node. The central node is red and is the location of the zero-velocity density distribution. The grey nodes are at the center of each of the faces of the cube, and the black nodes are at the middle of each of the edges of the cube.

The LBM equation describing the collision is a discretized version of the Boltzmann equation and can be written [38]:

$$\Delta_i f = -\frac{1}{\tau}(f_i - f_i^{eq}(F_i)), \qquad \ldots(3.3)$$

Here $f_i$ is the particle density distribution at the start of the time step in the $i^{th}$ direction, and $f_i^{eq}$ is the known equilibrium particle distribution, which incorporates any forces on the node, $F_i$. For a single fluid with no applied forces $f_i^{eq}$ is the ideal gas distribution. $\Delta_i f$ is the change in the particle density distribution on the $i^{th}$ link caused by all the collisions that have taken place on the node.

The relaxation time, $\tau$, controls how rapidly the solution converges to its equilibrium state and is related to the viscosity of the fluid. It is specified by the modeler and has units of time step. The Navier Stokes equation is derived by substituting the Chapman-Enskog expansion of the distribution function into the mass and momentum continuum equations [39]. The viscosity of an LBM fluid is then taken from comparing the LBM Navier Stokes equation to the Navier Stokes equation for a macroscopic fluid. The viscosity of an LBM fluid is given by [40]:

$$\mu = \frac{c^2}{D}\left(\tau - \frac{1}{2}\right). \qquad \ldots(3.4)$$

Where c is the unit of velocity in lattice space and c = $\delta_x / \delta_t$. Here $\delta_x$ is the lattice constant and $\delta_t$ is the time step. For simplicity, in most cases, $\delta_x$ = 1 and $\delta_t$ = 1, resulting in c = 1 [36, 40]. D is the dimension of the system, where for flow in three dimensions, D=3. From equation 3.4 we see that $\tau$ must be greater than ½ time step

for physically reasonable viscosities. The unit of viscosity in lattice space is (lattice length)$^2$/time step which corresponds to the MKS units of kinematic viscosity m$^2$/s. Fluid pressure is related to particle density:

$$P = \rho \frac{c^2}{D}, \qquad \ldots(3.5)$$

where $\rho$ is particle density and P is the fluid pressure.

Systems containing immiscible fluids are simulated by placing two particle distributions on each node, one for the non-wetting and one for the wetting fluid, and solving for the motion of each fluid using the LBM method described above. The interactions of the two fluids have been incorporated in several ways [26-29, 1, 41]. We use the LBM immiscible fluid implementation of Shan and Chen and calculate the density gradients for each fluid and apply a force to the particles:

$$F_n = g_{nn} \nabla \rho_n + g_{nw} \nabla \rho_w \qquad \ldots(3.6)$$

$$F_w = g_{ww} \nabla \rho_w + g_{wn} \nabla \rho_n, \qquad \ldots(3.7)$$

where *n* indicates non-wetting and *w* indicates the wetting fluid. Judicious selection of values for $g_{nn}$, $g_{ww}$ and g provide forces that segregate the two fluids and simulate surface tension phenomenon. We follow Shan and Chen [1] by setting $g_{nw} = g_{wn} = g$ and $g_{nn} = 0$. We found that by setting $g_{ww} = 0.05$, we obtained the strongest separation and most distinct solid wetting behavior without the system becoming unstable. Therefore, the segregating force in our simulations is:

$$F_n = \rho_n g \nabla \rho_w \qquad \ldots(3.8)$$

$$F_w = g_{ww}\nabla\rho_w + g\nabla\rho_n \quad \ldots(3.9)$$

Solid nodes are given different interaction parameters, $g_{sw}$ and $g_{sn}$, which define the degree of attraction or repulsion of the wetting and non-wetting fluids for the boundary. The additional force applied due to the presence of a solid is:

$$F_w = \rho_w g_{sw}\nabla\rho_s \quad \ldots(3.10)$$

$$F_n = \rho_n g_{sn}\nabla\rho_s \quad \ldots(3.11)$$

Where $\rho_s$ is the density of the solid nodes surrounding the fluid node.

Particles approaching the solid boundary bounce off the boundary in a fashion that conserves their momentum parallel to the boundary and reverses their momentum perpendicular to the boundary. Pressure can be specified at a boundary by fixing particle density at the boundary nodes. In the following simulations, we initially set the z-boundaries as cyclic, in which the inlet and outlet are linked numerically so that particles leaving one boundary enter the other. The initial conditions are that each node has a wetting particle density of 0.1, which is equally distributed over all 19 links. For a 20 layers of nodes upstream of the constriction, each node also has a non-wetting particle density of 0.1, equally distributed amongst the 19 links. The non-wetting saturation, $S_n$ is defined as:

$$S_n = \frac{\rho_n N_n}{\rho_n N_n + \rho_w N_w} \quad \ldots(3.12)$$

Where $\rho_n = \rho_w$ and $N_n$ is the number of nodes upon which the non-wetting fluid is initially placed. Similarly, $N_w$ is the number of nodes on which the wetting fluid is initially placed, this is equal to the total number of fluid nodes in the system. Using the values of $N_n$ and $N_w$ from the value in Table 3.1, we find that Sn = 10%. As soon as the phases have separated, the cyclic boundary conditions for the wetting phase are replaced by a fixed pressure boundary condition by setting the particle density of the wetting fluid on each node in the entry and exit planes to a specified value. Due to the low non-wetting densities at the boundaries, we allow the non-wetting boundary to remain cyclic. More discussion can be found in Poyurs [42].

We use an LBM computer code developed by Ladd and Verberg [43]. It is a standard implementation of the LBM method of Shan and Chen [1]. The Ladd and Verberg code was modified by us to add Shan and Chen's [1] segregation force for immiscible fluids, and we implemented boundary and initial conditions suitable for capillary seal simulation. We also added various schemes to increase stability of our code. Stability issues are known to arise in the presence of high density gradients [44]. Poyurs [42] shows that high density gradients lead to negative densities, which cause the stability issues. All schemes were introduced to reduce the introduction of negative densities either by removing negative densities directly, without the compromise of mass and momentum conservation, or by removing the cause of the high density gradients. These modifications are fully described in Poyurs [42].

Our version of the Lattice Boltzmann Method was tested by verifying that it correctly simulated Poiseuille flow, that the pressure in a bubble of non-wetting phase follow Laplace's law, and that two phases separate as expected when introduced in a mixed state. Description of these verification calculations can be found in Poyurs [42].

## 3.4 Analysis of Capillary Sealing using LBM

To analyze capillary sealing we simulate multiphase flow in an axially symmetric tube as shown in Figure 3.5. The tube has 160 nodes in the z direction and is 18 nodes in diameter at either end, narrowing to 8 nodes in diameter in the center. This narrowing is as smooth as possible given the coarseness of the grid. The square 20 x 20 x 160 grid is filled with solid nodes so that an annular construction is defined.

We initially placed a mixture of 50% wetting and 50% non-wetting fluid beneath the pore at locations $40 \leq z \leq 60$, and wetting fluid everywhere else, so that the final non-wetting saturation, in the total system, was 10%. We allowed the system to come to equilibrium for 500 iterations, with no applied pressured gradient and periodic boundary conditions. During this time, the wetting and non-wetting fluid separated in the lower part of the grid, forming a single non-wetting bubble surrounded by wetting fluid, as illustrated in Figure 3.6. At 500 iterations we applied the pressure boundary condition in which the wetting fluid mass was specified at each node on either end plane, and removed the periodic boundary conditions for the wetting fluid only.

Material and fluid parameters were assigned as indicated in Table 3.1. We used g = -0.7 with $g_{ww} = 0.05$ and $g_{nn} = 0$. The two fluids in the system are named "wetting" and "non-wetting" after their affinity to wet the solid boundary. We found that in conjunction with the non-zero self attraction of the wetting fluid, e.g., $g_{ww} = 0.05$, the

most distinct wetting behavior was obtained with $g_{sw} = 1$ and $g_{sn} = -10$.

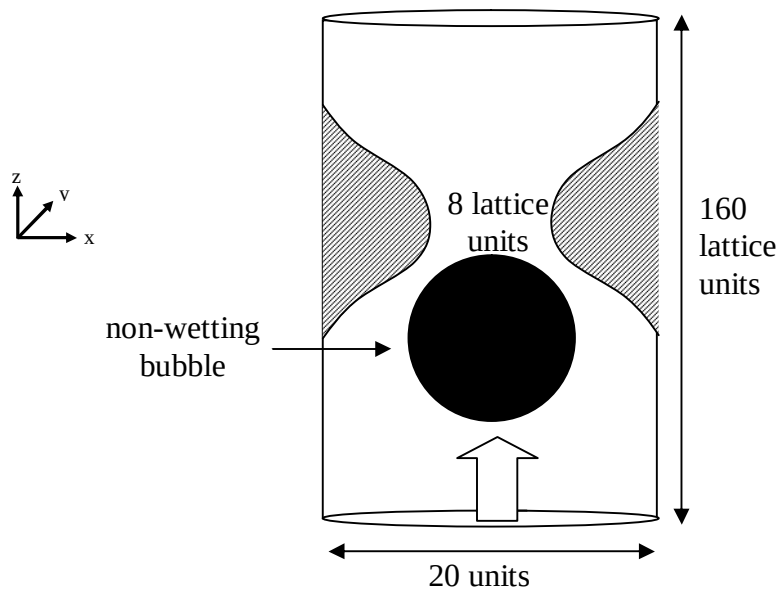


Figure 3.5: Numerical setup for the single pore simulations.

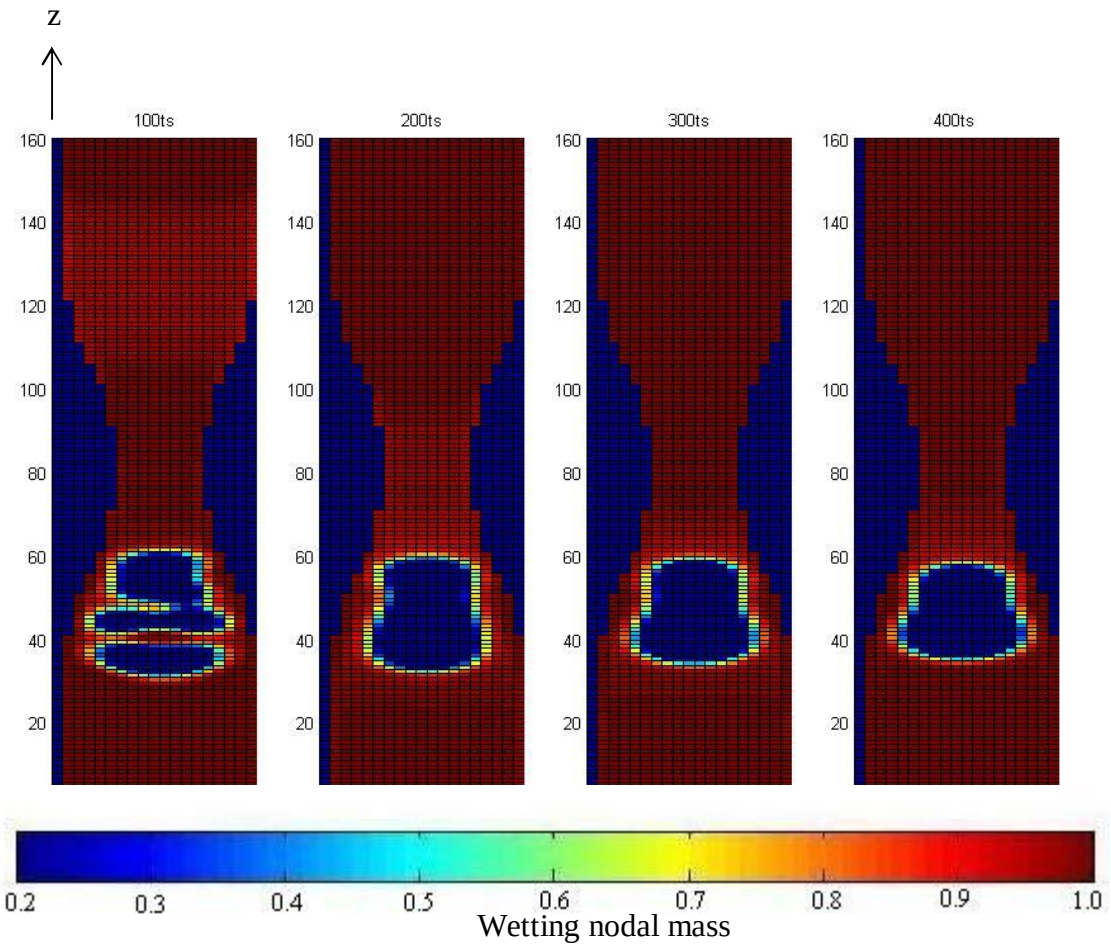


Figure 3.6: The capillary seal experiment is initialized with a mixture of both the wetting and non-wetting phases placed between $40 \leq z < 60$. Wetting fluid is placed everywhere else. A non-wetting bubble forms by 400 iterations.

Table 3.1. Parameters used in the LBM simulations

| | | |
|---|---|---|
| $L_x$ | Number nodes in x direction | $18 \rightarrow 8$ |
| $L_y$ | Number nodes in x direction | $18 \rightarrow 8$ |
| $L_z$ | Number nodes in x direction | 160 |
| $\tau$ | Relaxation parameter | 1 |
| $g_{nn}$ | Non-wetting fluid self attraction | 0 |
| $g_{ww}$ | Wetting fluid self attraction | 0.05 |
| $g_{wn}=g_{nw}$ | fluid repulsion from each other | -0.7 |
| $g_{sw}$ | Virtual wetting mass on solid node | 1 |
| $g_{sn}$ | Virtual wetting mass on solid node | -10 |
| $P_w^{top}$ | Average number of wetting particles specified on the top (z=160) boundary to fix pressure. | 0.09 |
| $P_w^{bottom}$ | Average number of wetting particles specified on the bottom (z=0) boundary to fix pressure. | 0.095 – 1 |
| $\rho_w^{initial}\big\|_{0\le z<60}$ | Density of wetting phase initially assigned to $0 \le z < 40$ | 0.1 |
| $\rho_n^{initial}\big\|_{0\le z<60}$ | Density of non-wetting phase initially assigned to $0 \le z < 40$ | 0 |
| $\rho_w^{initial}\big\|_{40\le z<60}$ | Density of wetting phase initially assigned to $40 \le z < 60$ | 0.1 |
| $\rho_n^{initial}\big\|_{40\le z<60}$ | Density of non-wetting phase initially assigned to $40 \le z < 60$ | 0.1 |
| $\rho_w^{initial}\big\|_{60\le z<160}$ | Density of wetting phase initially assigned to $60 \le z < 160$ | 0.1 |
| $\rho_n^{initial}\big\|_{60\le z<160}$ | Density of non-wetting phase initially assigned to $60 \le z < 160$ | 0 |
| $N_w$ | Number of nodes wetting fluid is initially applied to (same as the total number of nodes) | 29820 |
| $N_n$ | Number of nodes non-wetting fluid is initially applied to. | 3350 |

## 3.5 Results

### A. Multiphase flow through a constriction

In the first set of experiments, we examined the conditions under which the non-wetting phase moves through or is blocked by a constriction. To do this we set up the experiment as described generally above, with an initial Sn = 10%, calculated using Eq. 31.2 and the experimental parameters from Table 3.1.

We allow the mixture of fluids to segregate and a non-wetting bubble form for the first 500 time steps of the simulation. To simulate non-blocked flow, at 500 time steps, we set the wetting fluid nodal masses on the inlet and outlet to be $\rho_{inlet} = 0.16$ and $\rho_{outlet} = 0.144$. Using Eq.3.5 with D = 3 and c=1, this translates to a system pressure drop, $\Delta P = (0.16 - 0.144)/3 = 5.33 \times 10^{-3}$ lattice pressure units.

We calculated $\Delta P_c$ using Eq. 3.1, where σ was estimated by running a series of experiments to replicate Laplace law; see Poyurs [42]. From the code parameters shown in Table 3.1, for the parameters of this experiment, σ = 0.0124, $r_{fine} = 4$, $r_{coarse} = 9$, and so $\Delta P_c = 3.4 \times 10^{-3}$ lattice pressure units. We also estimated $\Delta P_c$ from a running a series of capillary sealing experiments where the $\rho_{inlet}$ was increased incrementally. We found that for $\rho_{outlet} = 0.144$ the non-wetting bubble was prevented from going through the pore for $\rho_{inlet} = 0.1536$ but passed through the pore for $\rho_{inlet} = 0.1552$. Thus $3.2 \times 10^{-3} < \Delta P_c <$ and $3.7 \times 10^{-3}$, which agrees with our analytical estimate of $3.4 \times 10^{-3}$ lattice pressure units.

We expect that since the applied pressure difference ( $\Delta P = 5.33 \times 10^{-3}$), is greater than the capillary pressure, $\Delta P_c$, the non-wetting phase will break through the constriction in this simulation. This happened between 7,500 and 12,500 time steps as shown in Figure 3.7.

To simulate blocked flow, we repeated the above experiment setting a prescribed $\rho_{inlet} = 0.152$ and $\rho_{outlet} = 0.144$ from 500 time steps onwards, so that the

system pressure drop, $\Delta P$ = 2.67 x $10^{-3}$ lattice pressure units, was less than $\Delta P_c$. We ran the simulation for 200,000 time steps. Once the non-wetting bubble became lodged in the pore at around 40,000 time steps, no further motion of the non-wetting bubble is observed for the full 200,000 time steps. This is shown in Figures 3.9 and 3.10. The time-average tube-parallel momentum of the wetting phase particles is zero. We discuss this at some length in the discussion section below.

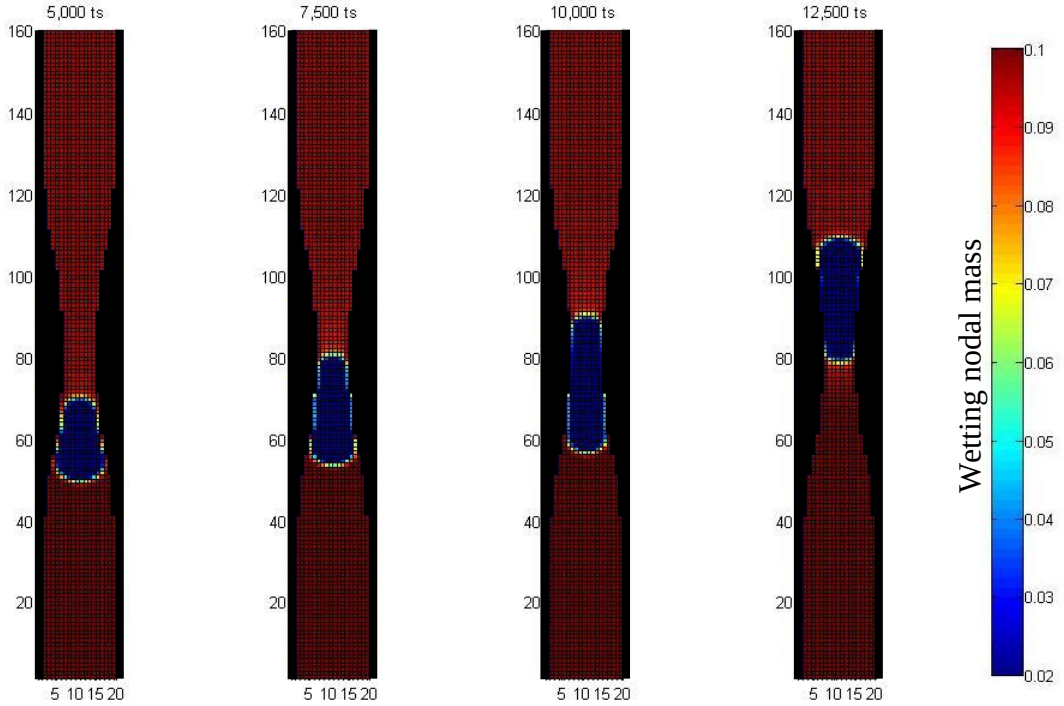


Figure 3.7: Snap shots of the central cross section through the tube, showing the nodal wetting fluid mass. The pressure drop across the tube, ΔP, was set at 5.33 x $10^{-3}$ lattice pressure units, and the capillary entry pressure, $\Delta P_c$ = 3.4 x $10^{-3}$ lattice pressure

units, so flow of the gas bubble through the constriction is expected and this figure shows it occurs.

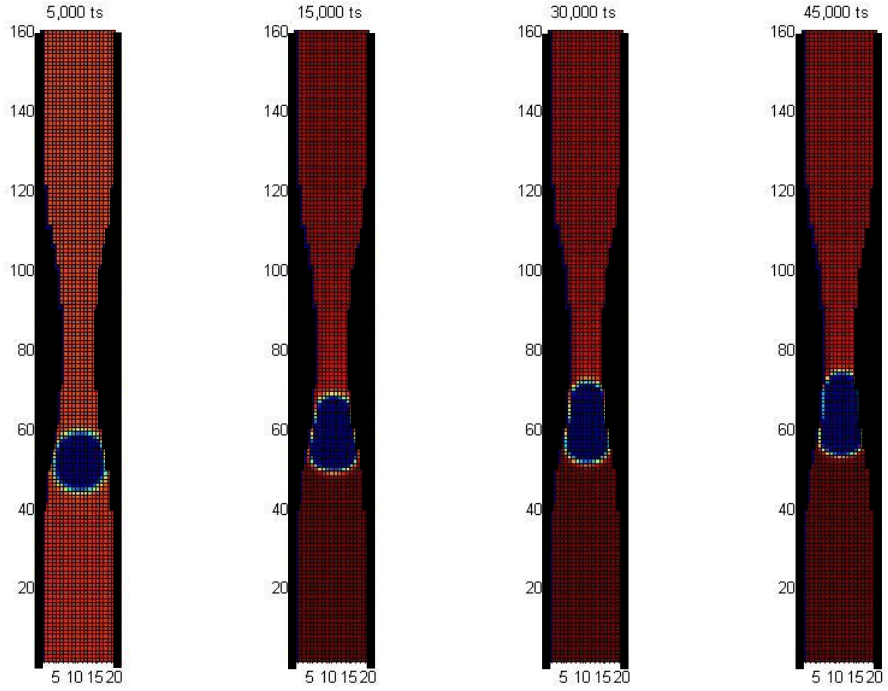


Figure 3.8: Snap shots of the central cross section through the tube, showing the nodal wetting fluid mass. For 5,000 time steps to 45,000 time steps. Note that the non-wetting bubble is prevented from moving from about 40,000 time steps onwards. The wetting fluid densities distributions for 50,000 time steps until the end of the simulation at 200,000 time steps are shown in Figure 3.9. The pressure drop across the tube, $\Delta P$, was set at 2.67 x $10^{-3}$ lattice pressure units, and the capillary entry pressure, $\Delta P_c$ = 3.4e$^{-3}$ lattice pressure units.

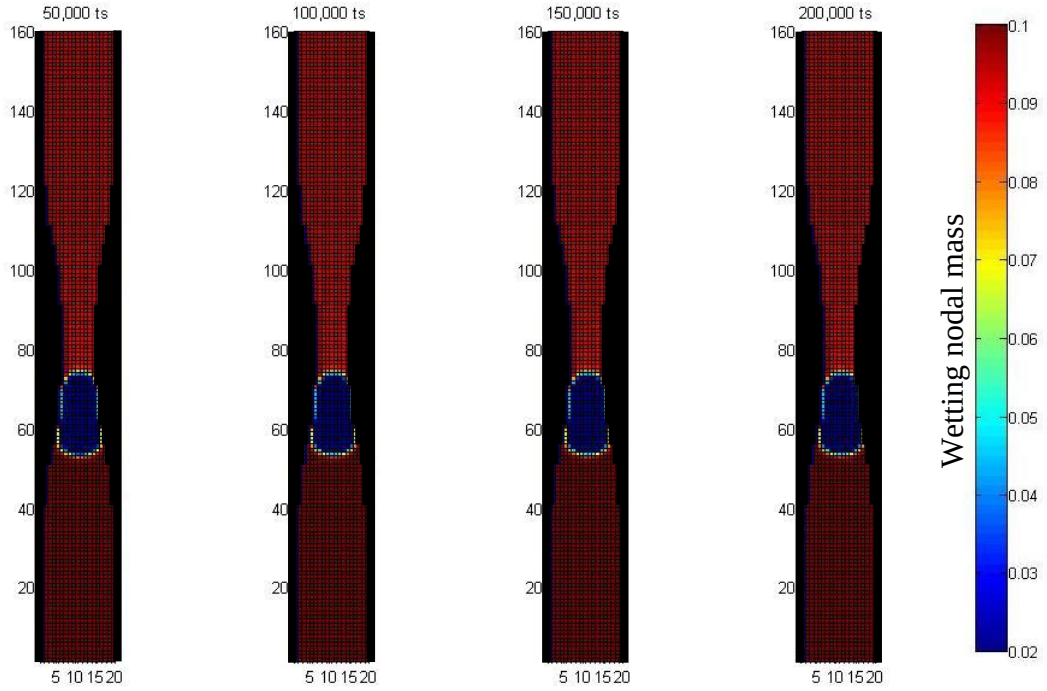


Figure 3.9: Snap shots of the central cross section through the tube, showing the nodal wetting fluid mass for 50,000 time steps through to the end of the simulation at 200,000 time steps. From Figure 3.9 in conjunction with this figure, it can be seen that the non-wetting bubble is prevented from moving from about 40,000 time steps onwards. The pressure drop across the tube, $\Delta P$, was set at $2.67 \times 10^{-3}$ lattice pressure units, and the capillary entry pressure, $\Delta P_c$ was $3.4 \times 10^{-3}$ lattice pressure units, so flow of the gas bubble through the constriction is not expected and this figure shows it does not occur.

B. Multiple pore constrictions

To investigate if the capillary pressure drop was cumulative over multiple blocked pores, we reproduced the blocked flow experimental set-up as described above, but with three pores in series. The grid set up is illustrated in Figure 3.11. As with the single pore experiment, a mixture of non-wetting and wetting fluid was placed immediately upstream of each pore, with only wetting fluid elsewhere, so that the saturation of the non-wetting mixture was 10% within each identical set-up pore unit. The mixtures were allowed to segregate under no external forces and with cyclic boundary conditions for 500 iterations. As with the single pore experiments, the non-wetting bubble appeared to have formed and be in equilibrium by 400 time steps. At 500 iterations, we switched the wetting boundary conditions to a fixed pressure inlet and outlet, with $\rho_{inlet} = 0.168$ and $\rho_{outlet} = 0.144$, so that the total system pressure drop, $\Delta P = 8 \times 10^{-3}$ lattice pressure units; three times that of the blocked flow single pore experiment and more than double $\Delta P_c$ for a single pore, but less than the cumulative entry pressure of three pores. As with the single blocked pore experiment, we then ran the simulation for 200,000 time steps. On a 1.4 GB PC, the simulation took ~ 5 days. Figure 3.14 shows that with a pressure drop across the whole system of $3\Delta P_c > \Delta P > \Delta P_c$, all three non-wetting bubbles are blocked behind their respective pores. This three pore experiment shows that the capillary pressure drop across each pore is indeed cumulative, as is shown in Shosa's experiments [19]. The three-pore experiment also indicates that the capillary pressure blocks the motion of the wetting as well as the non-wetting fluids, just as is suggested in Shosa's experiments [19]. As with the single constriction, the time-average tube-parallel momentum of the wetting phase particles is zero. We also discuss this in the discussion section below.

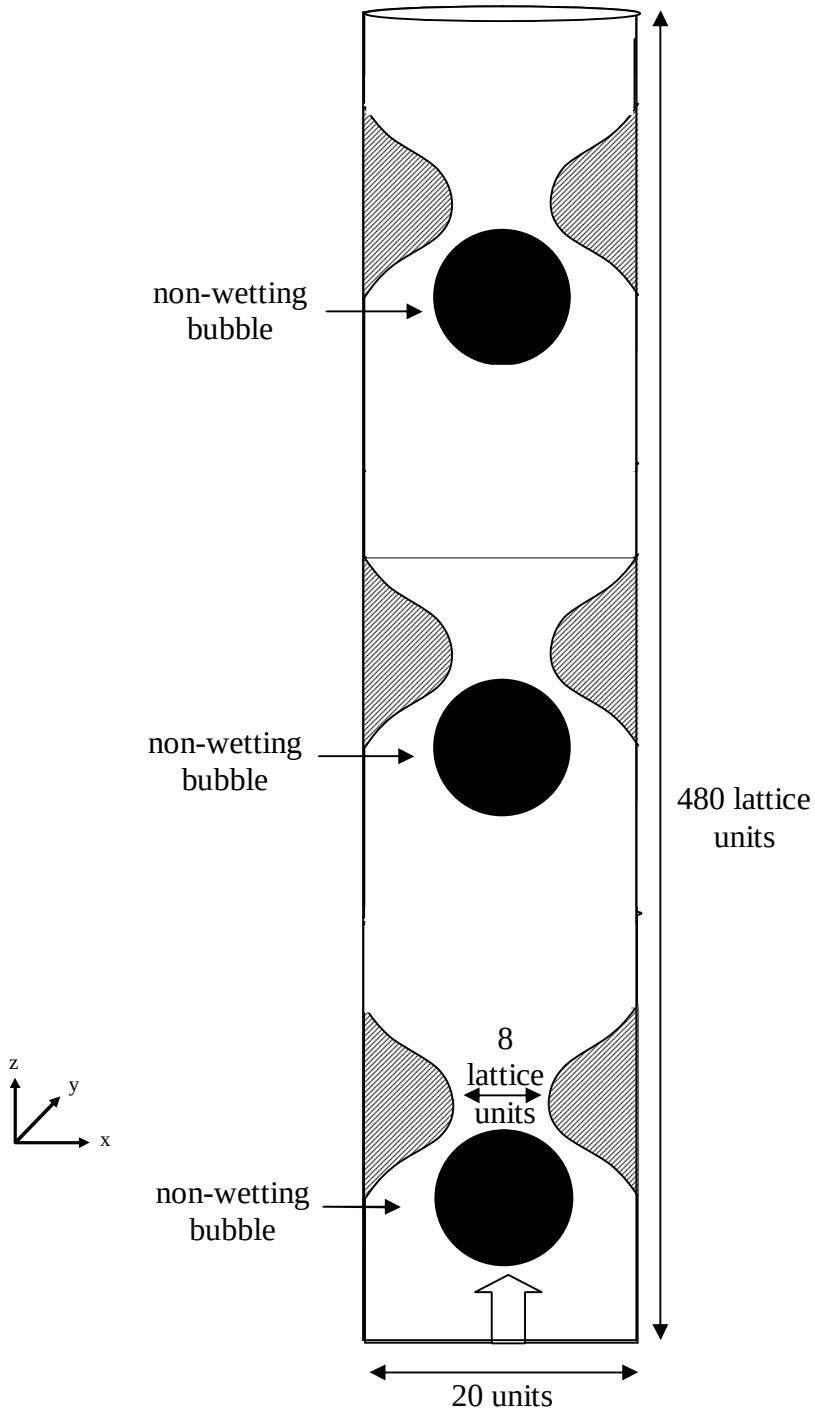


Figure 3.10: Numerical setup for three pores in series

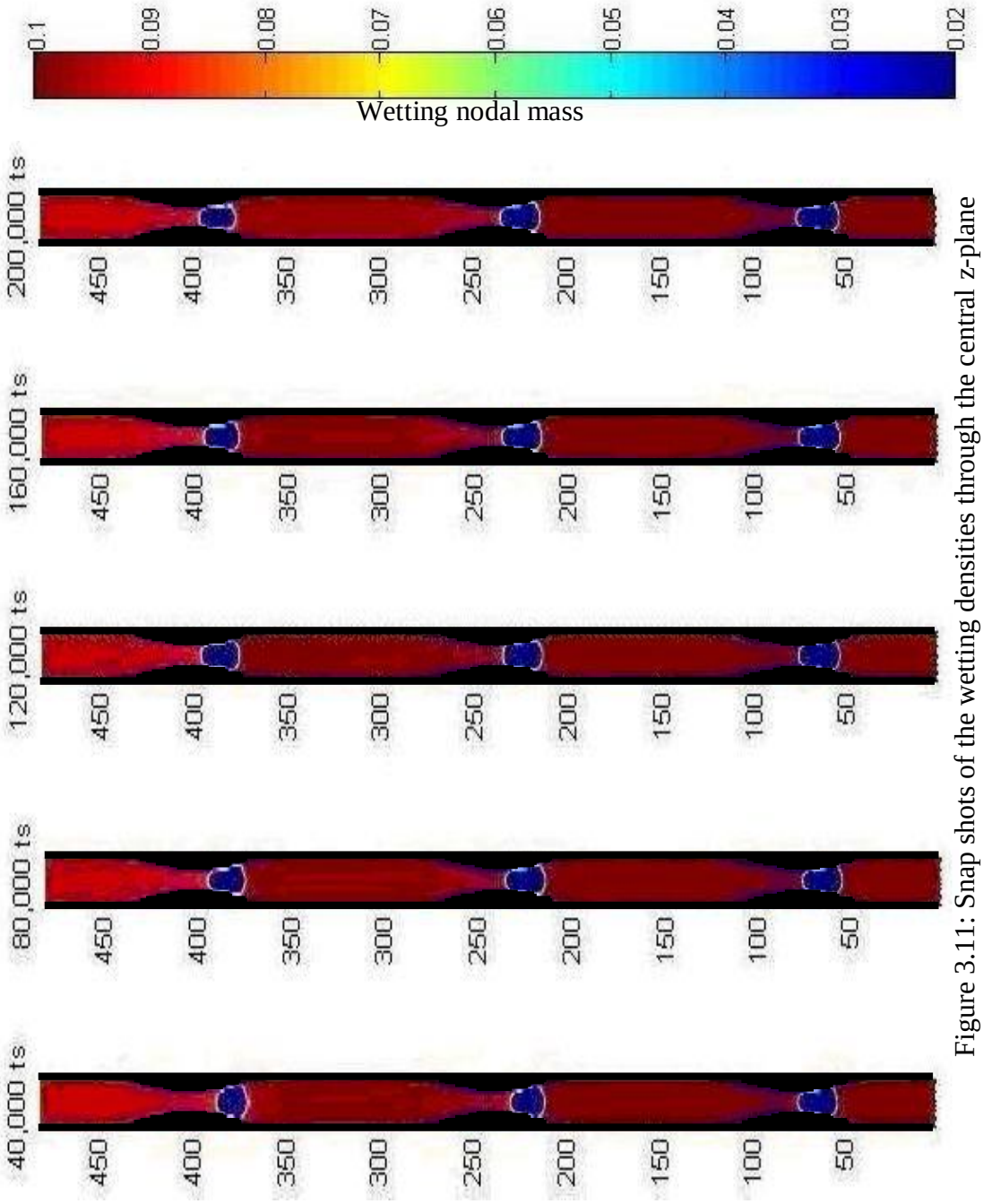


Figure 3.11: Snap shots of the wetting densities through the central z-plane

C. Seal healing

A critical aspect of capillary seals is their ability to re-heal. Here we use the LBM to investigate this phenomenon. We repeated the non-blocked simulation, as described in section A, with fixed wetting fluid pressure boundary conditions applied from 500 time steps onwards, so that $\rho_{inlet} = 0.16$ and $\rho_{outlet} = 0.144$, which translates to a system pressure drop, $\Delta P = 5.3 \times 10^{-3}$ lattice pressure units. At 5,000 time steps we reduce the inlet pressure so that $\rho_{inlet} = 0.152$ and $\Delta P = 2.67 \times 10^{-3}$ lattice pressure units; the parameters used in the blocked pore experiment. We observed the non-wetting bubble start to break through the pore and then at about 6,000 time steps (once the reduced pressure has had time to be transmitted to the bubble) we observed that the non-wetting bubble retreats back through the pore, as illustrated in Figure 3.12. From this point to the end of the simulation, the non-wetting bubble remains stuck upstream of the pore, as illustrated in Figure 3.13. The seal healing experiment clearly showed the ability of the capillary seals to re-from after break-through.

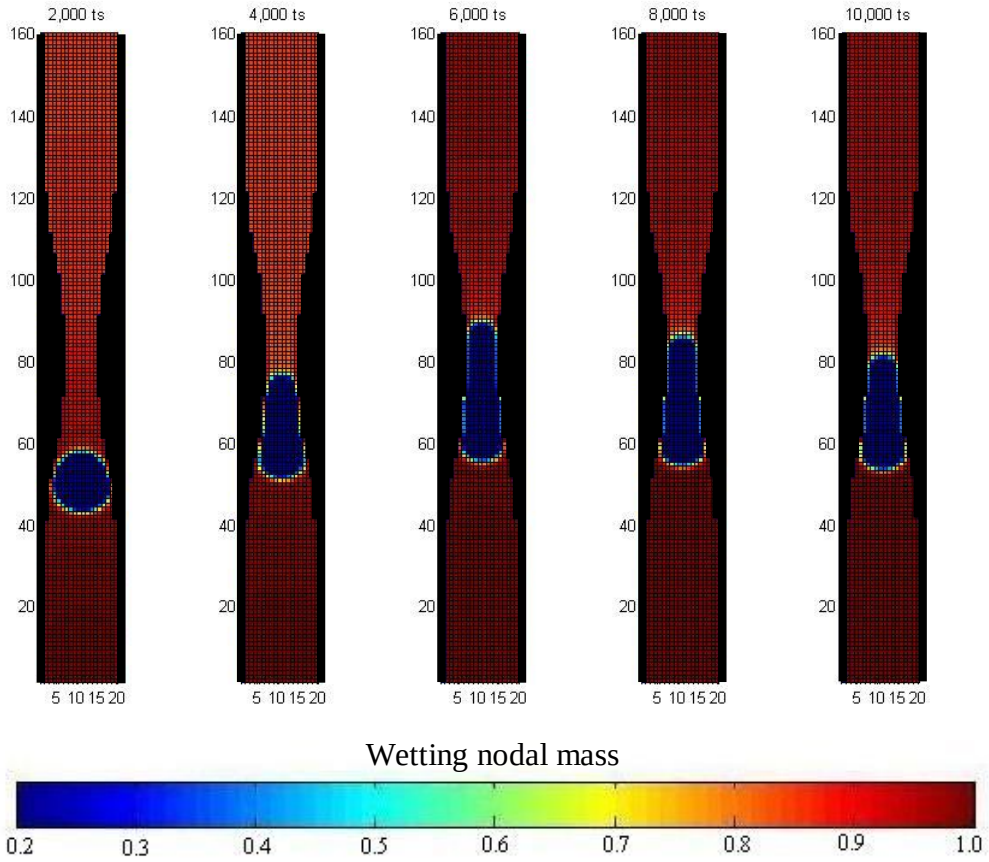


Figure 3.12: Snap shots of the wetting density distributions through the z-center plane for the first 10,000 time steps. $\Delta P$ across the system is $>\Delta Pc$, but is reduced to $<\Delta Pc$ at the 5,000 time step. The bubble begins to retreat when the new $\Delta P$ reaches the center of the tube at about 6,000 time steps.

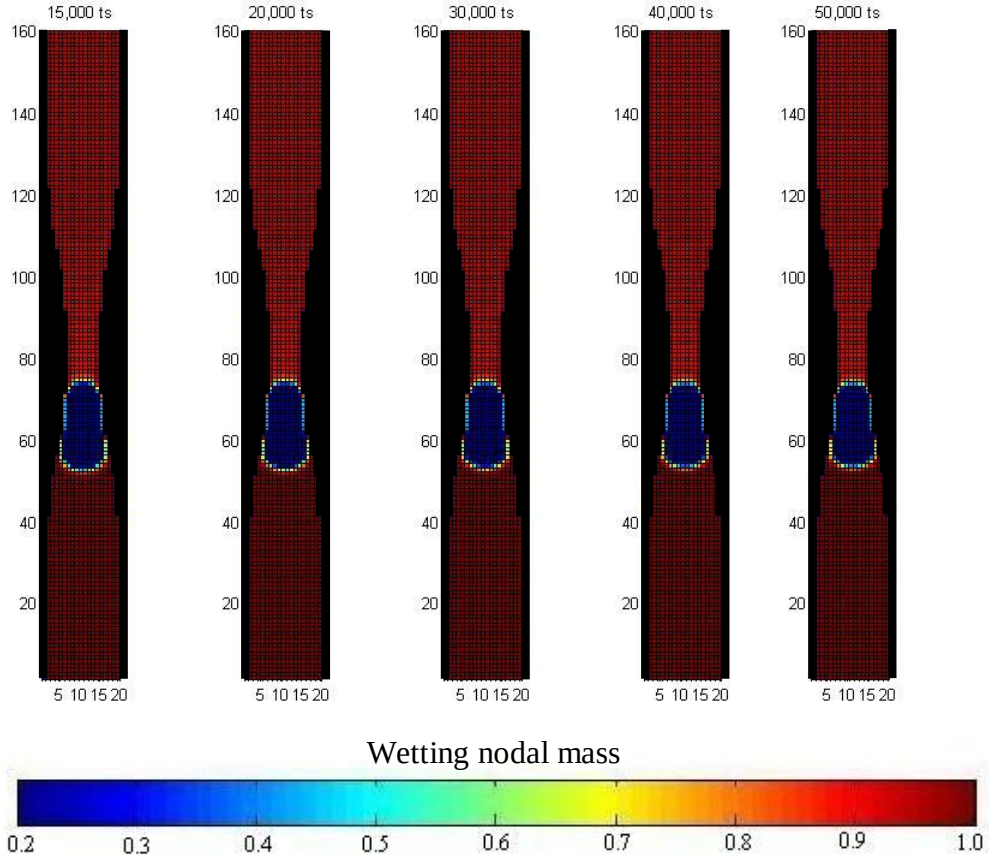


Figure 3.13: Snap shots of the wetting density distributions through the z-center plane from 15,000 time steps until the end of the simulation at 50,000 time steps. The bubble remains stuck over this time step.

D. Critical abundance of the non-wetting phase

We repeated the blocked pore experiment as described in section A, except that the initial non-wetting particle density placed at each node was varied. The non-wetting fluid saturation, $S_n$ is now defined as:

$$S_n = \frac{M\rho_n N_n}{M\rho_n N_n + \rho_w N_w} \qquad \ldots(3.13)$$

We varied the factor M such that the non-wetting fluid nodal density was = $0.7\,\rho_n$, $0.8\,\rho_n$ and $0.9\,\rho_n$. Using the values of $N_n$ and $N_w$ from Table 3.1, it may be seen that we investigated non-wetting fluid saturations of 7%, 8% and 9%. Again, at 500 time steps, after the two fluids separated, we replaced the cyclic boundary conditions on the wetting fluid with a fixed pressure inlet and outlet, so that $\Delta P = 2.67 \times 10^{-3}$ lattice pressure units, the same as in the blocked flow simulation. We found that with non-wetting fluid saturations of 7% and 8%, the non-wetting bubble passed through the pore, whereas with 9% saturation, the non-wetting bubble was prevented from passing through the pore. Therefore, for our simulation set-up, the critical non-wetting saturation is 8%. The results are illustrated in Figure 3.14 through Figure 3.16.

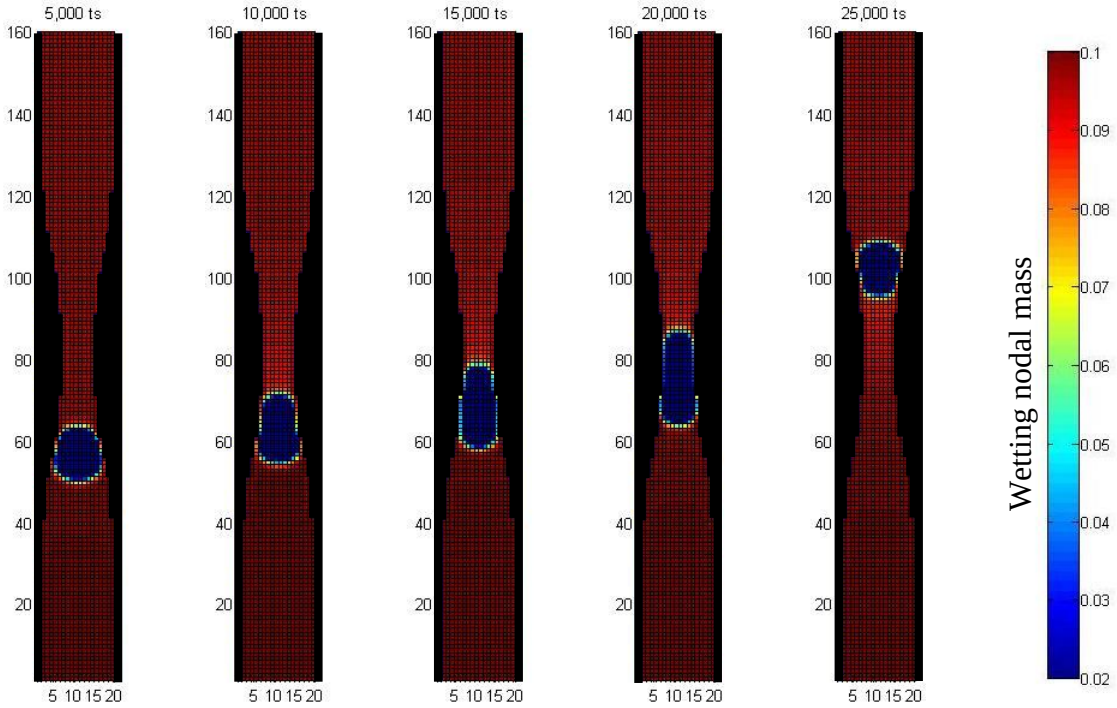


Figure 3.14: Snap shots of the wetting density distribution for the simulation with a non-wetting saturation of 7%. $\Delta P < \Delta Pc$

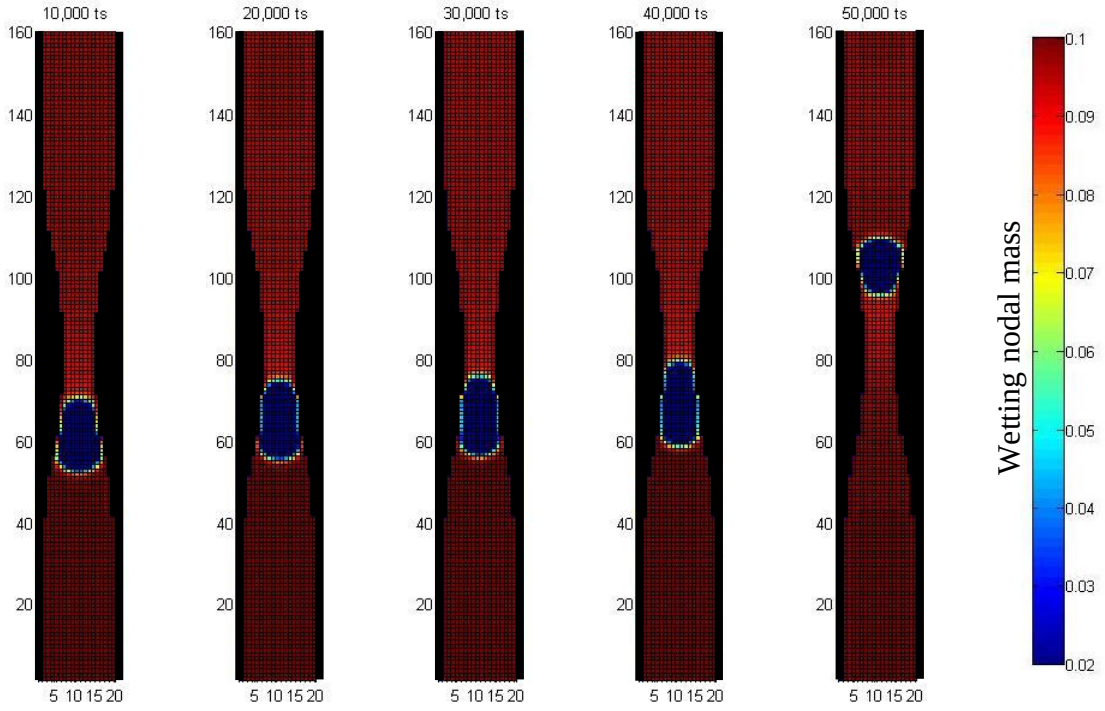


Figure 3.15: Snap shots of the wetting density distribution for the simulation with a non-wetting saturation of 8%. $\Delta P < \Delta Pc$

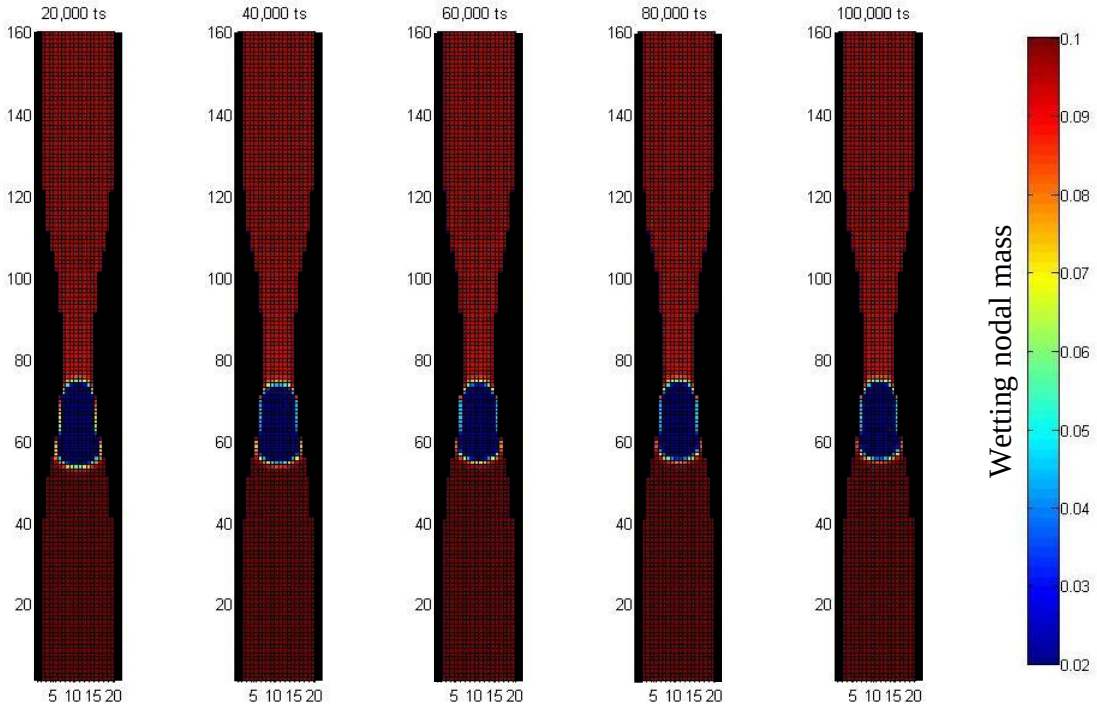


Figure 3.16: Snap shots of the wetting density distribution for the simulation with a non-wetting saturation of 9%. $\Delta P < \Delta Pc$

## 3.6 Discussion

### A. Blocked and unblocked flow of the non-wetting fluid

Whilst the motion of the non-wetting fluid was obviously prevented for the duration of the blocked flow simulation, some further probing of the results is required to determine if there is any leakage of the wetting fluid through the system. In the following sections, we take a more detailed at the z-momentum (flow parallel to the tube walls) distributions in both the unblocked and blocked-flow cases.

The wetting density distributions of the unblocked and blocked flow simulations in Figures 3.7 through 3.9 clearly show the non-wetting bubble going through the pore for $\Delta P > \Delta P_c$ and remaining trapped behind the pore for $\Delta P < \Delta P_c$. In Figure 3.17, the z-momentum distribution for the unblocked simulation is positive through the system, more so through the pore. This is to be expected from simple conservation of mass. The flow of the wetting fluid in the constricted part of the tube must be greater than in the non-constricted part. Since the cross sectional area of the tube reduces by a factor of 0.2 within the constriction, we expect that the velocity to increase by a factor of 5. We find this to be the case.

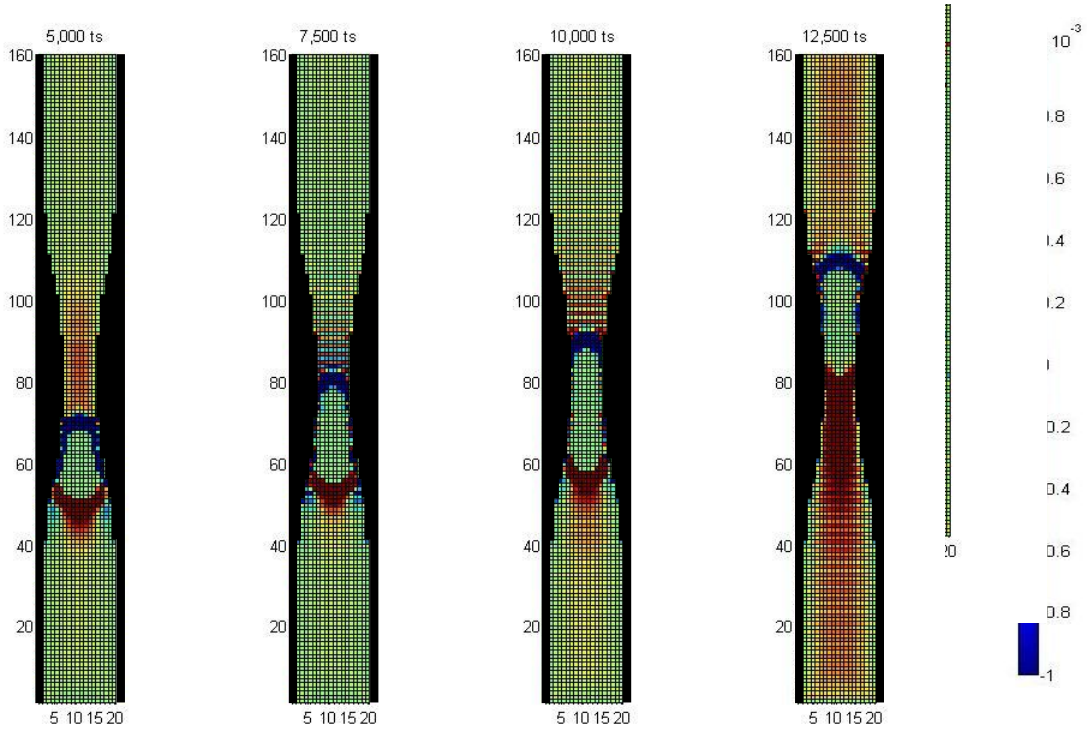


Figure 3.17: Snap shots of the central cross section through the tube, showing the nodal wetting fluid z-momentum for the numerical experiment shown in Figure 3.7.

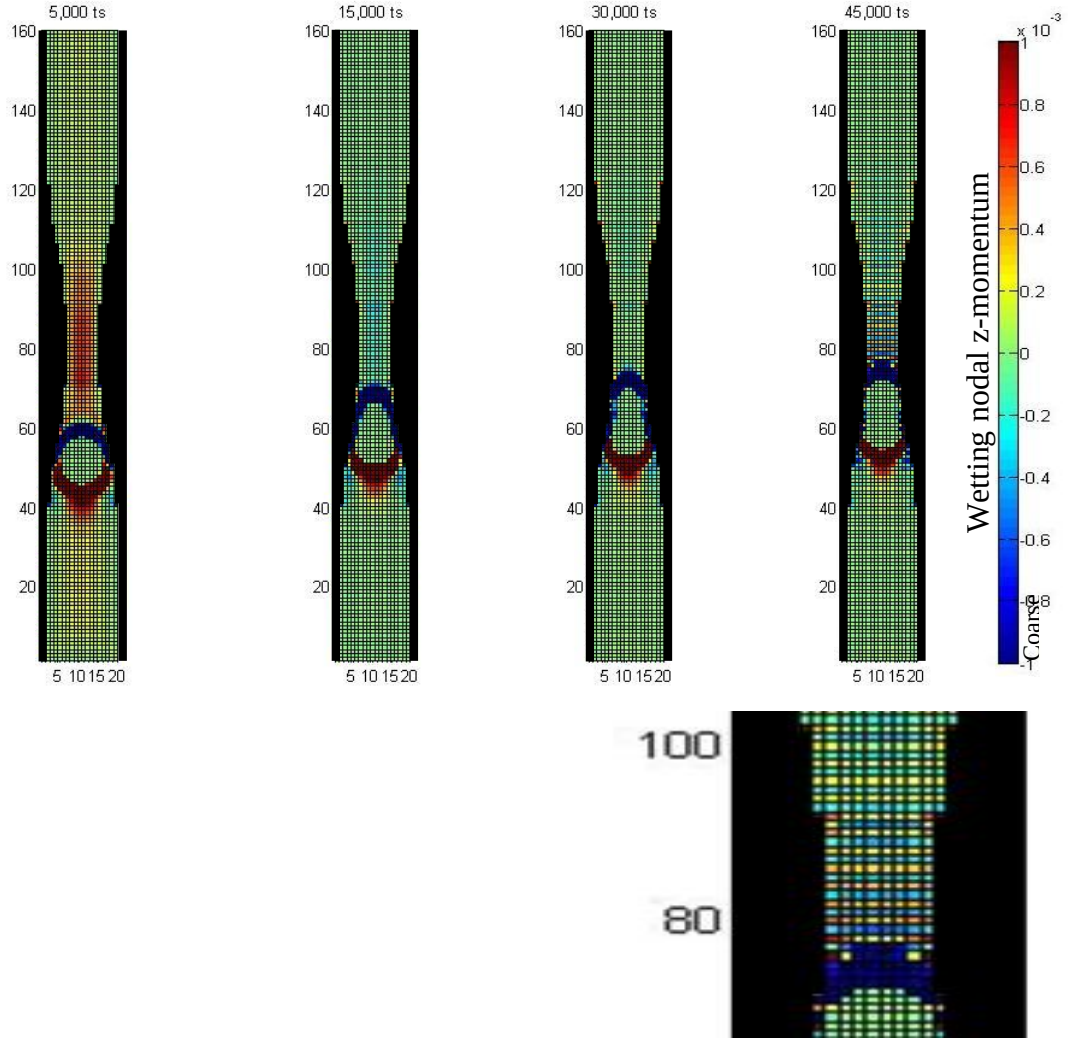


Figure 3.18: Snap shots of the central cross section through the tube, showing the nodal wetting fluid z-momentum for the numerical experiment in Figure 3.8. The blow up of the 45,000$^{th}$ iteration shows the z-momentum banding.

As shown in Figure 3.18, the z-momentum wetting fluid distributions for the blocked flow at 5,000 time steps shows a positive z-momentum. The blocked flow is shown in Figure 3.8 and 3.9. In this case the pressure drop across the tube is less than the capillary entry pressure, the pressure needed for the non-wetting fluid to pass through the constriction, but at the 5000$^{th}$ timestep the bubble is still being pushed into the pore. At the 15,000$^{th}$ iteration the bubble has just stalled, and the z-momentum of the wetting fluid downstream of the bubble is actually negative. By the 30,000$^{th}$ iteration the z-momentum downstream of the bubble is zero. At the 45,000$^{th}$ time step the z-momentum downstream of the trapped bubble is, on average, still zero but has become banded.

Within the z-momentum plots two other interesting phenomena may also be seen; regions of strong z-momentum on the ends of the non-wetting bubble, and isolated nodes located on the vertical tube boundary, which contain much greater z-momentum then their neighboring nodes. Such nodes are illustrated in Figure 3.19 below. The regions of strong z-momentum capping the upstream and downstream edges of the non-wetting bubble can be clearly seen as the blue cap and red bottom on the bubble in the z-momentum plot in Figure 3.16, for example. The capping indicates a strong flow of the wetting towards the non-wetting bubble. This is an artifact of the fact that we examine the z-momentum just after the particle motions have been redistributed and before the system has adjusted to the new particle motions. The caps are a numerical artifact that do not affect the momentum distributions obtained away from interfacial regions. Similarly, hot spots appear in the corner nodes for the wetting density distributions and momentum distributions, as shown for momentum in Figure 3.19. These hot spots are a numerical artifact caused when a fluid node neighbors more than one solid node. Both the momentum caps and the hot spots are

discussed at length in Poyurs [42]. Both numerical effects have been shown not to affect the general flow field and therefore can safely be ignored.

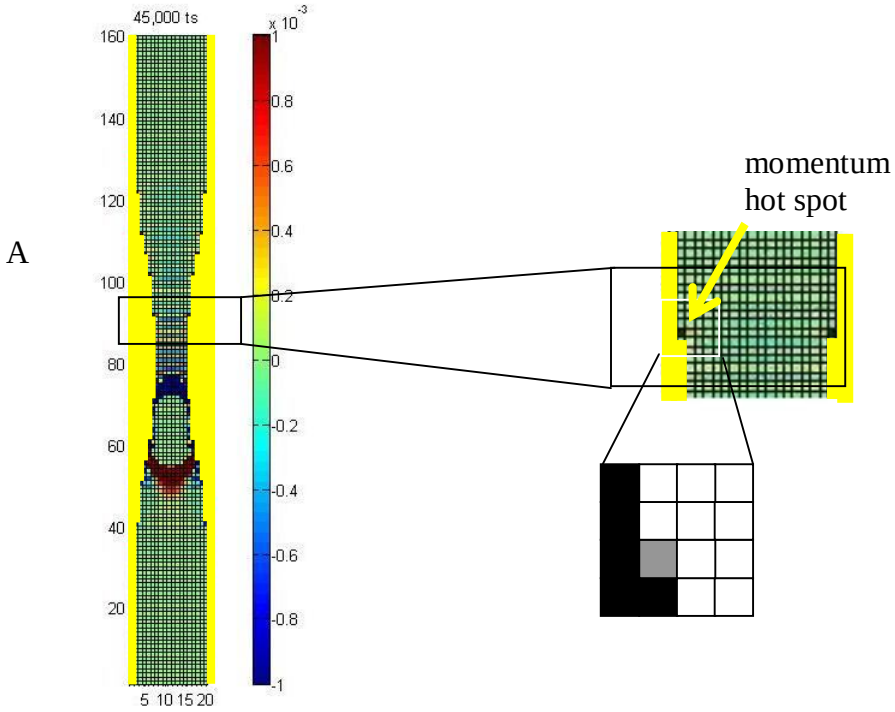


Figure 3.19: Illustration of a hot spot: corner nodes (the grey node in C) are located in the stepped boundary of the coarsely defined tube wall curvature (black nodes in C). The walls of the tube are highlighted in yellow to make the momentum hot spot more visible.

The reversal of flow at the 15,000$^{th}$ iteration may be explained by the fixed outlet pressure condition in conjunction with the reduction of wetting fluid flow as the non-wetting bubble becomes lodged into the pore.

Prior to the non-wetting bubble blocking the pore, wetting fluid is able to push through the pore. These wetting particle distributions have a positive z-momentum which is then translated downstream. As the non-wetting bubble becomes more lodged into the pore, the mass flux of wetting fluid through the pore reduces. At this point, due to the cessation of wetting mass flux, there is a wetting density deficiency immediately downstream of the pore with respect to the fixed wetting density at the outlet. This wetting density deficiency is the cause of the reverse pressure gradient. This reverse pressure gradient leads to the redistribution of wetting flow downstream of the blocked pore until the downstream region comes into equilibrium with the fixed wetting region density specified at the outlet.

Banding in the z-momentum distributions can be observed for the blocked flow experiment, from about 30,000 time steps onwards, and also in the non-blocked flow experiment at 10,000 time steps. The z-momentum banding for both experiments are blown up and shown in Figure 3.20 below. Poyurs [42] looked at the x y momentum plots for the blocked flow case and observed identical x, y momentum banding parallel to the x and y axis respectively, replicated in Figure 3.21. Given the no flow condition in the x and y directions, and given that the oscillation in the unblocked flow case exhibits a positive mean, Poyurs inferred that the oscillatory mean is the real value of the momentum. Furthermore, since the oscillation has a constant wavelength of 2 lattice lengths, Poyurs concluded that the oscillation is a numerical artifact, superimposed upon a momentum field of the mean value. For the blocked flow experiment, the wetting fluid therefore has zero momentum in these banded regions from ~ 30,000 time steps onwards.

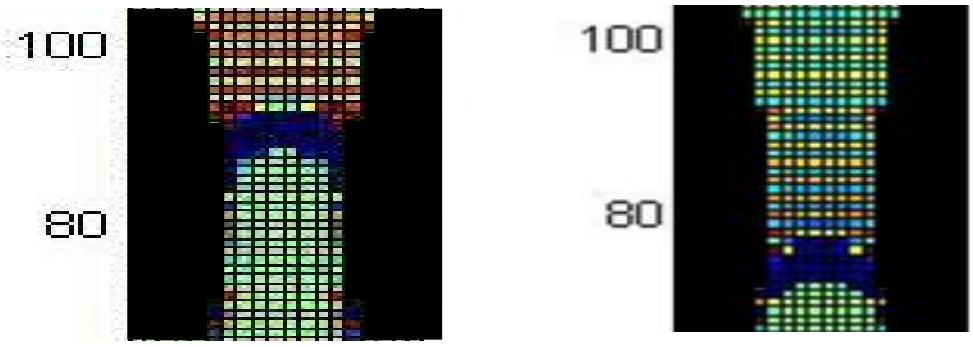


A B

Figure 3.20: Blow up of the z-momentum banding for the (A)_unblocked and (B) blocked experiments.

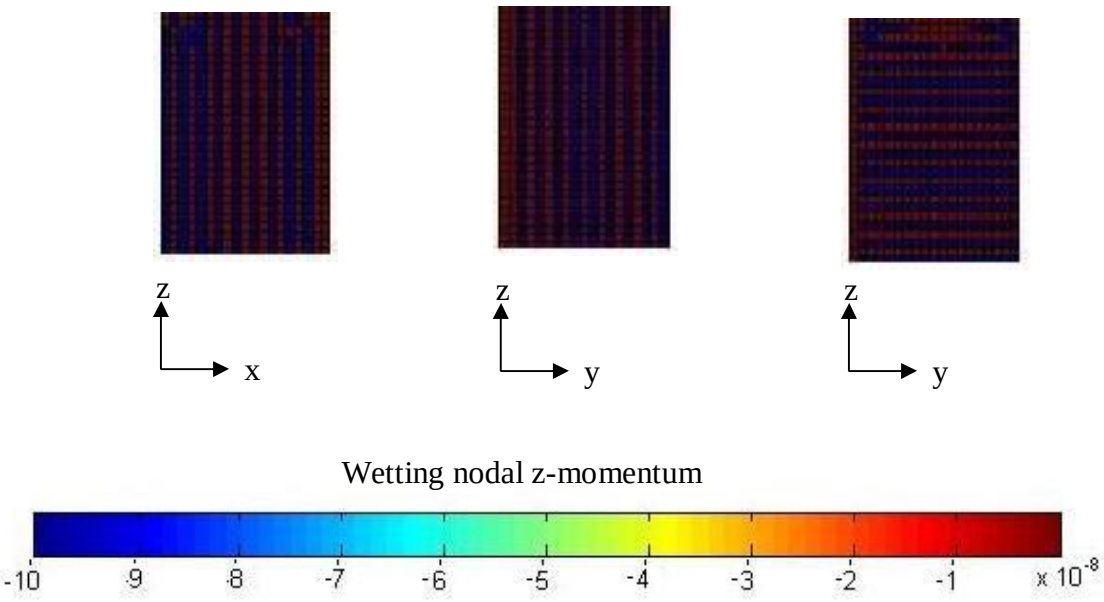


Figure 3.21: Blow up of the (A) x-momentum, (B) y-momentum and (C) z-momentum banding for the blocked experiment.

B. Multiple blocked pores

With three pores in series and with $\Delta P < \Sigma \Delta P_c$, we find that each pore is blocked. The capillary pressures drops across each pore constriction are additive, as indicated by the Shosa experiment [18]. Furthermore the wetting fluid z-momentum distributions indicate show all the same features as for a single blocked pore. Immediately following the plugging of a pore by the non-wetting bubble, the wetting fluid in the immediate downstream is sucked into the pore due to the presence of a reverse pressure gradient. Once this pressure has been equalized, the wetting fluid shows a banding of alternate positive and negative z-momentum averages to zero, indicating that all motion of the wetting fluid has ceased and that both phases are blocked.

It appears from Figure 3.11 that the blocked pores come into equilibrium sequentially downstream, one after another. It also appears that even after 200,000 time steps, the last downstream pore is not completely in equilibrium. At this time step there is still some wetting fluid back flow into the pore, indicating that the non-wetting bubble immediately upstream of the third pore has just plugged the third pore and that at 200,000 time steps, the wetting fluid pressure gradient has been reversed so that the wetting fluid flows back into the third pore. We expect that should the experiment have been carried out for longer, we would have seen the wetting fluid z-momentum revert to a banded pattern similar to that observed in the two upstream pores.

C. Seal healing

The seal healing experiment (Figure 3.12) clearly showed the ability of the capillary seals to re-form after break-through. After the non-wetting bubble was pushed all the way through the downstream exit of the finest part of the pore and $\Delta P$

was reduced so that $\Delta P < \Delta P_c$, the non-wetting bubble then retreated through the pore, and all further flow through the pore was blocked. Once the non-wetting bubble is stuck upstream of the pore, there is no motion of the wetting fluid downstream.

The actual characteristics of the retreat merit further discussion. The downstream interface retreats all the way to the upstream side of the finest pore. The finest part of the pore consists of a tube of diameter 8 lattice lengths and length 20 lattice lengths. Thus there is a substantial interval in the center of the tube constriction where the diameter of the tube is constant. Why does the interface retreat when the radius of curvature, and therefore the capillary pressure, is the same all throughout this portion of the finest pore? Once the downstream interface has settled, it seems that the upstream interface moves slightly into the bubble, why is this so?

This motion can be understood in terms of the pressures exerted on the bubble.

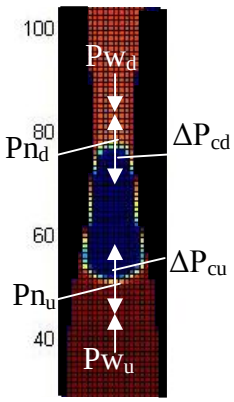


Figure 3.22: The pressures exerted on the bubble.

As shown in Figure 3.22, $Pw_u$, $Pn_u$, and $\Delta P_{cu}$ are the pressures in the wetting fluid, the non-wetting fluid, and the capillary pressure on the upstream interface of the non-wetting fluid, and $Pw_d$, $Pn_d$, and $\Delta P_{cd}$ are the same on the downstream interface.

The motion of the bubble can be thought of as balance of these pressures. At equilibrium, when the bubble is lodged and not moving:

$$Pw_u + \Delta P_{cu} - Pn_u = Pw_d + \Delta P_{cd} - Pn_d \,. \qquad \ldots(3.14)$$

But since $Pn_d = Pn_u$, we see that equilibrium requires that the pressure drop of the wetting fluid across the non-wetting bubble be balanced by the difference in the capillary pressures the downstream and upstream ends of the non-wetting bubble:

$$Pw_u - Pw_d = \Delta P_{cd} - \Delta P_{cu} \qquad \ldots(3.15)$$

If the non-wetting bubble is initially pushed into the smallest diameter interval of the tube constriction and $Pw_u$ then reduced, the bubble must move backward (upstream) until the tube radius at the downstream bubble surface is such that there is overall pressure balance. For most of this retreat the downstream end of the bubble is in the constriction and $\Delta P_{cu}$ is thus not changing. By conservation of mass the entire bubble must retreat until a force balance is re-established

D. Critical abundance of the non-wetting phase

The experiments show that there is a critical non-wetting saturation required for the pore to block the flow of the fluids. With the parameters used in our simulations, it appears that this critical saturation is ~8% (see Figures 3.14-3.16). Our experiments suggest that for the non-wetting bubble to lodge it must be large enough so that whilst the downstream end is inserted into the finest pore, its upstream end is in the largest part of the coarsest pore. Thus for a seal to form we need half the porosity of the bordering fine layer to be filled with non-wetting fluid. If we ask what

the saturation of the first layer of coarse pores must be to supply this amount of non-wetting fluid, we find the required saturation is $\varphi d_{fine}/2$ divided by $\varphi d_{coarse}$ or $d_{fine}/2d_{coarse}$, where $\varphi$ is the porosity of both layers (assumed to be the same) and d is the diameter of the fine or coarse layers depending on the subscript.

Using the values from our experiments, $d_{fine}$= 8 and $d_{coarse}$ = 18, this gives S=22%. This is very different from our estimate of non-wetting fluid saturation 8%. However, the 8% non-wetting fluid saturation was calculated using the total number of nodes into which non-wetting and wetting fluids are initially placed. If, for the wetting fluid, we use the number of nodes from half way along the coarser part of the tube through the middle of the pore, half way along the finer part of the pore, we find that this gives $N_w$ = 9770. Using this value in Eq. 3.12, we find that critical non-wetting saturation for blockage to occur is 21.5%, very close to our rough estimation.

## 3.7 Summary and Conclusion

The presence of abnormally pressure compartments in sedimentary basins that have in some cases persisted for hundreds of millions of years are well documented world-wide. We investigate here a possible capillary sealing mechanism in which a non-wetting bubble inserted into the pores of a fine-grained layer would prevent the motion of both the wetting and non-wetting phases through that layer. For this mechanism to contain the abnormal pressures observed, the capillary pressure drops at each interface must be additive over many coarse/fine interfaces, and if ruptured the capillary seals must be able to re-form. Demonstrating this by numerical simulations is the objective of this paper.

The Lattice Boltzmann Method was chosen for its ability to easily simulate multiple immiscible fluids and complex boundaries. The LBM simulations we report here show that the capillary forces are able to prevent flow of both phases through a

blocked pore, and that the resulting pressure drop across a single pore throat is indeed additive across many pore throats. LBM shows that the wetting fluid is imbibed back into the finest part of the pore from its downstream side, and that thereafter the flow of both fluids is zero. Both the wetting and non-wetting fluids are totally blocked. Furthermore the numerical simulations shows how the capillary seal re-heals after relaxation of overpressures high enough to push the non-wetting phase through the seal and cause seal failure. The numerical simulations suggest that the saturation of the fine pores must be sufficient for the non-wetting phase to extend into the coarse layer, a very minimal requirement for sealing. The numerical experiments we report thus confirm all important aspects of the capillary sealing hypothesis. In simulating total flow blockage we also were led to examine aspects of the LBM that could be of broader interest.

# REFERENCES


1. Shan, X. and H. Chen, *Lattice Boltzmann Model for Simulating Flows with Multiple Phases and Components*. Phys. Rev E, 1993. 47(3):p.1815-1820.

2. Powley, D.E., *Pressures and hydrogeology in petroleum basins.* Earth Science Reviews, 1990. 29(1-4): p. 215-226.

3. Bradley, J.S., *Abnormal Pressure Formation.* AAPG Bull., 1975. 59(6): p. 957-973.

4. Ortoleva, P., Z. Al-Shaieb, and J. Puckette, *Genesis and dynamics of basin compartments and seals.* Am. J. Sci., 1995. 295: p. 345-427.

5. Osborne, M.J. and R.E. Swarbrick, *Mechanisms for generating overpressure in sedimentary basins: A Reevaluation.* AAPG Bull., 1997. 81(6): p. 1023 - 1041.

6. Holm, G., How abnormal pressures affect hydrocarbon exploration. Oil and Gas J., 1998. 96(2): p. 79-84.

7. Bredehoeft, J.D. and B.B. Hanshaw, *On maintenance of anomalous fluid pressures. 1. Thick sedimentary sequences.* Geological Society of America Bulletin, 1968. 79(9): p. 1097-1106.

8. van Ruth, P., et al., *The origin of overpressure in 'old' sedimentary basins: an example from the Cooper Basin, Australia.* GeoFluids, 2003. 3(2): p. 125-131.

9. Powley, D. E., *Resume of Talk*, Gas Research Institute Deep Gas Sands Workshop, 1987, Chicago, July 30:p.30.

10. Hunt, J.M., *Generation and migration of Petroleum from Abnormally Pressured Fluid Compartments*, AAPG, 1990. 74(1):p.1-12.

11. Bradley, J.S and D. E. Powley, *Pressure Compartments in Sedimentary Basins: A Review*, in Basin Compartments and Seals, ed. 1994. Tulsa, Oklahoma, AAPG Memoir , 61:p.3-26.

12. Ortoleva, P.J., *Basin Compartments and Seals*, ed. 1994. Tulsa, Oklahoma, AAPG:p.477.

13. Surdam, *Seals, Traps and the Petroleum System*, ed. 1997, Tulsa Oklahoma, AAPG:p.317.

14. Law, B.E. et. al., *Abnormal Pressures in Hydrocarbon Environments*, ed. 1998. AAPG:p.264.

15. Mitchell, A. and D. Graules, *Overpressures in Petroleum Exploration*, ed. 1999. Bull. Centre Rech. Elf Explor. Prod., Pau:p.248.

16. Tigert, V. and Z. Al-Shaieb, *Pressure Seals: Their Diagenetic Banding Patterns.* Earth-Sci Revs., 1990. 29: p. 227-240.

17. Perrodon, A., *Dynamics of Oil Gas Accumulations*, ed. E. Aquitaine. 1983, Paris. 368.

18. Deming, D., *Factors necessary to define a pressure seal.* AAPG Bull., 1994. 78(6): p. 1005 - 1009.

19. Shosa, J., *Overpressure in sedimentary basins: Mechanisms and mineralogical implications*, in *Department of Earth and Atmostpheric Sciences*. 2000, Cornell University: Ithaca.

20. Cathles, L.M., *Capillary Seals as a Cause of Pressure Compartmentation in Sedimentary Basins*, 2001, GCSSEPM Foundation 21st Annual Research conference Petroleum Systems of Deep-Water Basins, Dec 2-5.

21. Meulbroek, *Hydrocarbon Phase Fractionation in Sedimentary Basins*, 1997. Geological Sciences, Ithaca, Cornell:p.345.

22. Al-Shaieb, Z. et. al., *Megacompartment Complex in the Anadarko Basin: A Completely Sealed Overpressured Phenomenon*, 1994. In Basin Compartments and Seals: AAPG Memoir, 66: p.55-68.

23. Al-Shaieb, Z. et. al., *Three Levels of Compartmentation within the Overpressured Interval of the Anadarko Basin*, 1994. In Basin Compartments and Seals: AAPG Memoir, 66: p.69-83.

24. Shosa, J.D. and L.M. Cathles. Experimental Investigation of Capillary Blockage of Two Phase Flow in Layered Porous Media. in GCSSEPM Foundation 21st Annual Research Conference: Petroleums Systems of deep-Water Basins. 2001.

25. Shan X. and H. Chen H., Simulation of Nonideal Gases and Liquid-Gas Fluid Transitions by the Lattice Boltzmann Equation. Phys. Rev E., 1994. 49: p. 2941-2948.

26. Swift M., W. R. Osborn, and J. M. Yeomans, *Lattice Boltzmann Simulation of Nonideal Fluids.* Phys. Rev. Lett., 1995. 75(5): p. 830-833.

27. Swift M., et al., *Lattice Boltzmann Simulation of Liquid Gas and Binary Fluid Systems.* Phys. Rev. E., 1996. 54(5): p. 5041-5052.

28. Gunstensen A. K., et al., *Lattice Boltzmann Model of Immiscible Fluids.* Phys. Rev. A, 1991. 43(8): p. 4320-4327.

29. Gunstensen A. K. and Rothman D., *Lattice-Boltzmann Studies of Immiscible Two –Fluid Flow Through Porous Media.* J. Geophys. Res., 1993. 98(B4): p. 6431-6441.

30. Appert C., S. Zaleski, Physical Review Letters, 1990, 64(1).

31. McNamara G., B. Alder, *Analysis of the Lattice Boltzmann Treatment of Hydrodynamics*, Physica A, 1993, 194: pp.218-228.

32. Benzi R., S. Succi, *Two-dimensional turbulence with the lattice Boltzmann equation*, 1990, J. Phys. A: Math. Gen,. 23(L1-L5).

33. Succi S.,*The Lattice Boltzmann Equation for Fluid Dynamics and Beyond*., 1st ed., 2001, Oxford: Oxford University Press.

34. Filippova O., et. al., *Multiscale Lattice Boltzmann Schemes with Turbulence Modeling,* Journal of Computational Physics, 2001, 170(2):pp. 812-829.

35. Benzi R., S. Succi, and M. Vergassoa, *The lattice Boltzmann equation- theory and applications.* Phys. Rep., 1992. 222(3): p. 145-197.

36. Martys N. S., H. Chen, *Simulation of Multicomponent Fluids in Complex Three-Dimensional Geometries by the Lattice Boltzmann Method*, Physical Review E, 1996, 53(1):pp.743.

37. Rothman D., J. Geophys. Res., 1990, 95:pp.8663.

38. Chen S. and G. Doolen, *Lattice Boltzmann Method for Fluid Flows.* Annu. Rev. Fluid Mech., 1998, 30: p. 329-364.

39. Alexander F. J., et. al., *Lattice Boltzmann model for Compressible Fluids*, Phys. Rev. A., 1991, 46(4): p.1967-1970.

40. Sofonea V., R. Sekerka, Viscosity of Finite Difference Boltzmann Models, Journal of Computational Physics, 2003, 184:pp.422-434.

41. Chen S., et al., *Lattice Boltzmann Model for Simulation of Magnetohydrodynamics.* Phys. Rev. Lett., 1991, 67: p. 3776-3779.

42. Poyurs, C., *Application of the Lattice Boltzmann Method to Understanding Capillary Seals in Sedimentary Basins and Dynamic Phase Interfaces*, in *Department of Earth and Atmospheric Sciences*. 2009, Cornell University: Ithaca.

43. Ladd, A.J.C. and Verberg R., *Lattice-Boltzmann Simulations of Particle-Fluid Suspensions*, J. Stat. Physics, 2001,104(516):pp.1191-1251.

44. Hazi G., et al., *Lattice Boltzmann Methods For Two Phase Flow Modeling.* Annuals of Nuclear Energy, 2002. 29: p. 1421-1453.

# Chapter 4. Dynamic Fluid Interface in a Hele Shaw Cell

## 4.1 Abstract

The Lattice Boltzmann Method (LBM) model of Shan and Chen [1] for immiscible fluids is used to simulate the dynamic fluid interface in a Hele-Shaw cell for a range of fluid velocities and surface tensions. We find that the Hoffman Tanner law captures the relationship between contact angel and flow velocity better than the empirically based law suggested by Weitz or the relationship derived from molecular kinetics suggested by Blake and Haynes. This justifies the widespread use of the Hoffman Tanner relationship to model the velocity dependant of the dynamic contact angle. We find how wettability, a factor not explicitly considered in any of these relationships, affects the velocity at which the curvature of the interface reverses and their coefficients multiplying the capillary number term. Our numerical experiments thus shed light on the wide variation of model constants found in the literature.

## 4.2 Introduction

The contact angle between a fluid-fluid interface and a solid boundary is known to change with the interfacial velocity. For example, as shown in Figure 4.1a, if there is no flow through the capillary tube, the interface between the wetting and non-wetting fluids is concave into the wetting fluid and the pressure in the non-wetting fluid, $P_n$, is greater than the pressure in the wetting fluid, $P_w$, by the amount needed to balance the capillary forces. In this case the meniscus meets the wall of the capillary at an angle $\theta_s$.

$$P_c = P_n - P_w = \frac{2\sigma\cos\theta_s}{r}, \qquad \ldots(4.1)$$

where r is the radius of the capillary tube, σ is the interfacial tension between the wetting and non-wetting fluids, $P_c$ is, by definition, the capillary pressure, and $\theta_s$ is the contact angle under static flow conditions. As the pressure drop across the capillary tube is increased above $P_c$, flow occurs through the tube and the curvature of the interface first flattens and then reverses as shown in Figures 4.1b and c. How the contact angle, θ, changes as the velocity of the interface, *u*, increases is important to theories of fingering instabilities [7, 8]. Dynamic contact angles in Hele Shaw cells have been the subject of much research, due to the similarity between the governing equations of fluid flow in Hele Shaw cells and in porous media. Good reviews can be found in Dussan [9], de Gennes [10], Kistler [11], Blake [12], and the comments in Schiaffino & Sonin [13]. See Appendix A for further discussion of fingering instabilities.

Several models of the relationship between interface velocity and contact angle have been proposed. Based on empirical observations, Hoffman [2] and Tanner [3] suggested that the contact angle depends on the capillary number, Ca [14, 15]:

$$\theta_d = A_{HT} Ca^{\frac{1}{3}} + \theta_s . \qquad \ldots(4.2)$$

This equation is known as the Hoffman-Tanner law. In it, $\theta_d$ is the dynamic contact angle, and $\theta_s$ is the static contact angle. The interface velocity is represented by the capillary number, Ca, which expresses the ratio of viscous and capillary forces.

$$Ca = \nu u / \sigma \qquad \ldots(4.3)$$

where $\nu$ is the dynamic viscosity, and $\sigma$ is interfacial tension between the wetting and non-wetting phases.

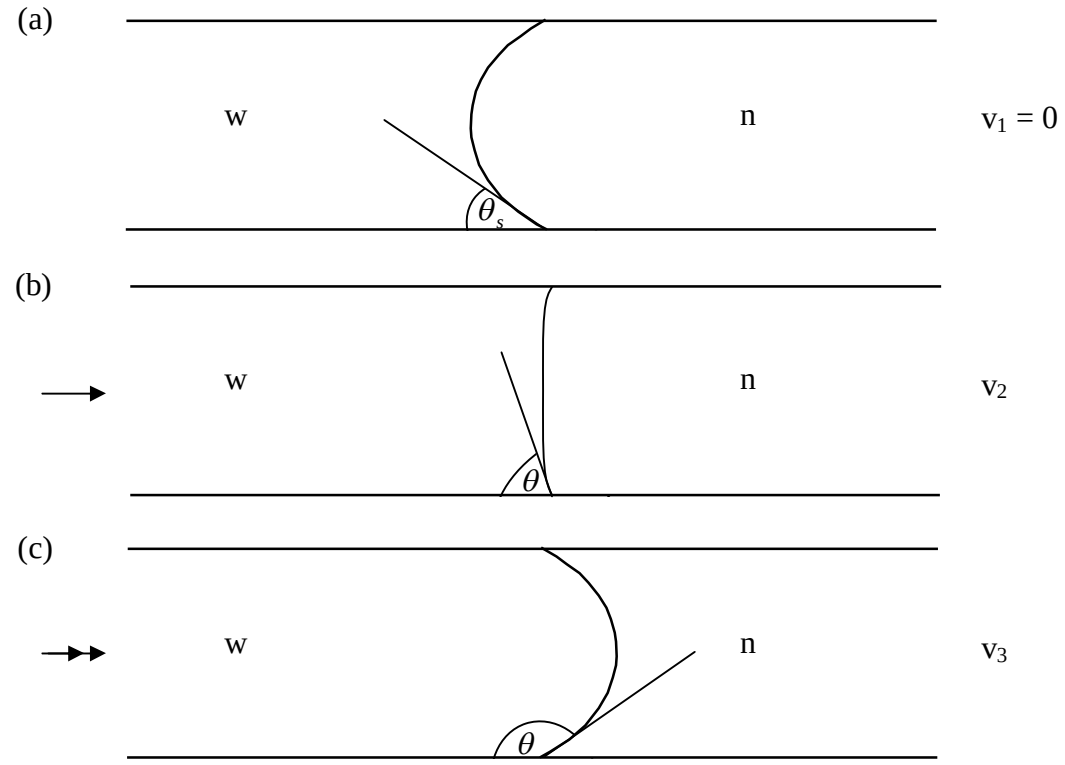


Figure 4.1: Three vertical sections through a Hele Shaw cell illustrate how the interface between wetting and non-wetting fluids changes as flow (from left to right) through the cell increases. (a) Depicts the interface under static, no flow conditions, (b) depicts interface under conditions of modest flow to the right, and (c) under substantial flow to the right. The contact angle that the fluid interface makes with the cell walls increases as the flow increases.

$A_{HT}$ is a constant which Hoffman [2] determined to have a value of ~ 200 for different silicone oils and air on glass. However published values of $A_{HT}$ vary greatly. For example, Bico et. al. [16] found $A_{HT}$ varied from 3 to 4 also for a silicone oil and air on glass, and Berthier [17] found $A_{HT}$ ~ 60 for a ferrofluid and air on glass. This suggests that the value of $A_{HT}$ depends on the fluids and the experimental design.

Weitz et. al. empirically related the capillary pressure to the interface velocity for porous media and Hele Shaw cell [4] and found:

$$\theta_d = A_W Ca^{\frac{1}{2}} + \theta_s . \qquad \ldots(4.4)$$

They found $A_w$ ~ 300 for decane and water in a glass porous medium.

Finally, Blake and Haynes [5, 12] derived a relationship from molecular-kinetic principles that has been successfully applied to a wide range of different geometries, including Hele Shaw cells. Their relationship was simplified by Martic et. al. [6]:

$$\cos\theta_d = \cos\theta_s - A_{BH} Ca , \qquad \ldots(4.5)$$

where $A_{BH} = \zeta / \mu$ = ~35, and $\zeta$ is a coefficient wholly based upon the molecular properties of the fluid. The value of $\zeta$ contributing to the $A_{BH}$ value quoted above is based upon the work of Bower [18] for ethanol on polyethylene terephthalate.

All three models are based upon a relationship between Ca and $\theta_d$. However wettability is known [10] to play an important role in the value of $\theta_s$, and is a surprising omission.

## 4.3 The Lattice Boltzmann Method (LBM)

The LBM solves the Navier Stokes equation by computing the movement of distributions of particles on a 2D or 3D cubic lattice. It has been validated extensively whilst being applied for ideal and non-ideal fluids [19-25], for high and low Reynolds number flows [26-28] as well as flows in complex geometries [23, 29-31]. The Lattice Boltzmann Method can be thought of occurring in two steps; translation and collision.

LBM simulations are carried out on a regular grid or lattice. Each unit cell of the lattice consists of a center point, known as a "node" on which resides $i$ groups of fractional numbers of particles, known as the particle density distribution, $f_i$. Each $f_i$ can be thought of residing on the $i^{th}$ link of the node, where the $i^{th}$ link provides a direct path between the node and its nearest neighbor node in the $e_i$ direction. Each of these neighbor nodes, in its own turn, can be considered a center node.

At the beginning of each timestep, $f_i$ moves to the closest node in the $i^{th}$ direction. In our case we use the 3DQ19 lattice, which is a 3D lattice with 19 velocity vectors, including a rest particle density distribution, $f_{i=0}$**.** The rest particle density distribution has zero velocity and so remains at the node after the translation has occurred. Six of the eighteen velocities are directed towards the center of each faces of the cube, and twelve are directed to the center of each of the cube's edges, as is illustrated in Fig 4.2. This translation is the first step of the simulation.

After translation, the particle density distributions arriving on the same node collide and are redistributed in a manner that conserves mass and momentum. This is the collision step. Body forces are applied by changing the overall particle momentum at a node at this step.

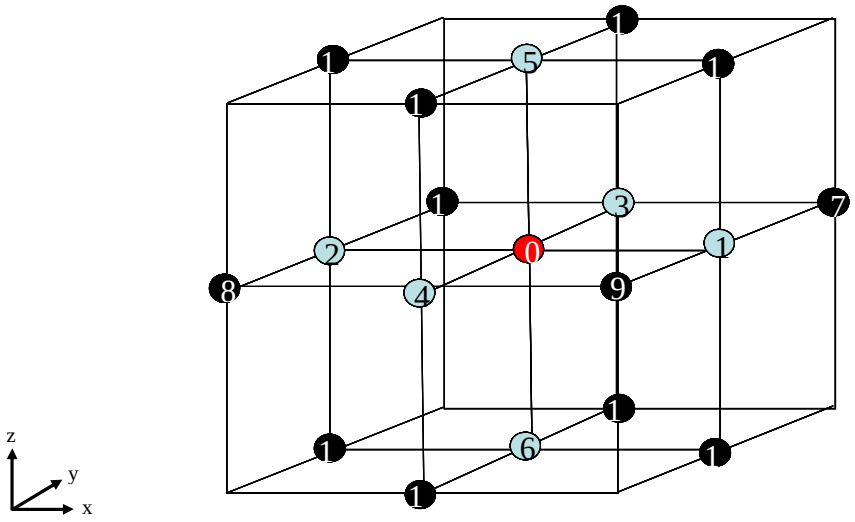


Figure 4.2: A unit cell of the LBM lattice is shown, with the locations of the 18 neighbor nodes, color coded by distance from the central node. The central node is red and is the location of the zero-velocity density distribution. The numbers of the links to the surrounding nodes are indicated in those nodes. The grey nodes are at the center of each of the faces of the cube, and the black nodes are at the middle of each of the edges of the cube.

The LBM equation describing the collision is a discretized version of the Boltzmann equation and can be written [32]:

$$\Delta_i f = -\frac{1}{\tau}(f_i - f_i^{eq}(F_i)), \qquad \ldots(4.6)$$

Here $f_i$ is the particle density distribution at the start of the time step in the $i^{th}$ direction, and $f_i^{eq}$ is the known equilibrium particle distribution, which incorporates any forces on the node, $F_i$. For a single fluid with no applied forces $f_i^{eq}$ is the ideal gas distribution. $\Delta_i f$ is the change in the particle distribution on the $i^{th}$ link of all nodes at the end of the time step after all particle collisions have taken place .

The relaxation time, $\tau$, controls how rapidly the solution converges to its equilibrium state and is related to the viscosity of the fluid. It is specified by the modeler and has units of time steps. The Navier Stokes equation is derived by substituting the Chapman-Enskog expansion of the distribution function into the mass and momentum continuum equations [33]. The viscosity of an LBM fluid is then determined by comparing the LBM Navier Stokes equation to the Navier Stokes equation for a macroscopic fluid. The kinematic viscosity of an LBM fluid is given by [34]:

$$\mu = \frac{c^2}{D}\left(\tau - \frac{1}{2}\right). \qquad \ldots(4.7)$$

Where c is the unit of velocity in lattice space and c = $\delta_x / \delta_t$. Here $\delta_x$ is the lattice constant and $\delta_t$ is the time step. For simplicity, in most cases, $\delta_x$ = 1 and $\delta_t$ = 1, resulting in c = 1 [30, 34]. D is the dimension of the system, where for flow in three

dimensions, D=3. From equation 5.4 we see that $\tau$ must be greater than ½ time step for physically reasonable viscosities. The unit of kinematic viscosity in lattice space is (lattice length)$^2$/time step which corresponds to the MKS units of kinematic viscosity $m^2/s$.

Fluid pressure is related to particle density:

$$P = \rho \frac{c^2}{D}, \qquad \ldots(4.8)$$

where $\rho$ is particle density and P is the fluid pressure in lattice pressure units, which is the nodal particle density times lattice length per time step squared.

Systems containing immiscible fluids are simulated by placing two particle distributions on each node, one for the non-wetting and one for the wetting fluid, and solving for the motion of each fluid using the LBM method described above. The interactions of the two fluids have been incorporated in several ways [1, 19-23, 35]. We use the LBM implementation of Shan and Chen. They calculate the density gradients for each fluid and apply a force to the particles:

$$F_n = g_{nn} \nabla \rho_n + g \nabla \rho_w \qquad \ldots(4.9)$$

$$F_w = g_{ww} \nabla \rho_w + g \nabla \rho_n, \qquad \ldots(4.10)$$

Where *n* indicates non-wetting and *w* indicates the wetting fluid. Judicious selection of values for $g_{nn}$, $g_{ww}$ and g provide forces that segregate the two fluids and simulate surface tension phenomenon. We follow Shan and Chen [1] by setting $g_{nn} = 0$ and $g_{ww} = 0$. Therefore, the additional segregating force in our simulations is:

$$F_n = \rho_n g \nabla \rho_w \quad \ldots(4.11)$$

$$F_w = \rho_w g \nabla \rho_n \quad \ldots(4.12)$$

Solid nodes are given different interaction parameters, $g_{sw}$ and $g_{sn}$, which define the degree of attraction or repulsion of the wetting and non-wetting fluids to the solid. In other words, $g_{sw}$ and $g_{sn}$ define the degree of wettability of each fluid.

$$F_w = \rho_w g_{sw} \nabla \rho_s \quad \ldots(4.13)$$

$$F_n = \rho_n g_{sn} \nabla \rho_n \quad \ldots(4.14)$$

Where $\rho_s$ is the density of the solid nodes surrounding the fluid node.

Particles approaching the solid boundary bounce off the boundary in a fashion that conserves their momentum parallel to the boundary and reverses their momentum perpendicular to the boundary. Pressure can be specified at a boundary by fixing particle density at the boundary nodes. In our LBM application, flow is imposed by specifying a body force and adapting cyclic boundary conditions. The cyclic boundary condition links the outflow and inflow boundaries numerically so that particles leaving one boundary enter the other.

In this paper we use a standard implementation of LBM that is fully described in Shan and Chen's pivotal paper [1]. We use an LBM computer code developed by

Ladd and Verberg [36] modified only by the addition, by us, of Shan and Chen's [1] segregation force for immiscible fluids.

## 4.4 Method

Figure 4.3 shows the simulation set-up for the immiscible fluid flow in a Hele Shaw cell numerical LBM experiments. The top and bottom boundaries (parallel to the x axis) are solid, no flow boundaries. The other boundaries are cyclic (e.g. the boundaries perpendicular to the x axis are connected numerically so that particles exiting one end reenter the other end). There are 100 nodes (L) along the x axis, 8 along the y axis and 24 along the z axes. The 3D grid contains of 19,200 nodes.

Initially we place the wetting fluid in the lower ($x < L/2$) half of the Hele Shaw cell and the non-wetting fluid in the upper half of the Hele Shaw cell ( $x \geq L/2$ ). The average fluid density of each fluid, at each node, is 0.1. Particles at each node are distributed equally between each of the 19 nodal links.

We undertake two separate experiments; one to investigate the accuracy of the three contact angle-velocity relationships and the other to investigate the affect of wettability on the dynamic contact angle.

To investigate the accuracy of the three contact angle-velocity relationships, a body force is applied to the wetting fluid in the z direction with magnitude varying between $0 \leq Fx \leq 0.0005$. We vary the surface tension between the fluids by varying $-1.6 \leq g \leq -0.9$ resulting in the surface tension, $\sigma$, varying $0.01175 \leq \sigma \leq 0.02085$ in lattice surface tension units. We examine the interface after 250 time steps for the eight different body forces. The parameters used in our modeling are summarized in Table 4.1.

To investigate how wettability affects the dynamic contact angle, we repeated the experiment for g = -1.3, under the eight different forcings, and repeated this set of

experiments for six different wettability conditions. We varied the wettability condition by changing $g_{sw}$ and $g_{sn}$, where we defined the degree of wettability as $1/\theta_s$ .

Results of the flow simulations are presented by plotting the dynamic contact angle against the capillary number. The fluid viscosity is determined from equation (4.7). For the relaxation parameter used in our simulations ($\tau$=1), $\mu$=1/6. The interface velocity, measured in lattice units per time step, is determined visually from changes in the position of the interface after equilibrium has been reached at around 250 time steps. The density is the mean density taken upstream of the interface.

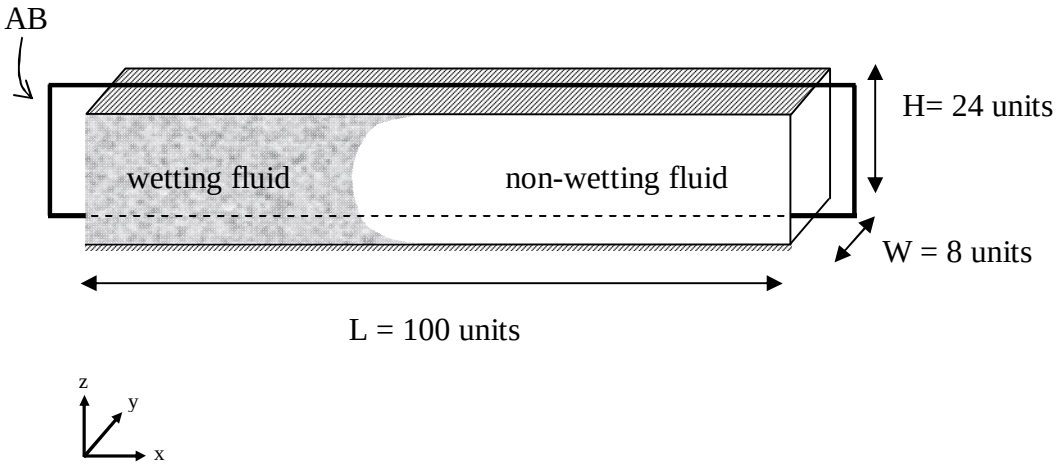


Figure 4.3: Geometry of the LBM experiment.

Table 4.1: Parameters used in the LBM simulations.

| | | |
|---|---|---|
| $L_x$ | Number nodes in x direction | 100 |
| $L_y$ | Number nodes in y direction | 8 |
| $L_z$ | Number nodes in z direction | 24 |
| $\tau$ | Relaxation parameter | 1 |
| $g_{nw}=g$ | Particle repulsion between fluids | -0.9 to -1.6 |
| $g_{sw}$ | Solid boundary force on wetting fluid | 1 |
| $g_{sn}$ | Solid boundary force on non-wetting fluid | -10 |
| $F_x$ | Body force imposed each time step | 0.0 – 0.005 |
| $\rho_w^{initial}\Big\|_{x\le L/2}$ | Density of wetting fluid initially assigned to $x \le L/2$ | 0.1 |
| $\rho_n^{initial}\Big\|_{x>L/2}$ | Density of non-wetting fluid initially assigned to $x > L/2$ | 0.1 |

Interfacial tension is related to the interaction parameter, g. This relationship was determined using Laplace's Law which states that the pressure inside a bubble of radius r will be greater that that outside the bubble by the capillary pressure $P_c$:

$$P_c = \frac{2\sigma}{r} \qquad \ldots(4.15)$$

We determined the relationship between g and σ through a series of LBM simulations. In each we placed different volumetric ratios of wetting to non-wetting fluid in a box of 20 units in dimension with periodic boundary conditions placed on each of the six sides. Once the system achieved equilibrium, we measured the difference in particle densities of the two fluids and converted them to pressure using Eq. 4.8. For each value of the interaction parameter (g), we then calculated the surface tension from the radius of the non-wetting bubble (Eq.4.15). In this fashion, we found the surface tensions for five different values of g. The Laplace results for all g may be found in Appendix C. The calculated pressure and radius values for 6 different values of g are given in Table 4.2 (see also Tables C.1-C.6 in Appendix C). The surface tension values for each g are plotted as a function of σ in Figure 4.4. The relationship is linear, and the linear regression show Figure 4.4 is used to determine σ from g in order to calculate the capillary number:

$$Ca = \frac{\rho\mu u}{\sigma} = \frac{\rho c^2 u\left(\tau - \frac{1}{2}\right)}{D\left(C_g g + A_g\right)} = \frac{\rho u}{6\left(C_g g + A_g\right)}, \qquad \ldots(4.16)$$

Where $C_g$ and $A_g$ are derived from the empirical relationship shown in Fig 4.4, $\sigma = C_g g + A_g$ . $\rho u$ are in units of lattice momentum, and $C_g g + A_g$ has units of lattice surface tension. This is equivalent to (lattice length)(particle mass)/(time steps)$^2$.

Table 4.2: Surface tensions for different values of the interaction parameter, g.

| g | -1.05 | -1 | -0.95 | -0.9 | -0.85 |
|---|---|---|---|---|---|
| σ | 0.0136 | 0.0131 | 0.0123 | 0.0118 | 0.0111 |

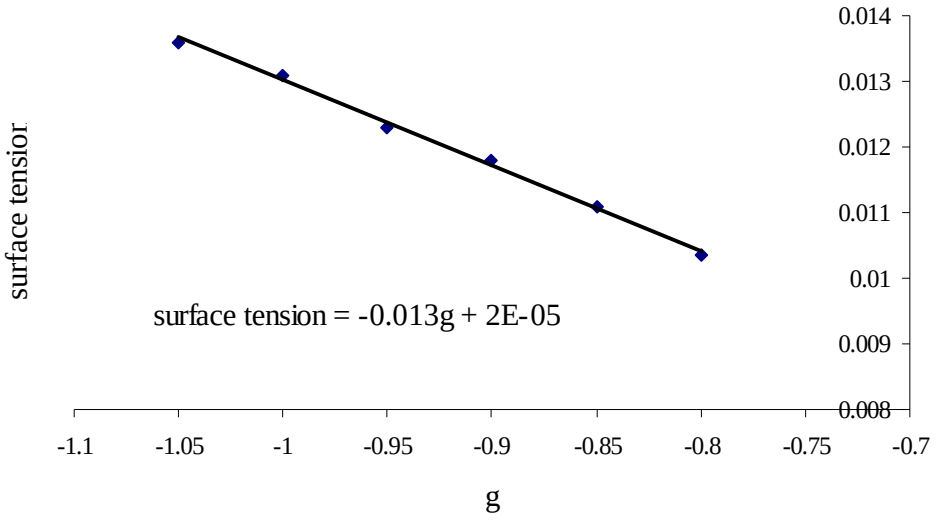


Figure 4.4: Correlation between the interaction parameter (g) and surface tension.

## 4.5 Results

### A. Accuracy of the three contact angle-velocity relationships.

Figure 4.5 shows how the shape of the fluid interface changes as fluid is forced at increasing rates through the Hele Shaw cell. The results shown in Figure 4.5 is for g = -1.1. The corresponding results for g = -0.9 g = -1.3, g = -1.4, g = -1.5 and g = -1.6 are shown in the Appendix B. Figure 4.5 shows that as the body force driving fluid through the tube increases, the upstream interface between the non-wetting and wetting fluids becomes increasingly concave, while the interface on the downstream side becomes less concave (with respect to the wetting fluid). For g =-1.1, at $F_x$ = 0.0005 it is flat, and at $F_x$ = 0.001 it becomes convex.

Figure 4.6 illustrates how we measure the contact angle. The interface between the wetting and non-wetting fluid is defined as the surface at which the density of the wetting fluid is 60% of its highest value. The $\rho u$ is measured as the average value upstream of the interface.

Figures 4.7 through 4.9 compare our numerical relationship to that suggested by the Hoffman Tanner, Weitz, and Blake and Haynes relationships, all computed with g= -1.1. Tables 4.4 through Table 4.6 show the correlation coefficient for each of the three velocity-dynamic contact angle relationships. The Hoffman Tanner relationship clearly provides the best fit our numerical simulation data.

The fitting coefficients change as the surface tension changes. For the Hoffman Tanner relationship for example, we see that the coefficient, $A_{HT}$, decreases as the surface tension increases. This may explain the range of $A_{HT}$ quoted in the literature.

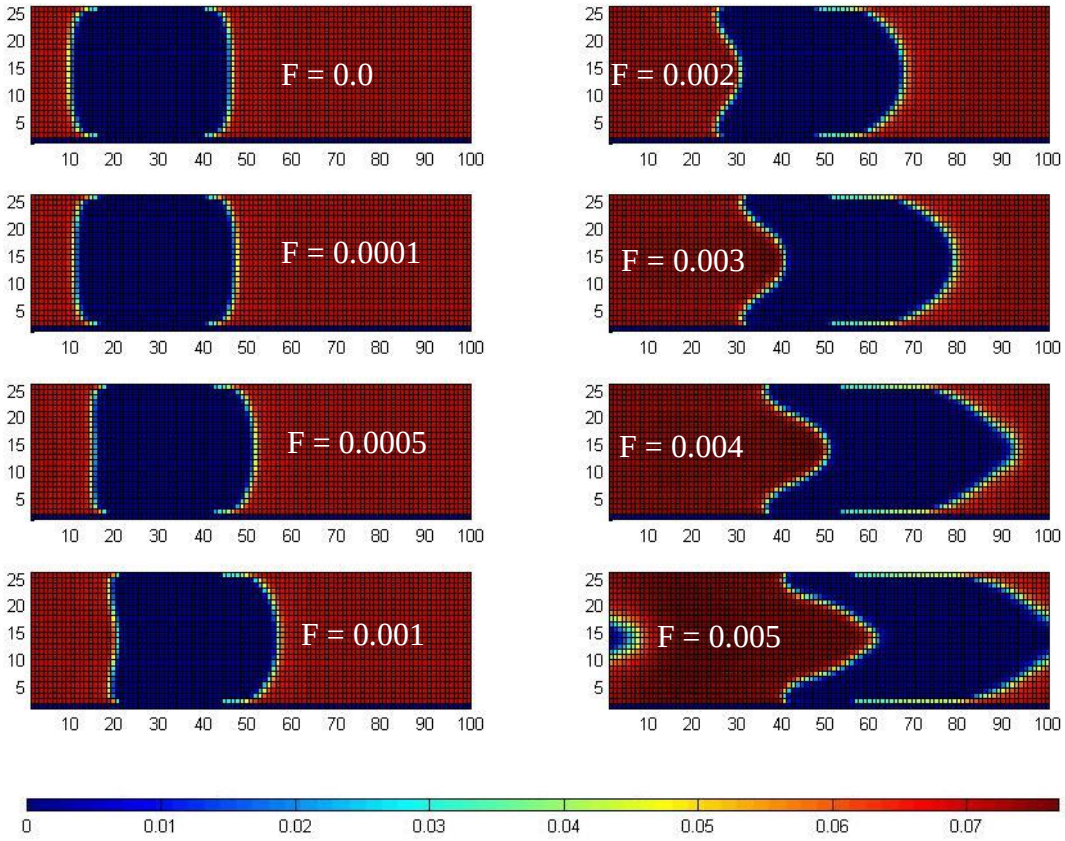


Figure 4.5: Illustration of the wetting fluid density, for g = 1.1, within a Hele Shaw cell as the forcing is increased.

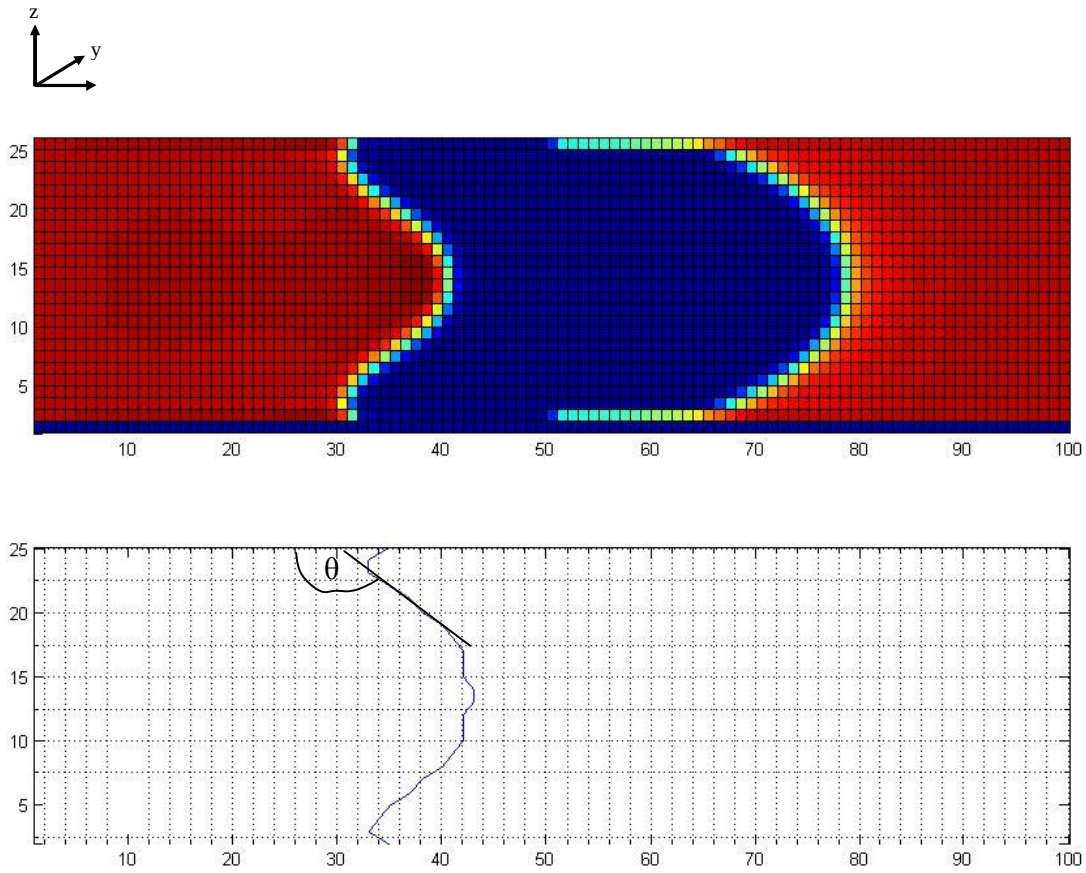


Figure 4.6: Section through phase boundary along the central y plane. The fluid boundary is defined by the non-wetting fluid saturation and is the surface at which the non-wetting fluid saturation is 90% of its maximum value in the simulation. The contact angle is determined by the shape of the interface a short distance from the sides of the Hele Shaw cell.

Table 4.3 gives the ρu, θ and Ca results. Figure 4.7 through Figure 4.9 plots the results for an interfacial tension of 0.01432. ρu is in units of lattice momentum.

Table 4.3: Measured $\theta_d$ and Ca

| g = -0.09, σ = 0.01172 | | | | | | | | |
|---|---|---|---|---|---|---|---|---|
| F | 0 | 0.00001 | 0.00005 | 0.0001 | 0.0002 | 0.0003 | 0.0004 | 0.0005 |
| ρu | 0 | 0.00075 | 0.0015 | 0.003 | 0.0045 | 0.0075 | 0.012 | 0.0195 |
| θ | 16 | 70 | 90 | 117 | 130 | 141 | 163 | 180 |
| Ca | 0 | 0.0107 | 0.0213 | 0.0427 | 0.0640 | 0.1067 | 0.1706 | 0.2773 |
| g = -1.1, σ = 0.01432 | | | | | | | | |
| F | 0 | 0.00001 | 0.00005 | 0.0001 | 0.0002 | 0.0003 | 0.0004 | 0.0005 |
| ρu | 0 | 0.00075 | 0.0015 | 0.003 | 0.006 | 0.0075 | 0.01125 | 0.018 |
| θ | 30 | 58 | 76 | 90 | 127 | 136 | 150 | 164 |
| Ca | 0 | 0.0087 | 0.0175 | 0.0349 | 0.0698 | 0.0873 | 0.1309 | 0.2095 |
| g = -1.3, σ = 0.01692 | | | | | | | | |
| F | 0 | 0.00001 | 0.00005 | 0.0001 | 0.0002 | 0.0003 | 0.0004 | 0.0005 |
| ρu | 0 | 0.00075 | 0.0015 | 0.00225 | 0.0045 | 0.0075 | 0.0105 | 0.0195 |
| θ | 35 | 72 | 86 | 90 | 117 | 135 | 153 | 164 |
| Ca | 0.0000 | 0.0074 | 0.0147 | 0.0221 | 0.0442 | 0.0737 | 0.1032 | 0.1917 |
| g = -1.4, σ = 0.01822 | | | | | | | | |
| F | 0 | 0.00001 | 0.00005 | 0.0001 | 0.0002 | 0.0003 | 0.0004 | 0.0005 |
| ρu | 0 | 0.00075 | 0.0015 | 0.00225 | 0.0045 | 0.0075 | 0.0105 | 0.0165 |
| θ | 40 | 75 | 85 | 90 | 120 | 140 | 153 | 155 |
| Ca | 0.0000 | 0.0069 | 0.0137 | 0.0206 | 0.0412 | 0.0686 | 0.0960 | 0.1509 |

Table 4.3 Continued

| g = -1.5, σ = 0.01952 | | | | | | | | |
|---|---|---|---|---|---|---|---|---|
| F | 0 | 0.00001 | 0.00005 | 0.0001 | 0.0002 | 0.0003 | 0.0004 | 0.0005 |
| ρu | 0 | 0.00075 | 0.0015 | 0.00225 | 0.0045 | 0.0075 | 0.009 | 0.018 |
| θ | 51 | 69 | 80 | 90 | 120 | 135 | 144 | 165 |
| Ca | 0.0000 | 0.0064 | 0.0128 | 0.0192 | 0.0384 | 0.0639 | 0.0767 | 0.1535 |
| g = -1.6, σ = 0.02082 | | | | | | | | |
| F | 0 | 0.00001 | 0.00005 | 0.0001 | 0.0002 | 0.0003 | 0.0004 | 0.0005 |
| ρu | 0 | 0.000375 | 0.00075 | 0.0015 | 0.0045 | 0.0075 | 0.0105 | 0.0135 |
| θ | 60 | 66 | 74 | 92 | 120 | 130 | 145 | 155 |
| Ca | 0.0000 | 0.0030 | 0.0060 | 0.0120 | 0.0360 | 0.0600 | 0.0841 | 0.1081 |

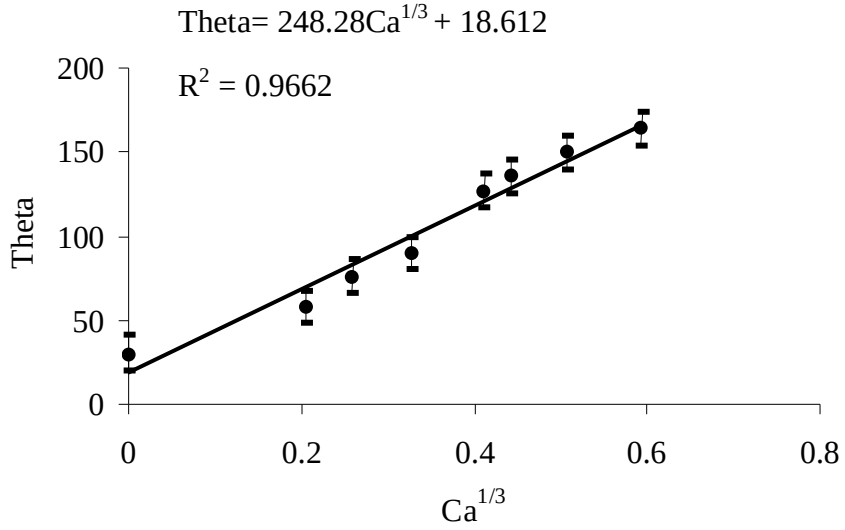


Figure 4.7: Example of the correlation plot for the Hoffman Tanner law, obtained for g=-1.1. To compare with the Hoffman–Tanner law, the dynamic contact angle is plotted against $Ca^{1/3}$. Ca is the capillary number which equals $\upsilon u/\sigma$, where $\upsilon$ is the dynamic viscosity, u is the velocity of the phase boundary, and $\sigma$ is the interfacial tension between the wetting and non-wetting phases.

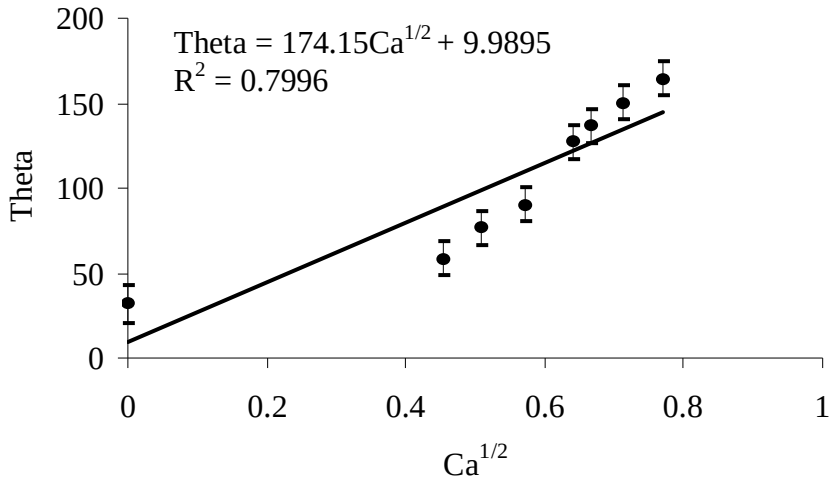


Figure 4.8: Example of the correlation plot for the Weitz et. al. relationship, obtained for g=-1.1. To compare with the Weitz relationship, the dynamic contact angle is plotted against $Ca^{1/2}$.

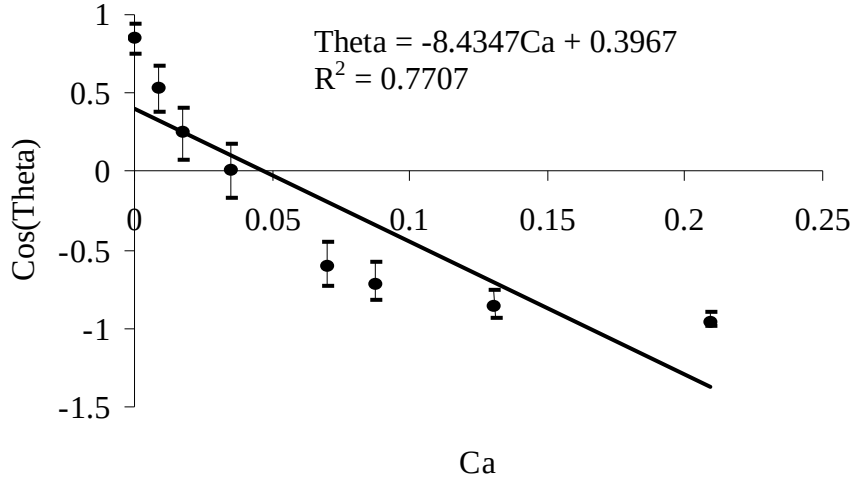


Figure 4.9: Example of the correlation plot for the Blake and Haynes relationship, obtained for g=-1.1. To compare with the Blake and Haynes relationship, the cosine of the dynamic contact angle is plotted against Ca.

Table 4.4: Summary of results from LBM simulations for comparison with the Hoffman Tanner model [2, 3]. : $\theta_d = A_{HT} Ca^{\frac{1}{3}} + \theta_s$

| g | Surface Tension | $\theta_s$ | $A_{HT}$ | Regression fit with data ($R^2$) |
|---|---|---|---|---|
| -0.9 | 0.01172 | $16^o$ | 258.63 | 0.989 |
| -1.1 | 0.01432 | $32^o$ | 248.28 | 0.9662 |
| -1.3 | 0.01692 | $34^o$ | 241.77 | 0.9806 |
| -1.4 | 0.01822 | $40^o$ | 241.05 | 0.9672 |
| -1.5 | 0.01952 | $50^o$ | 235.84 | 0.9418 |
| -1.6 | 0.02082 | $59^o$ | 220.61 | 0.946 |

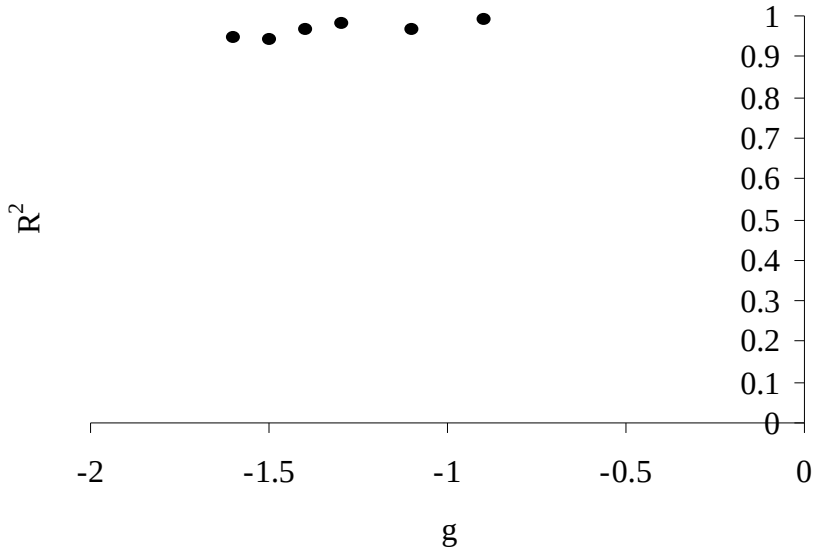


Figure 4.10: Illustration of the Regression fit depends upon g, after the data is fitting against the Hoffman –Tanner relationship.

Table 4.5: Summary of results from LBM simulations for comparison with the Weitz et. al. [4]. $\theta_d = A_W Ca^{\frac{1}{2}} + \theta_s$

| g | Surface Tension | $\theta_s$ | $A_W$ | Regression fit with data ($R^2$) |
|---|---|---|---|---|
| -0.9 | 0.01172 | $16^o$ | 203.54 | 0.92 |
| -1.1 | 0.01432 | $32^o$ | 174.15 | 0.7996 |
| -1.3 | 0.01692 | $34^o$ | 172.23 | 0.8507 |
| -1.4 | 0.01822 | $40^o$ | 165.07 | 0.8317 |
| -1.5 | 0.01952 | $50^o$ | 153.31 | 0.742 |
| -1.6 | 0.02082 | $59^o$ | 142.69 | 0.7416 |

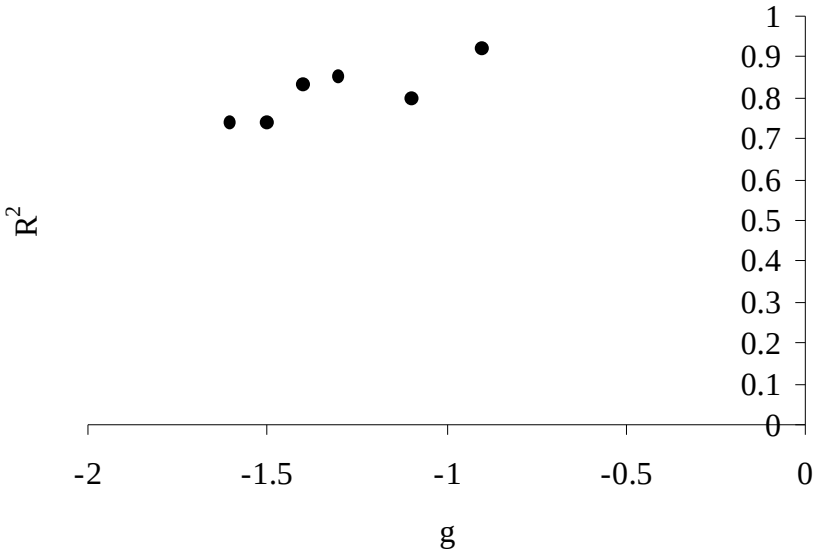


Figure 4.11: Illustration of the Regression fit depends upon g, after the data is fitting against the Weitz et. al. relationship.

Table 4.6: Summary of results from LBM simulations for comparison with the Blake and Haynes [5, 6, 12]: $\cos\theta_d = \cos\theta_s - A_{BH} Ca$

| g | Surface Tension | $\theta_s$ | $A_{BH}$ | Regression fit with data ($R^2$) |
|---|---|---|---|---|
| -0.9 | 0.01172 | $16^o$ | -5.6622 | 0.6051 |
| -1.1 | 0.01432 | $32^o$ | -8.4347 | 0.7707 |
| -1.3 | 0.01692 | $34^o$ | -8.185 | 0.7113 |
| -1.4 | 0.01822 | $40^o$ | -10.142 | 0.7517 |
| -1.5 | 0.01952 | $50^o$ | -10.094 | 0.758 |
| -1.6 | 0.02082 | $59^o$ | -13.013 | 0.8809 |

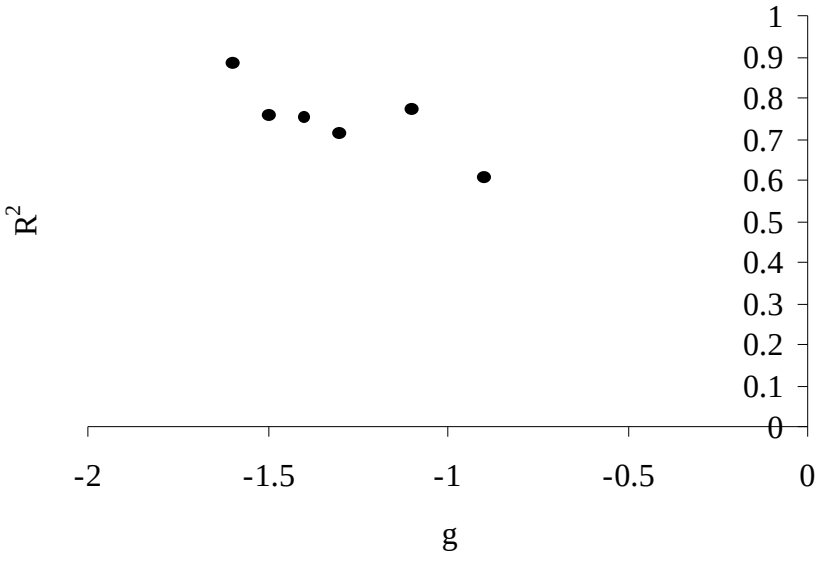


Figure 4.12: Illustration of the Regression fit depends upon g, after the data is fitting against the Blake and Haynes relationship.

B. Wettability affects

Figure 4.13 shows the changes in the static (F=0) wetting angle $\theta_s$ that result from different values of surface wettability. The dependence of $\theta_s$ on $g_{ws}$ suggests that wettability enters the Hoffman Tanner and other wetting angle laws through the static wetting angle. As the wettability becomes stronger, the static contact angle becomes smaller, and the flow rate (Capillary number) required to reverse the polarity of the interface increases. The Law remains as valid as before but the flow velocity coefficients are also changed. For example, Figure 4.14 shows the quality of the Hoffman tanner relationship for $g_{sw}$=1, $g_{sn}$=-20 ( $\theta_s = 27^o$) remains as good as that shown in Figure 4.7 where $g_{sw}$=1, $g_{sn}$=-10 ($\theta_s = 45^o$). The Hoffman Tanner $A_{HT}$ coefficient changes from 248.28 to 256.5. Thus, changes in wettability are another reason that the value of the $A_{HT}$ coefficient determined in different experiments varies. This is shown in Figure 4.15.

The effect of wettability can be quite dramatic in a laboratory experiment. For example, Figure 4.16 shows that the fluid velocity at which the interface curvature changes direction can change by a factor of more than two as the wettability of the surface changes.

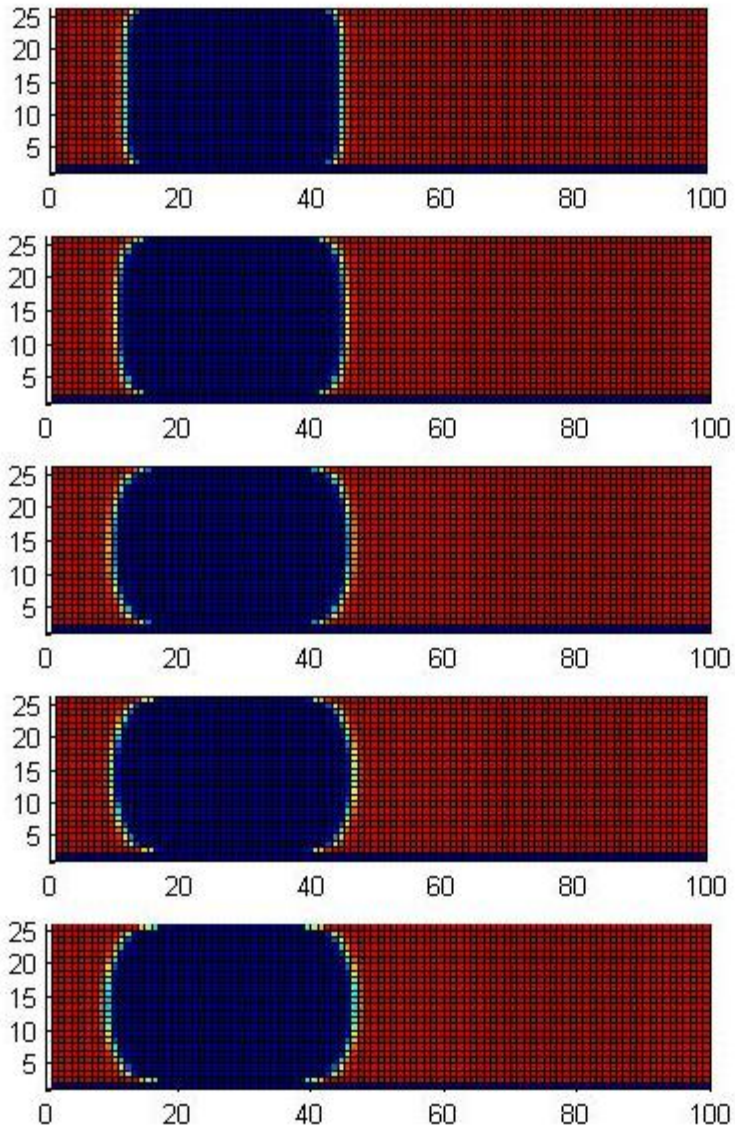


Figure 4.13: Illustration of the fluid interface, showing the static contact angle for the five sets of wettability conditions. The value of g, $g_{ww}$ and $g_{nn}$ is the same for all cases so that g = -1.3, $g_{ww} = g_{nn} = 0$. From Table 4.6, we see that the interfacial tension for all cases is $\sigma = 0.01692$.

Table 4.7: Measured $\theta_d$ and Ca

| | | | | | | | | |
|---|---|---|---|---|---|---|---|---|
| $\frac{1}{\theta_s} = 0.0179$ | | | | | | | | |
| F | 0 | 0.00001 | 0.00005 | 0.0001 | 0.0002 | 0.0003 | 0.0004 | 0.0005 |
| ρu | 0 | 0.00075 | 0.0015 | 0.00225 | 0.0045 | 0.0075 | 0.012 | 0.0165 |
| θ | 56 | 75 | 90 | 113 | 130 | 141 | 158 | 169 |
| Ca | 0 | 0.00739 | 0.01478 | 0.02216 | 0.04433 | 0.07388 | 0.1182 | 0.16253 |
| $\frac{1}{\theta_s} = 0.0222$ | | | | | | | | |
| F | 0 | 0.00001 | 0.00005 | 0.0001 | 0.0002 | 0.0003 | 0.0004 | 0.0005 |
| ρu | 0 | 0.00075 | 0.0015 | 0.003 | 0.0045 | 0.009 | 0.0105 | 0.0195 |
| θ | 45 | 67 | 85 | 92 | 122 | 135 | 149 | 165 |
| Ca | 0 | 0.00739 | 0.01478 | 0.02955 | 0.04433 | 0.08865 | 0.10343 | 0.19208 |
| $\frac{1}{\theta_s} = 0.0294$ | | | | | | | | |
| F | 0 | 0.00001 | 0.00005 | 0.0001 | 0.0002 | 0.0003 | 0.0004 | 0.0005 |
| ρu | 0 | 0.00075 | 0.0015 | 0.003 | 0.006 | 0.0075 | 0.0105 | 0.0195 |
| θ | 34 | 50 | 60 | 90 | 120 | 135 | 145 | 160 |
| Ca | 0 | 0.00739 | 0.01478 | 0.02955 | 0.0591 | 0.07388 | 0.10343 | 0.19208 |
| $\frac{1}{\theta_s} = 0.0370$ | | | | | | | | |
| F | 0 | 0.00001 | 0.00005 | 0.0001 | 0.0002 | 0.0003 | 0.0004 | 0.0005 |
| ρu | 0 | 0.00075 | 0.0015 | 0.003 | 0.0045 | 0.006 | 0.0105 | 0.0195 |
| θ | 27 | 45 | 55 | 80 | 121 | 135 | 141 | 158 |
| Ca | 0 | 0.00739 | 0.01478 | 0.02955 | 0.04433 | 0.0591 | 0.10343 | 0.19208 |

| Table 4.7 continued | | | | | | | | |
|---|---|---|---|---|---|---|---|---|
| $\frac{1}{\theta_s} = 0.0526$ | | | | | | | | |
| F | 0 | 0.00001 | 0.00005 | 0.0001 | 0.0002 | 0.0003 | 0.0004 | 0.0005 |
| ρu | 0 | 0.00075 | 0.0015 | 0.003 | 0.0045 | 0.00825 | 0.009 | 0.012 |
| θ | 19 | 45 | 70 | 85 | 120 | 131 | 141 | 151 |
| Ca | 0 | 0.00739 | 0.01478 | 0.02955 | 0.04433 | 0.08126 | 0.08865 | 0.1182 |

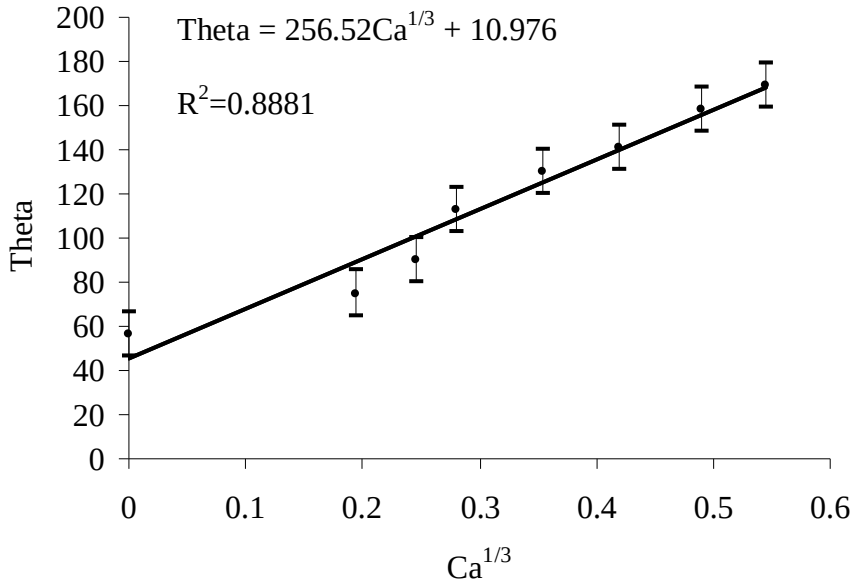


Figure 4.14: Example of the correlation plot for the Hoffman Tanner, obtained for g=-1.3, with $\frac{1}{\theta_s} = 0.0370$. The remaining plots may be found in Appendix B.

Table 4.8: Summary of the different wettability results, for g = -1.3 and σ=0.01692, in comparison with the Hoffman Tanner model [2, 3]. : $\theta_d = A_{HT} Ca^{\frac{1}{3}} + \theta_s$

| $1/\theta_s$ | $A_{HT}$ | Regression fit with data ($R^2$) |
|---|---|---|
| 0.018 | 224.3 | 0.9579 |
| 0.022 | 226.444 | 0.9555 |
| 0.029 | 253.83 | 0.9241 |
| 0.027 | 265.52 | 0.881 |
| 0.053 | 290.74 | 0.9591 |

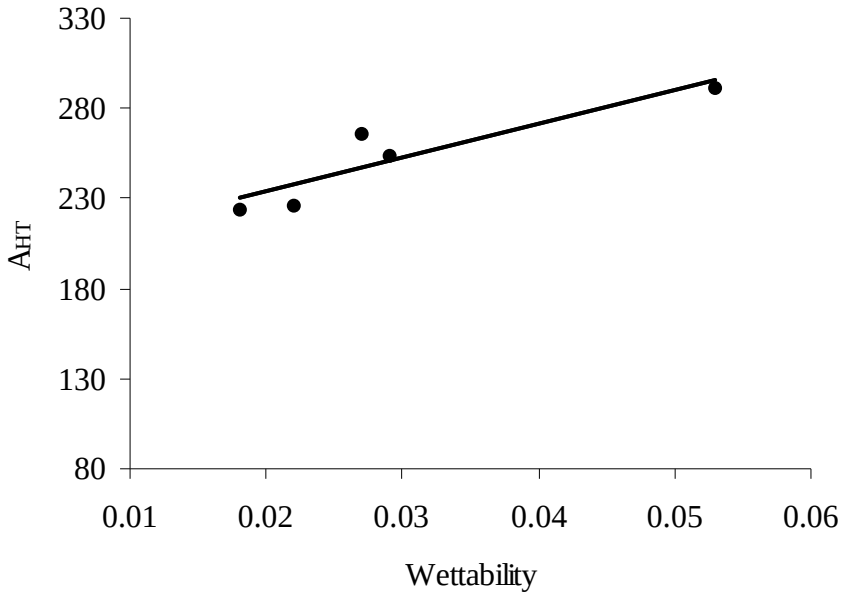


Figure 4.15: Illustration of the dependence of $A_{HT}$ with wettability.

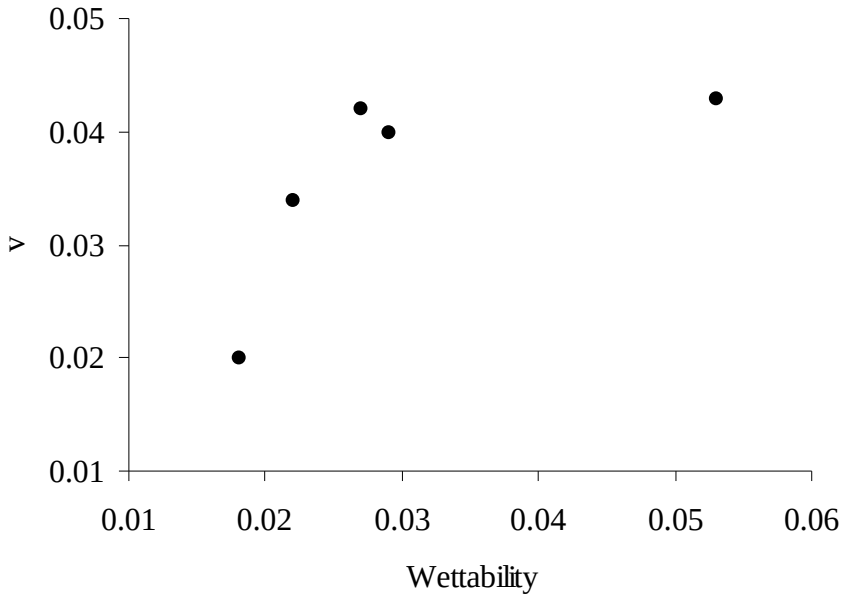


Figure 4.16: Affect of wettability upon the velocity at which the interface curvature switched polarity, taken to be when the $\theta = 90^{o}$. When necessary, the velocities were estimated by linear interpolation.

## 4.6 Conclusion

Using the Lattice Boltzmann Method to numerically simulate immiscible fluid flow, the response of the wetting/non-wetting interface to changes in the pressure gradient across a Hele Shaw cell is investigated. The affect of wettability upon the dynamic contact angle, for a given surface tension is also investigated using the same methodology.

With increasing velocity of the interface through the cell, the interface first flattens (as the radius of curvature increases) and then becomes convex (when the radius of curvature reverses sign). This is observed in laboratory Hele Shaw cell experiments.

The relationship between the LBM dynamic contact angle and the LBM interface velocity is found to be best fit by the Hoffman-Tanner law. The Weitz's and the Blake and Haynes relation both fit the data reasonably, but less accurately. In addition the quality of the predictions of the Weitz et. al and Blake and Haynes Laws depend on the LBM interfacial tension whereas the quality of the Hoffman-Tanner predictions of the dynamic contact angle is almost independent of interfacial tension.

It should be noted that the estimate of the coefficient of proportionality, $A_{HT}$, is found to be the same order of magnitude as obtained by Hoffman [7] for our range of data. The Hoffman-Tanner coefficient increases with wettability and decreases with surface tension, thus providing a possible explanation for the widely varying Hoffman-Tanner coefficients reported in the literature.

# REFERENCES


1. X. Shan and Chen H., *Lattice Boltzmann Model for Simulating Flows with Multiple Phases and Components*, Phy. Rev E, 1993, 47(3):pp.1815-1820.

2. R. L. Hoffman, *Study of Advancing Interface. 1. Interface Shape in Liquid-Gas Systems.* Journal of Colloid and Interface Science, 1975, 50(2): pp.228-241.

3. L. H. Tanner, *Spreading of Silicone Oil Drops on Horizontal Surfaces.* Journal of Physics D - Applied Physics, 1979, 12(9): p.1473.

4. D. A. Weitz et al., *Dynamic Capillary Pressure in Porous Media: Origin of the Viscous-Fingering Length Scale.* Physical Review Letters, 1987, 59(26): pp2967-2970.

5. T. D. Blake and Haynes J.M., Journal of Colloid and Interface Science, 1969. 30(421).

6. G. Martic et. al., *A Molecular Dynamic Simulation of Capillary Imbibition*, Langmuir, 2002, 18:pp.7971-7976.

7. R. L. Chuoke, van Meurs P., and van der Poel C., *The Instability of Slow, Immiscible, Viscous Liquid-Liquid Displacements in Permeable Media.* Transactions of the American Institute of Mining and Mettallurgical Engineers, 1959, 216: pp.188-194.

8. J. Y. Parlange and Hill S., *Theoretical Analysis of Wetting Front Instability in Soils,* Soil Science, 1976s 122(4): pp.236-239.

9. E.B. Dussan, *Spreading of Liquids on Solid-Surfaces - Static and Dynamic Contact Lines.* Annual Review of Fluid Mechanics, 1979, 11: pp.371-400.

10. P. G. de Gennes, *Wetting - Statics and Dynamics.* Reviews of Modern Physics, 1985. 57: p. 827.

11. S. F. Kistler, in *Wettability*, J.C. Berg, Editor. 1993, Dekker: New York, pp.311-429.

12. T. D. Blake, in *Wettability*, J.C. Berg, Editor. 1993, Dekker: New York, pp.251-309.

13. S. Schiaffino and Sonin A.A., *Molten Droplet Deposition and Solidification at Low Weber Numbers.* Physics of Fluids, 1997, 9(11):pp.3172-3187.

14. O. V. Voinov, Sov. Phys. Dokl., 1978, 23:pp.891-893.

15. W. Boender, Chesters A.K. and van der Zanden A.J.J., *An Approximate Analytical Solution of the Hydrodynamic Problem Associated with an Advancing Liquid Gas Contact Line.* International Journal of Multifluid Flow, 1991, 17(5):pp. 661-676.

16. J. Bico and Quere D., *Falling Slugs.* Journal of Colloid and Interface Science, 2001,243(1):pp.262-264.

17. J. Berthier and Ricoul F., *Numerical Modeling of Ferrofluid Flow Instabilities in a Capillary Tube at the Vicinity of a Magnet*. in *International Conference on Modeling and Simulation of Microsystems*. 2002. San Juan, Puerto Rico.

18. T. D. Blake, De Coninck J. Advances in Colloid Interface Science, 2002, 96(21).

19. X. Shan and Chen H., *Simulation of Nonideal Gases and Liquid-Gas Fluid Transitions by the Lattice Boltzmann Equation*. Phys. Rev E., 1994, 49:pp.2941-2948.

20. M. Swift, Osborn W. R., and Yeomans J. M., *Lattice Boltzmann Simulation of Nonideal Fluids.* Phys. Rev. Lett., 1995, 75(5):pp.830-833.

21. M. Swift et al., *Lattice Boltzmann Simulation of Liquid Gas and Binary Fluid Systems,* Phys. Rev. E., 1996, 54(5):pp.5041-5052.

22. A. K. Gunstensen et al., *Lattice Boltzmann Model of Immiscible Fluids.* Phys. Rev. A, 1991, 43(8):pp.4320-4327.

23. A. K. Gunstensen and Rothman D., *Lattice-Boltzmann Studies of Immiscible Two –Fluid Flow Through Porous Media.* J. Geophys. Res., 1993, 98(B4):pp.6431-6441.

24. C. Appert and Zaleski S., Physical Review Letters, 1990, 64(1).

25. G. McNamara and Alder B., *Analysis of the Lattice Boltzmann Treatment of Hydrodynamics*, Physica A, 1993, 194: pp.218-228.

26. R. Benzi and Succi S., *Two-Dimensional Turbulence with the Lattice Boltzmann Equation*, 1990, J. Phys. A: Math. Gen., 23:pp.L1-L5.

27. S. Succi, *The Lattice Boltzmann Equation for Fluid Dynamics and Beyond*, 1st ed., 2001, Oxford: Oxford University Press.

28. O. Filippova et. al., *Multiscale Lattice Boltzmann Schemes with Turbulence Modeling,* Journal of Computational Physics, 2001, 170(2):pp.812-829.

29. R. Benzi, Succi S. and Vergassoa M., *The Lattice Boltzmann Equation - Theory and Applications.* Phys. Rep., 1992, 222(3): pp.145-197.

30. N. S. Martys and Chen H., *Simulation of Multicomponent Fluids in Complex Three-Dimensional Geometries by the Lattice Boltzmann Method*, Physical Review E, 1996, 53(1):pp.743.

31. D. Rothman, J. Geophys. Res., 1990, 95:pp.8663.

32. S. Chen and Doolen D., *Lattice Boltzmann Method for Fluid Flows.* Annu. Rev. Fluid Mech., 1998, 30:pp.329-364.

33. F. J. Alexander et. al., *Lattice Boltzmann Model for Compressible Fluids*, Phys. Rev. A., 1991, 46(4):pp.1967-1970.

34. V. Sofonea and Sekerka R., *Viscosity of Finite Difference Boltzmann Models*, Journal of Computational Physics, 2003, 184:pp.422-434.

35. S. Chen et al., *Lattice Boltzmann Model for Simulation of Magnetohydrodynamics.* Phys. Rev. Lett., 1991, 67:pp.3776-3779.

36. A. J. C. Ladd and Verberg R., *Lattice-Boltzmann Simulations of Particle-Fluid Suspensions*, J. Stat. Physics, 2001,104(516):pp.1191-1251.

# Chapter 5. Conclusion and Summary

## 5.1 Conclusion and Summary

This thesis was undertaken to investigate how capillary seals maintain abnormally pressured compartments over geological time. Of particular interest was the conditions under which a non-wetting fluid phase could prevent the motion of the wetting phase. Critics of the capillary sealing hypothesis maintained that the wetting fluid would flow through the seal, albeit with a very low relative permeability. Geologic evidence and experiments run at Cornell suggested the blockage was total and there was no slow leakage.

Numerical simulation of the capillary blockage (no flow) is challenging. Previous modeling attempts [1] using traditional finite difference methods proved difficult due to numerical instabilities. The Lattice Boltzmann Method promised to be a method that could handle these instabilities since it is based upon a discretized Boltzmann equation, rather than a discritized Navier Stokes equation, and has been shown to easily simulate multiple immiscible fluids and complex boundaries, issues which were the cause of the instabilities in previous attempts.

The Lattice Boltzmann Method proved capable of simulating capillary sealing in an instructive fashion. Through careful analysis of the z-momentum plots of the wetting fluid we concluded that there is no wetting fluid flow through a blocked pore. Our experiments also indicated that the capillary pressure across a single coarse/fine interface is cumulative, and the simulations show how capillary seals can re-heal after being broken by overly-great pressures. From observation of the shape of the smallest non-wetting bubble saturation required for blockage, we conceived a generalized expression for the critical saturation of the non-wetting fluid that is required for flow

blockage. The pressure required for failure of the numerical seal agrees with the analytical expression used to interpret laboratory experiments of capillary sealing.

The success of the Lattice Boltzmann Method in simulating immiscible fluid flow precipitated numerical simulations of the velocity-dependent dynamic contact angle relationship observed in a Hele Shaw cells. Comparing our data to three published relationships we found that the Hoffman Tanner law provides by far the best velocity-dynamic contact angle relationship. LBM allowed us to investigated the affect wettability on the dynamic contact angle, a factor overlooked in the published relationships, and a factor difficult to separate experimentally or theoretically from interfacial tension. We found that the wettability directly affects the dynamic contact angle in a manner that is consistent by changing the static contact angle and the coefficient of the velocity-dependent term. The stronger the wettability, the smaller the static contact angle, and the greater the fluid momentum required to reverse the direction of curvature of the interface. Both wettability and surface tension affected the value of the correlation coefficient in the Hoffman Tanner law. This is a new insight that may explain why so many different values of the Hoffman Tanner coefficients have been quoted in the literature.

Throughout our studies, but more particular during the study of the capillary seals, we came across many numerical issues. These issues are detailed at length in Chapter 2 of this dissertation, but the main points are summarized here. We found sensitive instabilities in the Shan Chen method of immiscibility as originally implemented. Through application of several stabilizing schemes, we managed to reduce the sensitivity of the instabilities, but not completely remove them. This meant that we were only able to apply a certain range of surface tensions and wettabilities to our fluids. Particle density anomalies arose on the corners of the solid surface, which

were able to reduce but not eliminate. Finer grids and a higher boundary condition tuning at corners of the solid surface could alleviate these anomalies. Areas of intense momentum capped the interfaces of the non-wetting phase. These were found to be an artifact of when the momentum was viewed in the LBM scheme, and therefore an artificial numerical effect that did not affect our conclusions and could be ignored. Momentum banding on the node scale observed during the blockage simulations is the example of a numerical issue with an, as yet, unknown cause. However, it appears to be numerical in nature and sensible results are obtained if the momentum mean is taken.

We were also made aware of a core complaint [2,3] of The Shan-Chen method of immiscibility has been criticized [2,3] for being a phenomenological rather than a natural (or physical) consequence of the fluid's non-ideal equation of state. This criticism in certainly well founded to at least some extent. For example, in the Shan Chen method each fluid is treated as an ideal gas, where immiscibility is enforced through an external force based upon the local density gradients of each fluid. In our simulations of a non-wetting bubble blocking a pore, the non-wetting fluid pressures were greater that those in the wetting fluid by an amount just equal to the capillary pressure. However, the increased pressure of the non-wetting fluid necessarily meant that it also had an increased particle density. This is not physically realistic. A gas should have a density less not greater than a fluid. However, as argued by Shan and Chen [4], the exact nature of the fluids involved may not be important as long as the forces felt by those fluids at phase interfaces. The LBM method may be addressing the most fundamental aspects of the physics.

The fundamental versus phenomenological argument is one that is likely to continue. What can be said from the work reported here is that regardless of how this debate is resolved, the LBM method appears to be useful. We learned, or appear to

have learned, things about capillary blockage and the dynamics of wetting angles that are useful and insightful. This may mean that the LBM method probes fundamental aspects of multiphase physics; it certainly means the method is useful.

# REFERENCES

1. Erendi, A., *Computer Simulations of Geological Processes*, in Department of Geological Sciences. 2000, Cornell University: Ithaca.

2. Swift M., Osborn W.R., and Yeomans J. M., *Lattice Boltzmann Simulation of Nonideal Fluids.* Phys. Rev. Lett., 1995. 75(5): p. 830-833.

3. Swift M., et al., *Lattice Boltzmann Simulation of Liquid Gas and Binary Fluid Systems.* Phys. Rev. E., 1996. 54(5): p. 5041-5052.

4. Shan X. and Chen H., *Lattice Boltzmann Model for Simulating Flows with Multiple Phases and Components.* Phys. Rev E., 1993. 47: p. 1815-1819.

# APPENDIX A: THE SAFFMAN TAYLOR INSTABILTIY

The methods initially developed to model fluid flow in the vadose zone assumed a uniform wetting front separating the invading fluid from the fluid being displaced. However observations indicated the presence of preferential flow pathways along which the transport of the wetting fluid through the vadose zone was more rapid. Two types of preferential pathways have been identified. The first occurs through macropores and fractures. This has been extensively studied [1-4]. Evidence suggested preferential pathways also exist in soils without macropores and fractures. This evidence includes discrepancies between uniform front models and actual field observations [5], rapid changes in the water level and chemistry in an aquifer shortly after a rainfall in uniform and unfractured soils [6], recharge even when the evapo-transpriation rate is high [7], and large lateral variations in the moisture content. This last piece of evidence lead to the conclusion that the wetting fluid was channeled into certain regions of the subsurface [8 -12].

In the late 1950's Saffman and Taylor [13] and Chuoke [14] described the theoretical underpinnings of what came to be known as the Saffman-Taylor or fingering instabilities. There are two types of fingering instability:

1. Gravity fingers, where a more dense fluid descends into a porous media containing a less dense fluid.

2. Viscous fingers, where a less viscous fluid is inserted into a more viscous fluid.

As their names suggest, the instabilities take on the form of fingers penetrating into a less dense/more viscous fluid. The actual form of the fingers depends on the exact value of the fluid parameters. Fluid parameters which can affect the form and extent of fingering are [15, 16]: the wetting properties, contact angles between the

invading and displaced fluid, relative viscosities and densities of the two fluids, permeability of the medium. It should be noted that while this list was constructed for viscous fingering, the same fluid parameters also apply to gravity fingers.

Laboratory and field experiments have been conducted to explore the relationship between some of these parameters and the fingering process. A number of authors [17 -21] have shown that there is a qualitative difference in viscous fingering depending on the wettability of soil by the invading fluid. In the case where the invading fluid wets the medium, the fingers spread rapidly enough that the invasion front can be described on a macroscopic scale. If the invading fluid does not wet the medium, the fingering occurs on the pore scale. The fingering then has a percolation character where a main finger acts as a backbone.

Laboratory experiments have shown that for viscous fingers, the lateral dimension of the fingers become smaller as the velocity or viscosity of the displaced fluid increases. From the results of numerous laboratory studies [11, 22, 23] of gravity fingers, it may be concluded [24] that the maximum finger diameter that can develop decreases with increasing grain size, and that for any given flow rate, coarse grained sands will produce fewer and more widely spaced fingers. Silio and Tellam [24] carried out experiments on gravity fingers in the field. They found that stratification promotes the fingering process and also that once fingers have formed they may persist in the same location for such a long time that they can be considered permanent features. Another conclusion was that fingers are broader and less distinct in moist sands.

Saffman and Taylor [13] used Darcy's law and the balance between density and viscous forces to understand when instabilities may occur. Darcy's law states that the pressure gradient in a fluid is the sum of gravitational body forces and viscous resistance to fluid movement:

$$\frac{dp}{dx} = -\frac{\mu u}{k} + \rho g \qquad \ldots(A.1)$$

Where $p$ = pressure, $u$ = velocity of the fluid, $\mu$ = viscosity, $k$ = permeability of the substrate, $\rho$ = density and $g$ = gravitational acceleration (pointing downwards).

We can use Darcy's law to find the difference in the pressure at a point due to the interface between two fluids:

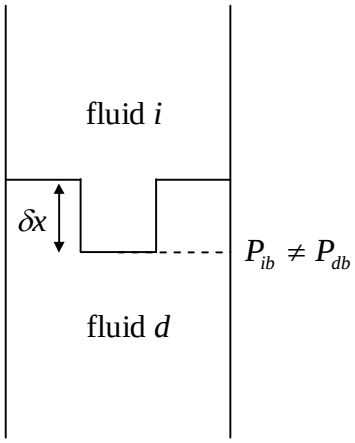


Figure A.1: Idealized finger development

In Figure 1.4, for example, "*i*" refers to the invading fluid and "*d*" the displaced fluid, $P_{it}$ is the pressure of the invading fluid at the top of the finger, $P_{ib}$ is the pressure of the invading fluid at the bottom of the finger, $P_{dt}$ is the pressure of the

displaced fluid at the top of the finger and $P_{db}$ is the pressure of the displaced fluid at the bottom of the finger  The pressure of both fluids is the same at the top of the finger and is different at the bottom of the finger.  Assuming the soil permeability is uniform, we obtain the pressure gradient within the finger:

$$\frac{dp}{dx} = \frac{P_{ib} - P_t}{\delta x} = -\frac{\mu_i u}{k} + \rho_i g \,, \qquad \ldots(A.2)$$

Therefore the pressure at the bottom of the finger is:

$$P_{1b} = \left[ -\frac{\mu_i u}{k} + \rho_i g \right] \delta x + P_t \,. \qquad \ldots(A.3)$$

Similarly we obtain the pressure of the displaced fluid at the bottom of the finger:

$$P_{db} = \left[ -\frac{\mu_d u}{k} + \rho_d g \right] \delta x + P_t \,. \qquad \ldots(A.4)$$

Note that we assume the entire interface between *i* and *d* moves downward with the same constant velocity, u.  The box in Figure 1.4 is just a small irregularity in the interface.  If $P_{ib} > P_{db}$, then the bottom of the finger would be pushed further into the invading fluid, and a positive feedback mechanism that is the predecessor of instability would be created [14].

$$\left[ -\frac{\mu_i u}{k} + \rho_i g \right] \delta x + P_t > \left[ -\frac{\mu_d u}{k} + \rho_d g \right] \delta x + P_t \qquad \ldots(A.5)$$

After a little algebra:

$$\frac{u}{k}(\mu_d - \mu_i) + g(\rho_i - \rho_d) > 0 \qquad \ldots(A.6)$$

From Eq. 1.6 we see that instabilities could occur if the viscosity of the displaced fluid is greater than that of the invading fluid and/or if the density of the invading fluid is greater than the displaced fluid. This relation also predicts a possible interplay between the viscosity and density. For example, if the invading fluid is denser than the displaced fluid, instability may not occur if this invading fluid is also more viscous than the displaced fluid. This interplay between gravitational viscous factors was put into a table by Glass and Nicholl [25] and is reproduced here in Table 5.1.

Interfacial tension at curved fluid-fluid interface produces a pressure jump between the two fluids that is defined by Laplace's law:

$$P_c = \frac{2\sigma}{r}, \qquad \ldots(A.7)$$

Where $P_c$ is the capillary pressure, r is the radius of curvature and $\sigma$ is the interfacial tension between the two fluids.

In the case of fingering, the capillary pressure acts to stabilize the finger, as long as an incipient finger moving downward has a concave upward interface. Approximately six months after Saffman and Taylor's original paper [13], Chuoke [14] added capillary pressure to the instability analysis.

He found that until a finger reaches a critical length, capillary forces stabilize the interface. Chuoke et. al. adjusted Eq. 1.6, such that instabilities occur if:

$$\frac{u}{k}(\mu_d - \mu_i) + g(\rho_i - \rho_d) - \sigma^* \alpha^2 > 0, \qquad \ldots(A.8)$$

where $\alpha$ describes interfacial deformation, where $\alpha \approx 1$[26], $\sigma^* = \sigma(dA^*/dA)$ is the effective interfacial tension in a porous media, compared to $\sigma$, the ordinary interfacial tension in a Hele Shaw cell. A is the total area of all microscopic moving fluid-fluid interfaces in the soil and A* is the interfacial area in a Hele Shaw cell. As fluid-fluid interfaces in porous media are rarely flat, Chuoke et. al. estimated the interfacial tension for porous media from Hele-Shaw cell data.

Table A.1: Interplay between the viscous and gravitation stabilizing forces; reproduced from Glass and Nicholl [25]

| | Gravity Stabilized | Gravity destabilized |
|---|---|---|
| Viscous stabilized | Type I: unconditionally stable fluid accelerated downwards into more dense, less viscous fluid (and vice versa) | Type II: conditionally unstable. Fluid accelerated downwards into a less dense, less viscous fluid |
| Viscous destabilized | Type III: conditionally unstable fluid accelerated downwards into more dense, more viscous fluid (and vice versa) | Type II: unconditionally unstable. Fluid accelerated downwards into a more dense, more viscous fluid |

Parlange and Hill [27] suggested adjusting the local velocity to include changes caused by the curved interface:

$$u = u_o - \frac{\Lambda}{r}, \qquad \ldots(A.9)$$

where $u_o$ is the velocity as measured in a Hele Shaw cell, r is the radius of curvature and $\Lambda = S^2 / 2(\theta_f - \theta_i)^2$, which is related to the capillary imbibition rate of the medium [28], S is the sorpivity, which is the measure of the capacity of a medium to absorb or desorb fluid by capillarity, and $\theta_i$ and $\theta_f$ are the initial and final volumetric water contents respectively. Both of these approaches have assumed that the wetting angle is constant (not dependant on interface velocity). However, it has been shown the capillary pressure is a dynamic parameter. Wetiz et. al. performed experiments which resulted in an empirical relationship between capillary pressure and fluid velocity, which shows that $P_c$ scales as :

$$P_c \approx \frac{\sigma}{r}\left(-1 + c\left[\frac{u\nu}{\sigma}\right]^x\right), \qquad \ldots(A.10)$$

where c and x are both constants which the authors fitted to experimental data. In Eq. A.10, u is the fluid velocity and $\nu$ the fluid viscosity. Weitz et. al. found that x =0.5, such that the final relationship between $P_c$ and u is:

$$P_c \propto u^{\frac{1}{2}} \qquad \ldots(A.11)$$

This is different from the relationship determined by other authors [29, 30] that has because known at the Hoffman-Tanner law. It states that relationship between the wetting angle and the fluid velocity is:

$$\theta = c_{HT}\left(\frac{u\nu}{\sigma}\right)^{\frac{1}{3}}, \qquad \ldots(A.12)$$

where $\theta$ is the wetting angle and $c_{HT}$ is a constant. The Hoffman tanner law may be expressed to highlight the relationship between the capillary pressure and the fluid velocity: $P_c \propto u^{\frac{1}{3}}$.

Dicarlo and Blunt [31] extended this analysis for porous media, adding in a term representing pore entry pressure. They suggested that pore-scale variations are important at low velocities and accounting for the branched nature of fingers, but pore scale variation is unimportant at high interface velocities, where a single backbone finger forms.

This review illustrates how the wetting angle between fluid fluids affects fingering, and suggests how a dynamic dependence of wetting angle on the interface velocity could be important. This provides background for our discussion in Chapter 4 of this thesis.

# REFERENCES


1. Beven, K. and P. Germann, *Macropores and Water-Flow in Soils.* Water Resources Research, 1982. 18(5): p. 1311-1325.

2. Germann, P. and K. Beven, *Kinematic Wave Approximation to Infiltration into Soils with Sorbing Macropores.* Water Resources Research, 1985. 21(7): p. 990-996.

3. Davidson, M.R., *Numerical-Calculation of Saturated-Unsaturated Infiltration in a Cracked Soil.* Water Resources Research, 1985. 21(5): p. 709-714.

4. Bronswijk, J.J.B., *Modelling of Water-Balance, Cracking and Subsidence of Clay Soils.* Journal of Hydrology, 1988. 97(3-4): p. 199-212.

5. Jury, W.A. and H. Fluhler, *Transport of Chemicals Through Soil - Mechanisms, Models and Field Applications.* Advances in Agronomy, 1992. 47: p. 141-201.

6. Steenhuis, T.S., C.J. Ritsema, and L.W. Dekker, *Fingered Flow in Unsaturated Soil: From Nature to Model - Introduction.* Geoderma, 1996. 70(2-4): p. 83-85.

7. Beekman, H.E., A. Gieske, and E.T. Selaolo. *Groundwater Recharge Studies in Botswana (1987-1997): A Critical Review.* in *DWAF/WRC Workshop on Recharge*. 1996. Warmsbaths, South Africa.

8. Starr, J.L., et al., *Leaching Characteristics of a Layered Field Soil.* Soil Science Society of America Journal, 1978. 42: p. 376-391.

9. Starr, J.L., J.Y. Parlange, and C.R. Frink, *Water and Chloride Movement Through a Layered Field Soil.* Soil Science Society of America Journal, 1986. 50(6): p. 1384-1390.

10. Allison, G.B., G.W. Gee, and S.W. Tyler, *Vadose-Zone Techniques for Estimating Groundwater Recharge in Arid and Semiarid Regions.* Soil Science Society of America Journal, 1994. 58(1): p. 6-14.

11. Glass, R.J., T.S. Steenhuis, and J.Y. Parlange, *Wetting Front Instability as a Rapid and Far Reaching Hydrologic Process in the Vadose Zone.* Journal of Contaminant Hydrology, 1988. 3: p. 207-226.

12. van Ommen, H.C., et al., *A New Technique for Evaluating the Presence of Preferential Flow Paths in Nonstructured Soils.* Soil Science Society of America Journal, 1988. 52(4): p. 1192-1193.

13. Saffman, P.G. and G. Taylor, *The Penetration of a Fluid into a Porous Medium or Hele-Shaw Cell Containing a More Viscous Liquid.* Proceedings of the Royal Society of London Series a-Mathematical and Physical Sciences, 1958. 245(1242): p. 312-&.

14. Chuoke, R.L., P. van Meurs, and C. van der Poel, *The Instability of Slow, Immiscible, Viscous Liquid-Liquid Displacements in Permeable Media.* Transactions of the American Institute of Mining and Mettallurgical Engineers, 1959. 216: p. 188-194.

15. Homsy, G.M., *Viscous Fingering In Porous Media.* Annual Reviews in Fluid Mechanics, 1987. 19: p. 271-311.

16. Wooding, R.A. and H.J. Morelseytoux, *Multifluid Fluid-Flow through Porous-Media.* Annual Review of Fluid Mechanics, 1976. 8: p. 233-274.

17. Peters, E.J. and D.L. Flock, *The Onset of Instability During 2-Fluid Immiscible Displacement in Porous-Media.* Society of Petroleum Engineers Journal, 1981. 21(2): p. 249-258.

18. Paterson, L., V. Hornof, and G. Neale, *Water Fingering into an Oil-Wet Porous-Medium Saturated with Oil at Connate Water Saturation.* Revue De L Institut Francais Du Petrole, 1984. 39(4): p. 517-&.

19. Paterson, L., V. Hornof, and G. Neale, *Visualization of a Surfactant Flood of an Oil-Saturated Porous-Medium.* Society of Petroleum Engineers Journal, 1984. 24(3): p. 325-327.

20. White, I., P.M. Colombera, and J.R. Philip, *Experimental-Study of Wetting Front Instability Induced by Sudden Change of Pressure-Gradient.* Soil Science Society of America Journal, 1976. 40(6): p. 824-829.

21. Maloy, K.J., J. Feder, and T. Jossang, *Viscous Fingering Fractals in Porous-Media.* Physical Review Letters, 1985. 55(24): p. 2688-2691.

22. Diment, G.A. and K.K. Watson, *Stability Analysis of Water-Movement in Unsaturated Porous Media. 3. Experimental Studies.* Water Resources Research, 1985. 21(7): p. 979-984.

23. Tamai, N., T. Asaeda, and C.G. Jeevaraj, *Fingering in Two-Dimensional, Homogeneous, Unsaturated Porous-Media.* Soil Science, 1987. 144(2): p. 107-112.

24. Sililo, O.T.N. and J.H. Tellam, *Fingering in Unsaturated Zone Fow: A Qualitative Review with Laboratory Experiments on Heterogeneous Systems.* Ground Water, 2000. 38(6): p. 864-871.

25. Glass, R.J. and M.J. Nicholl, *Physics of Gravity Fingering of Immiscible Fluids within Porous Media: An Overview of Current Understanding and Selected Complicating Factors.* GEODERMA, 1996. 70(2-4): p. 133-163.

26. Stokes, J.P., A.P. Kushnick, and M.O. Robbins, *Interface Dynamics in Porous Media: A Random Field Description.* Physical Review Letters, 1988. 60: p. 1386-1389.

27. Parlange, J.Y. and S. Hill, *Theoretical Analysis of Wetting Front Instability in Soils.* Soil Science, 1976. 122(4): p. 236-239.

28. Glass, R.J., J.Y. Parlange, and T.S. Steenhuis, *Immiscible Displacement in Porous Media. Stability Analysis of 3-Dimensional, Axisymmetrical Disturbances with Application to Gravity-Driven Wetting Front Instability.* Water Resources Research, 1991. 27(8): p. 1947-1956.

29. Hoffman, R.L., *Study of Advancing Interface. 1. Interface Shape in Liquid-Gas Systems.* Journal of Colloid and Interface Science, 1975. 50(2): p. 228-241.

30. Tanner, L.H., *Spreading of Silicone Oil Drops on Horizontal Surfaces.* Journal of Physics D - Applied Physics, 1979. 12(9): p. 1473.

31. DiCarlo, D.A. and M.J. Blunt, *Determination of Finger Shape using Dynamic Capillary Pressure.* Water Resour. Res., 2000. 36(9): p. 2781-2785.

# APPENDIX B: THE AFFECT OF AN INCREASING BODY FORCE ON FLUIDS WITH DIFFERENT INTERACTION PARAMETERS

In this appendix we show the simulation results for different body forces acting on fluids with constant wettability, where $g_{sw}$ = -1 and $g_{sn}$ = -10, with a fluid interaction parameter given by g = -0.9, g = -1.1, g = -1.3, g = -1.4, g =-1.5 and g = -1.6. Each frame shows a cross section through the section of the cell in an identical manner to Figure 4.5. All figures show the wetting fluid density, where the interface is defined as the surface at which the density of the non-wetting fluid is 90% of its highest value. For all values of g, the curvature of the interface changes from concave to convex as the body force is increased. .

We also show the corresponding figures from the investigation of how wettability affects the velocity-dynamic contact angle relationship. In this set of experiments, we use a constant g = -1.3 and $gs_w$ = 1 and vary $gs_n$, so that $gs_n$ = -5, $gs_n$ = -10, $gs_n$ = -15, $gs_n$ = -20 and $gs_n$ = -25.

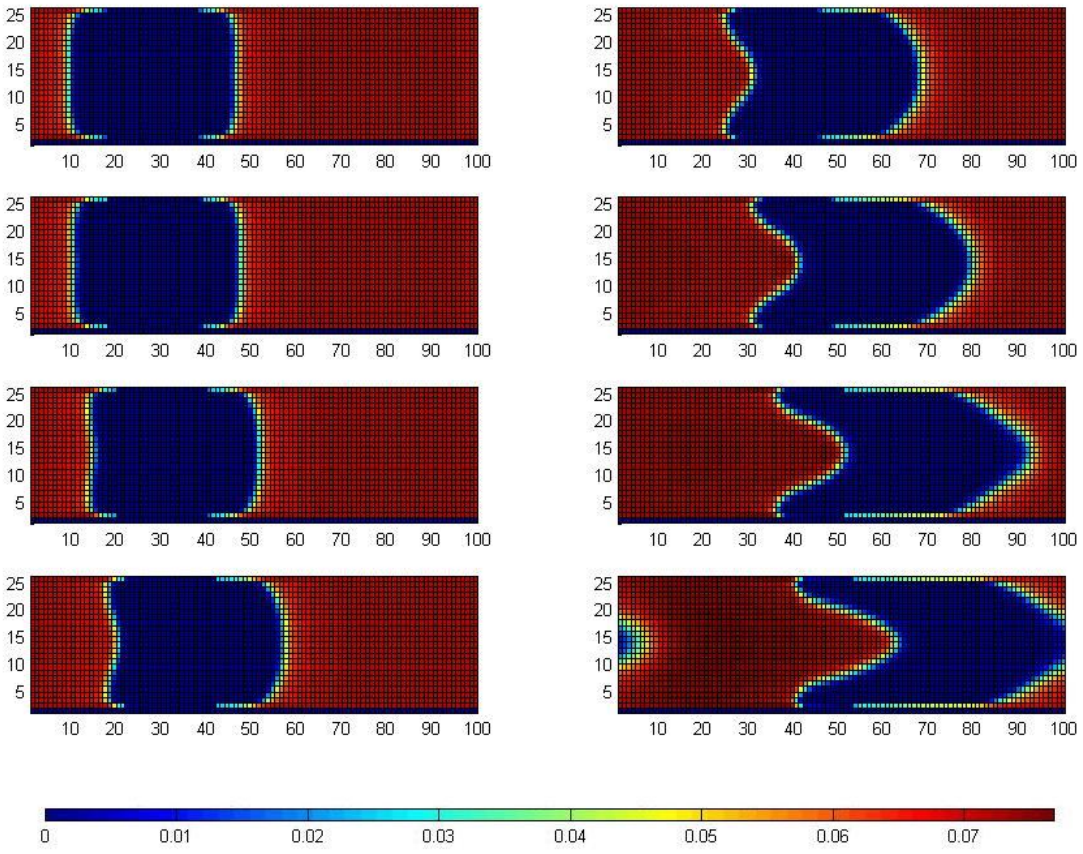


Figure B.1: Simulation results for g =-0.9, $g_{sw}$ =1, $g_{sn}$ =-10.

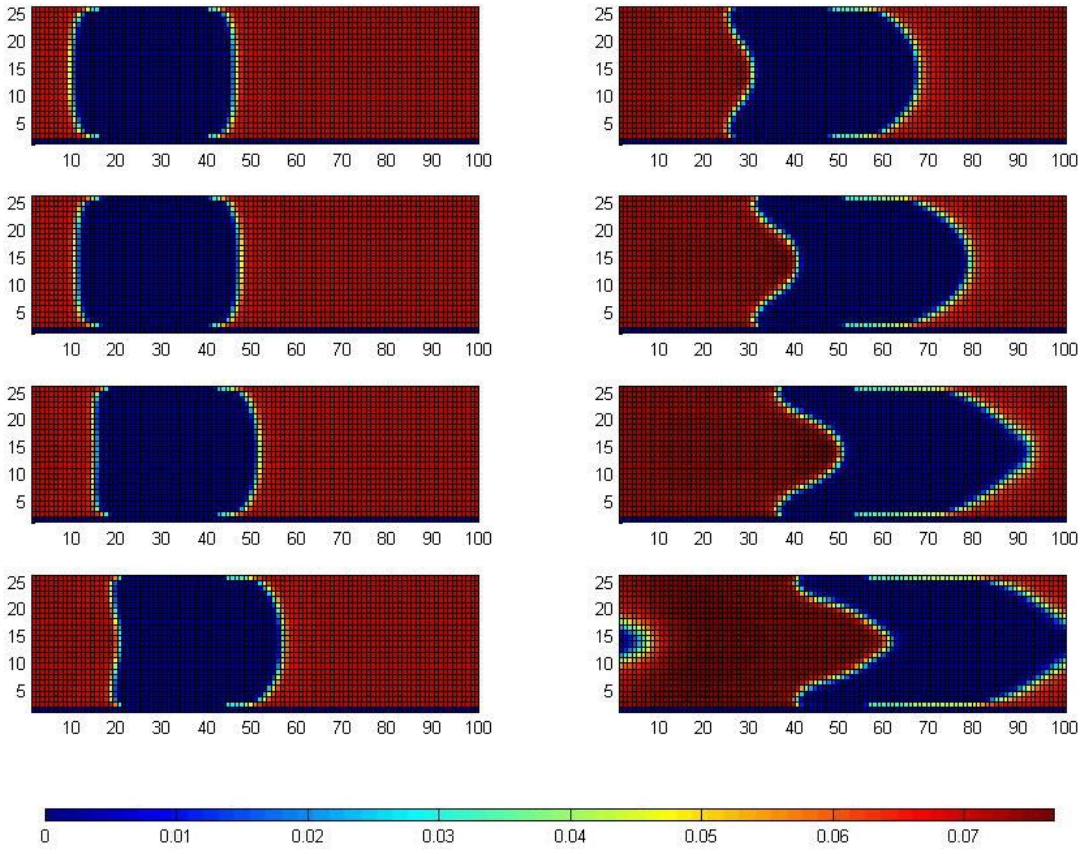


Figure B.2: Simulation results for g =-1.1, $g_{sw}$ =1, $g_{sn}$ =-10.

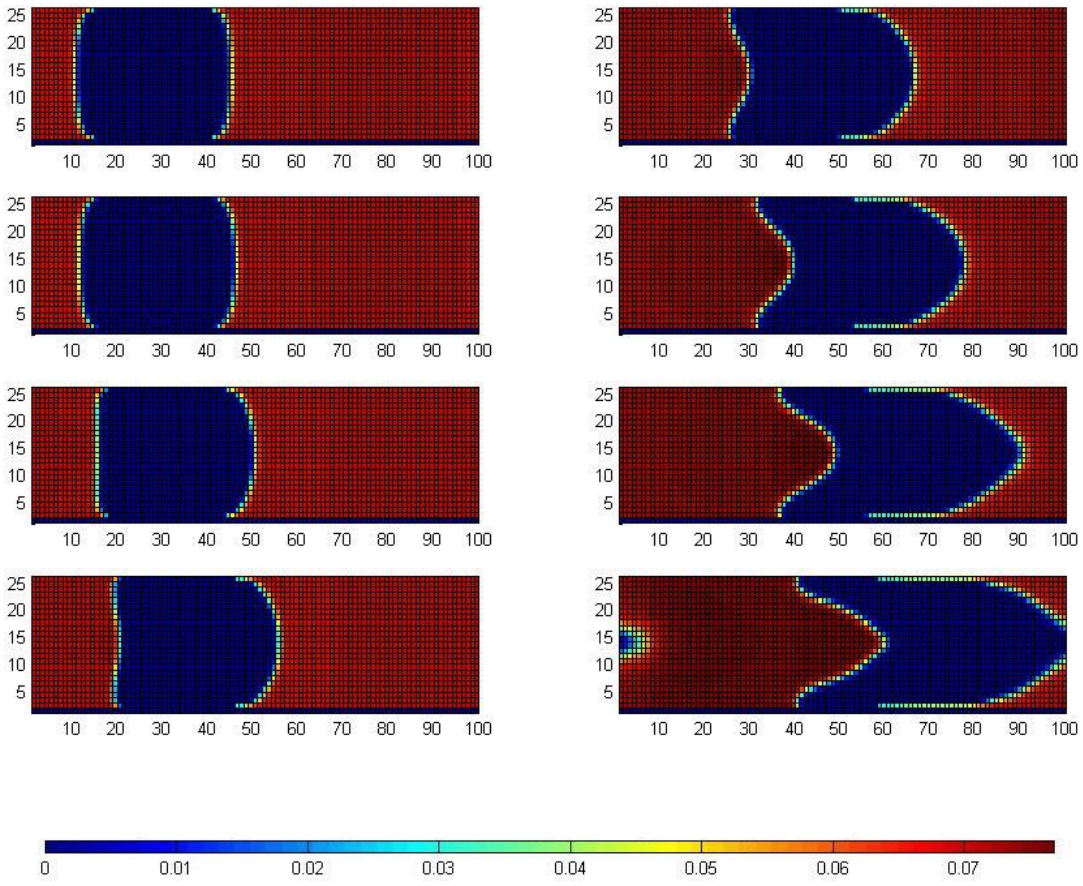


Figure B.3: Simulation results for g =-1.3, $g_{sw}$ =1, $g_{sn}$ =-10.

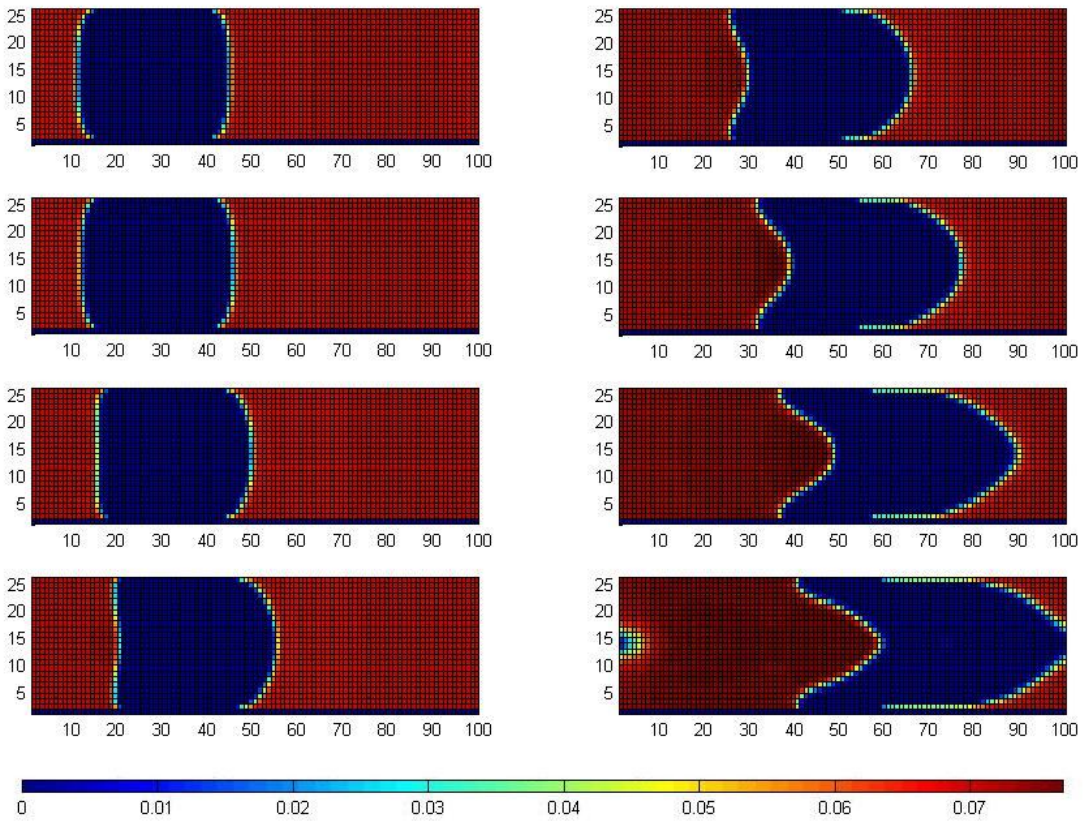


Figure B.4: Simulation results for g =-1.4, $g_{sw}$ =1, $g_{sn}$ =-10.

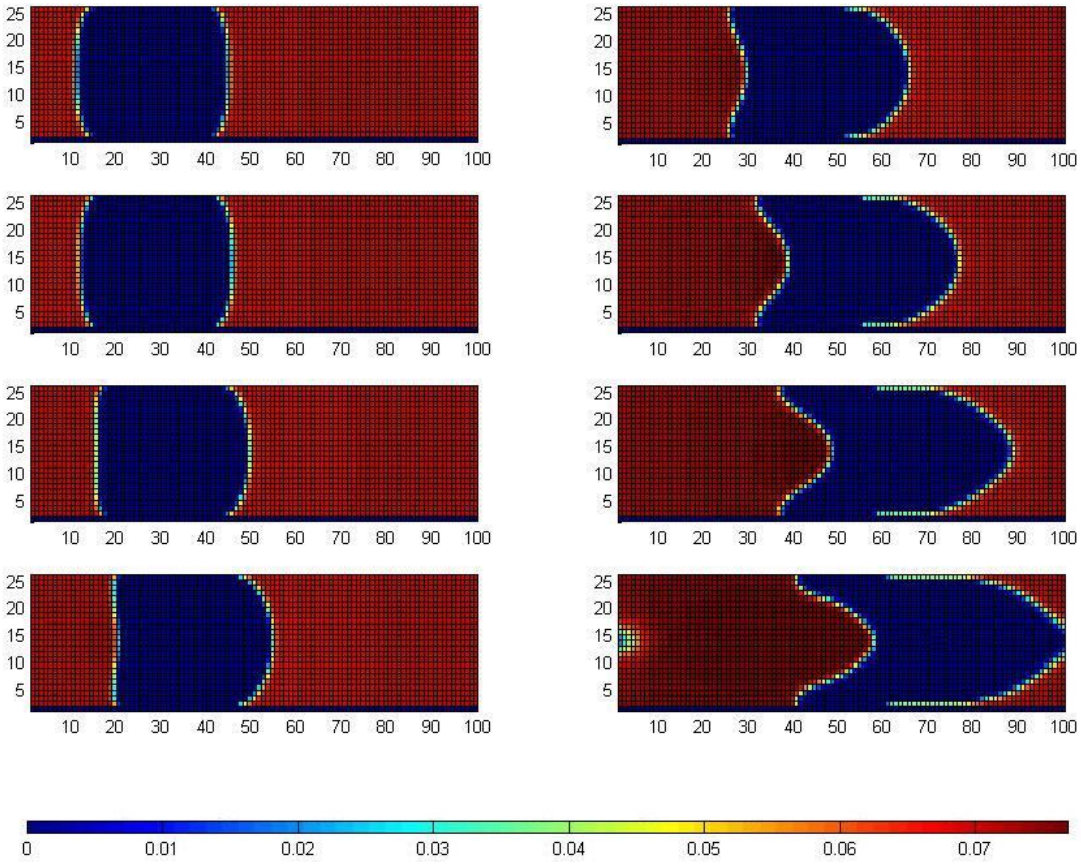


Figure B.5: Simulation results for g =-1.5, $g_{sw}$ =1, $g_{sn}$ =-10.

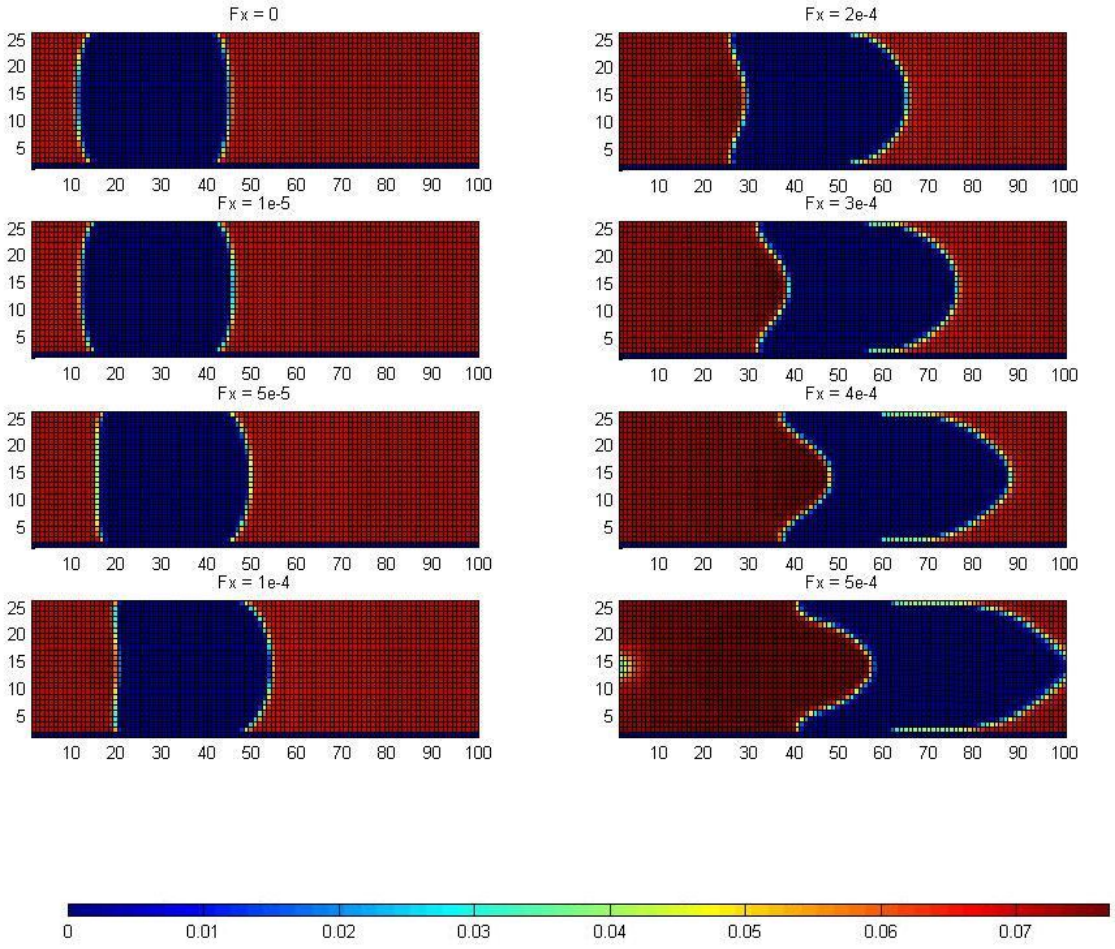


Figure B.6: Simulation results for g =-1.6, $g_{sw}$ =1, $g_{sn}$ =-10.

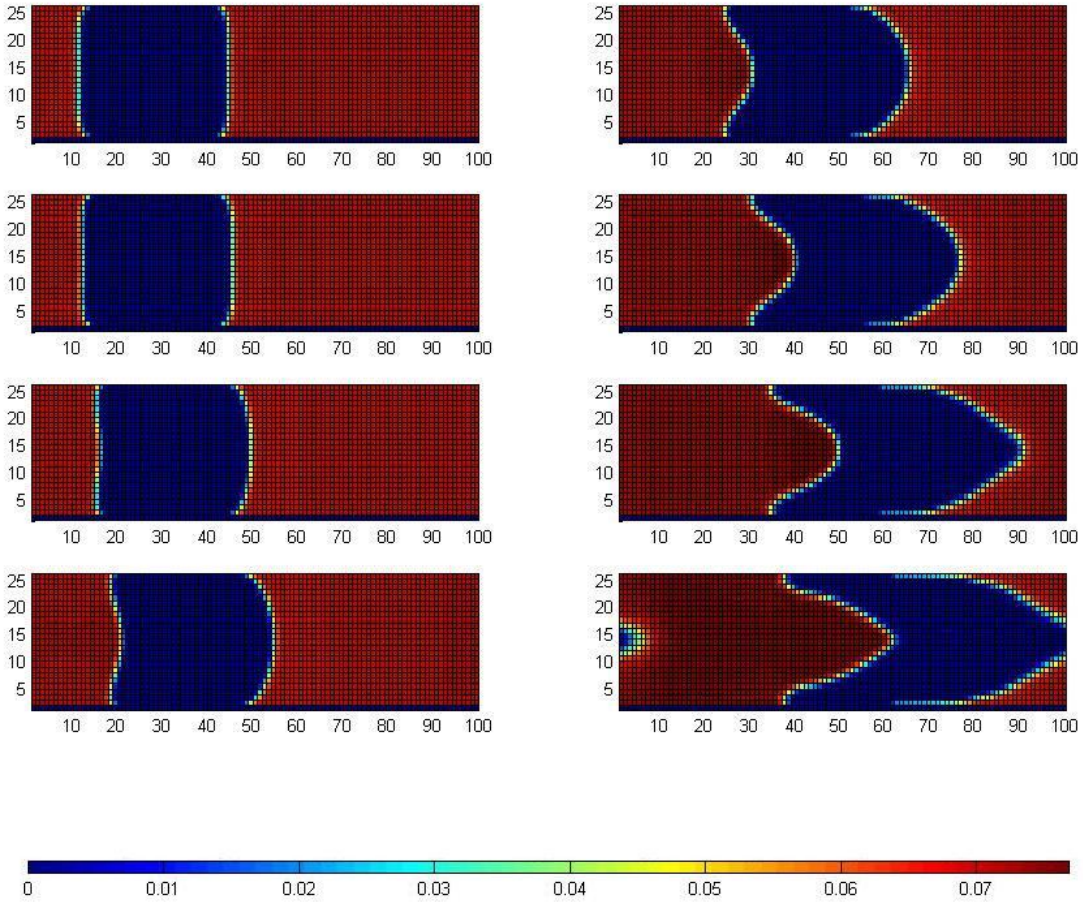


Figure B.7: Simulation results for g =-1.3, $g_{sw}$ =1, $g_{sn}$ =-5.

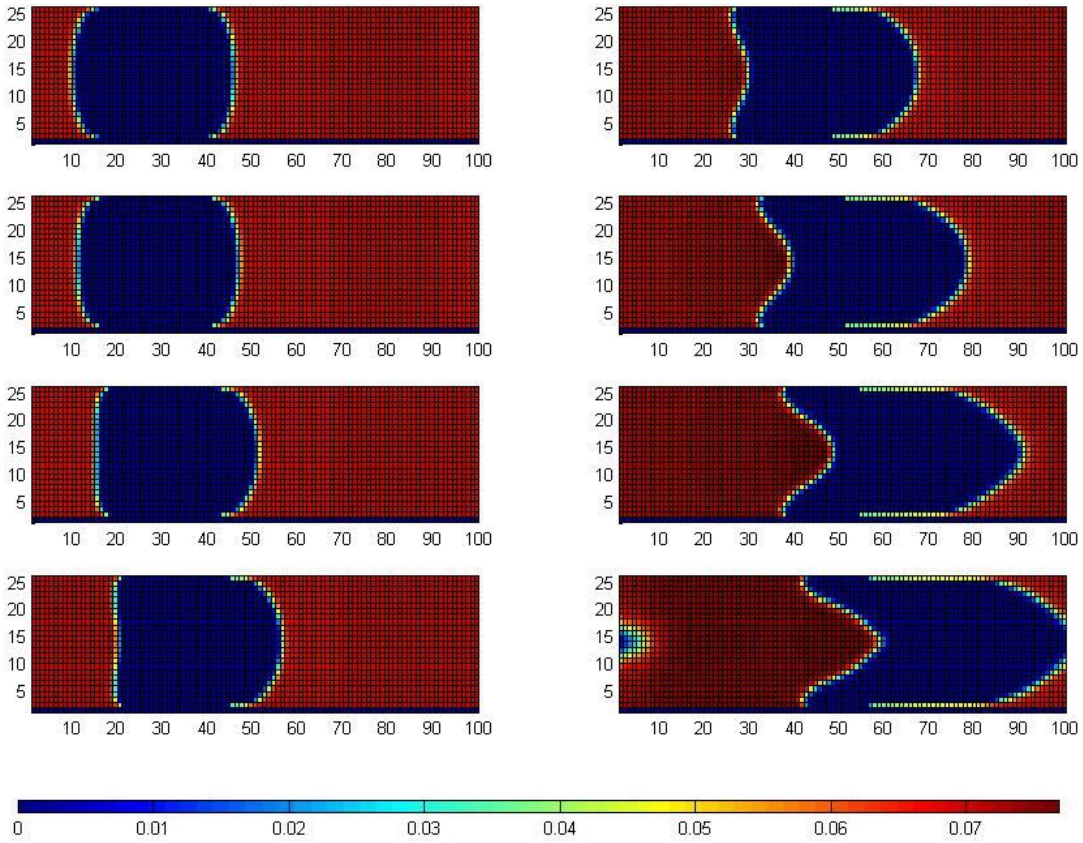


Figure B.8: Simulation results for g =-1.3, $g_{sw}$ =1, $g_{sn}$ =-15.

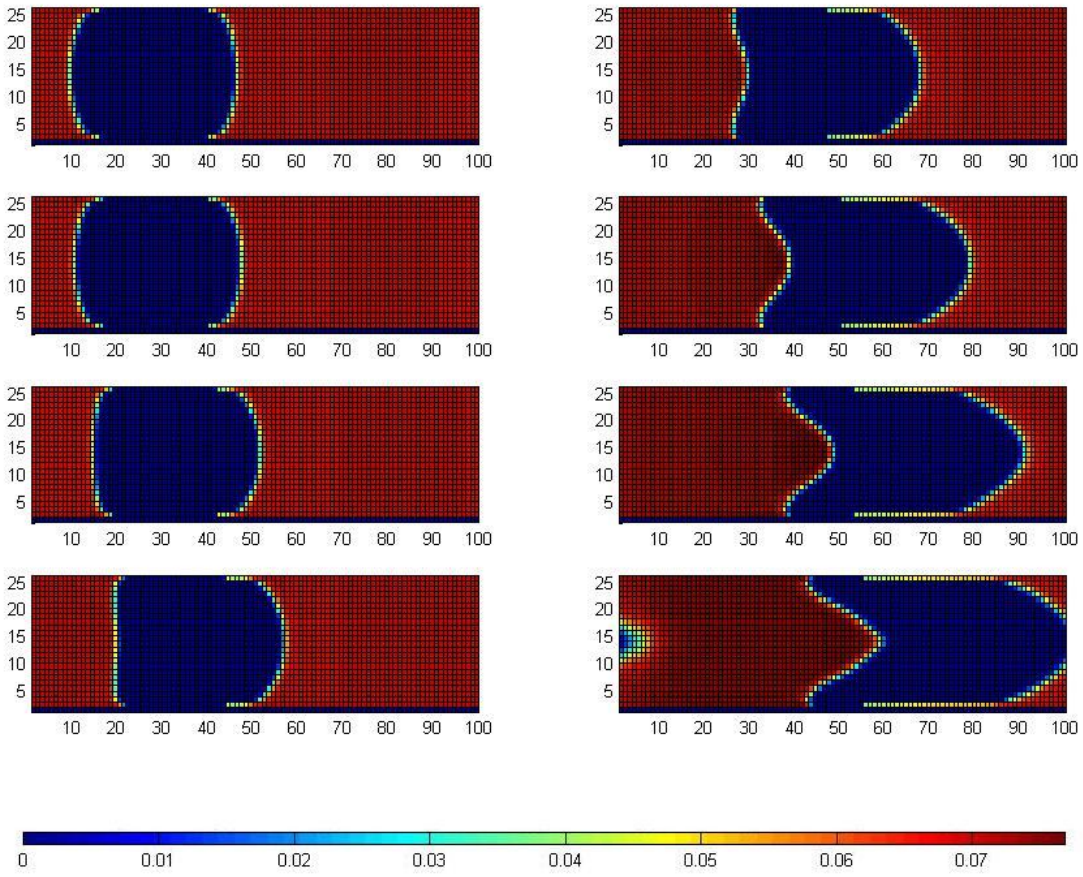


Figure B.9: Simulation results for g =-1.3, $g_{sw}$ =1, $g_{sn}$ =-20.

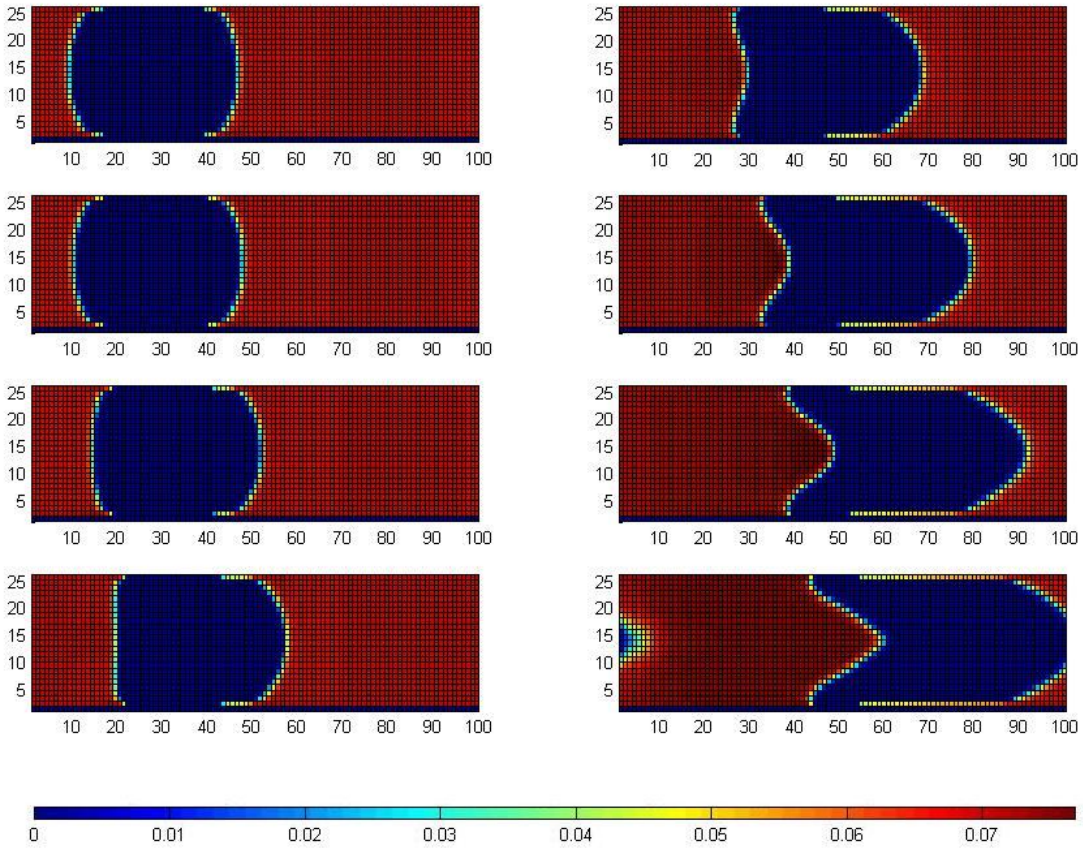


Figure B.10: Simulation results for g =-1.3, $g_{sw}$ =1, $g_{sn}$ =-25.

# APPENDIX C: RESULTS FROM THE LAPLACE TESTS DESIGNED TO CALCULATE SURFACE TENSION

Table C.1: Table of results of the Laplace test when g = -0.8, $g_{ww}$= $g_{nn}$ = 0

| $S_{nw}$ | $r_w$ | $r_{nw}$ | $\rho_w$ | $\rho_n$ | $\Delta\rho$ | 1/r | $\Delta P$ |
|---|---|---|---|---|---|---|---|
| 21.74% | 10.0469 | 6.9792 | 0.0917 | 0.0993 | 0.0076 | 0.1175 | 0.0025 |
| 23.21% | 10.3942 | 7.2192 | 0.0922 | 0.0995 | 0.0074 | 0.1135 | 0.0025 |
| 24.67% | 10.6248 | 7.4785 | 0.0926 | 0.1003 | 0.0077 | 0.1105 | 0.0026 |
| 26.10% | 10.8403 | 7.7529 | 0.0931 | 0.1004 | 0.0074 | 0.1076 | 0.0025 |

Where $r_n$, $r_w$, $r_{avg}$ are the estimate of the radius from the non-wetting fluid and the wetting fluid respectively, and $r_{avg}$ = ½($r_w$+$r_n$). All radii are given in lattice lengths. $\rho_w$ and $\rho_n$ are the wetting fluid density and the non-wetting fluids density respectively, $\Delta\rho$ is the density differences $\Delta P$ is the pressure difference, given in lattice pressure units.

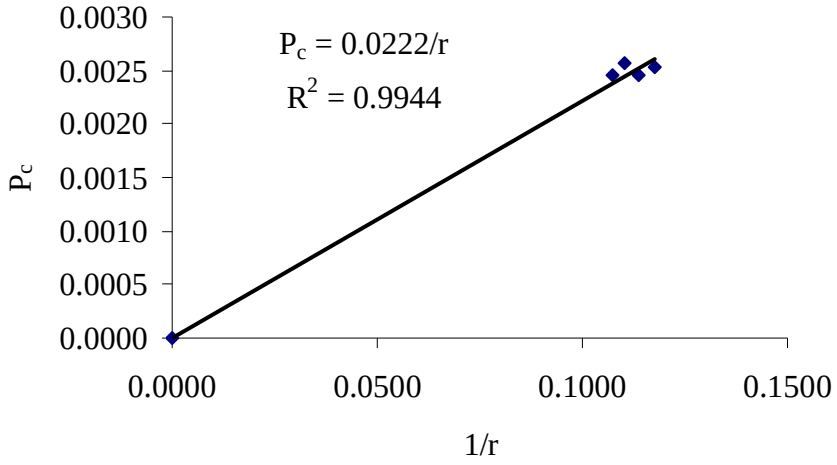


Fig C.1: Pc against 1/r where r = radius of the non-wetting sphere from the Laplace test when g = -0.8, $g_{ww}$ = $g_{nn}$ =0.

Table C.2: Table of results of the Laplace test when g = -0.85, $g_{ww}$= $g_{nn}$ = 0

| $S_{nw}$ | $r_w$ | $r_{nw}$ | $\rho_w$ | $\rho_n$ | $\Delta\rho$ | 1/r | $\Delta P$ |
|---|---|---|---|---|---|---|---|
| 18.70% | 9.6941 | 6.6214 | 0.0911 | 0.0989 | 0.0078 | 0.1226 | 0.0026 |
| 20.23% | 9.9642 | 6.9265 | 0.0915 | 0.0989 | 0.0074 | 0.1184 | 0.0025 |
| 21.74% | 10.3409 | 7.1201 | 0.0919 | 0.0998 | 0.0078 | 0.1145 | 0.0026 |
| 23.21% | 10.5452 | 7.4327 | 0.0924 | 0.1000 | 0.0076 | 0.1112 | 0.0025 |
| 24.67% | 10.7749 | 7.7423 | 0.0928 | 0.1003 | 0.0075 | 0.1080 | 0.0025 |
| 26.10% | 10.9263 | 7.9892 | 0.0933 | 0.1002 | 0.0069 | 0.1057 | 0.0023 |

Where $r_n$, $r_w$, $r_{avg}$ are the estimate of the radius from the non-wetting fluid and the wetting fluid respectively, and $r_{avg}$ = ½($r_w$+$r_n$). All radii are given in lattice lengths. $\rho_w$ and $\rho_n$ are the wetting fluid density and the non-wetting fluids density respectively, $\Delta\rho$ is the density differences $\Delta P$ is the pressure difference, given in lattice pressure units.

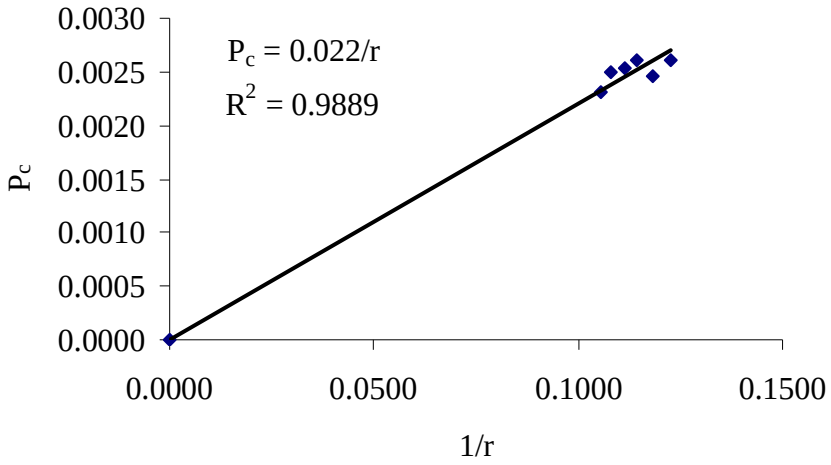


Fig C.2: Pc against 1/r where r = radius of the non-wetting sphere from the Laplace test when g = -0.85, $g_{ww}$ = $g_{nn}$ =0.

Table C.3 Table of results of the Laplace test when g = -0.9, $g_{ww}$= $g_{nn}$ = 0

| $S_{nw}$ | $r_w$ | $r_{nw}$ | $\rho_w$ | $\rho_n$ | $\Delta\rho$ | 1/r | $\Delta P$ |
|---|---|---|---|---|---|---|---|
| 21.74% | 10.4178 | 7.3275 | 0.0921 | 0.0999 | 0.0078 | 0.1127 | 0.0026 |
| 23.21% | 10.6135 | 7.5685 | 0.0926 | 0.1005 | 0.0079 | 0.1100 | 0.0026 |
| 24.67% | 10.8512 | 7.7423 | 0.0930 | 0.1005 | 0.0075 | 0.1076 | 0.0025 |
| 26.10% | 11.0528 | 8.0289 | 0.0934 | 0.1011 | 0.0077 | 0.1048 | 0.0026 |

Where $r_n$, $r_w$, $r_{avg}$ are the estimate of the radius from the non-wetting fluid and the wetting fluid respectively, and $r_{avg}$ = ½($r_w$+$r_n$). All radii are given in lattice lengths. $\rho_w$ and $\rho_n$ are the wetting fluid density and the non-wetting fluids density respectively, $\Delta\rho$ is the density differences $\Delta P$ is the pressure difference, given in lattice pressure units.

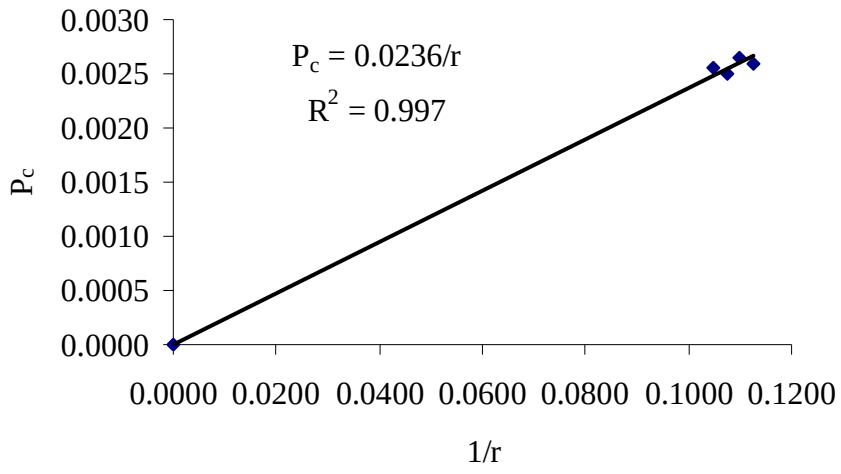


Fig C.3: Pc against 1/r where r = radius of the non-wetting sphere from the Laplace test when g = -0.9, $g_{ww}$ = $g_{nn}$ =0.

Table C.4: Table of results of the Laplace test when g = -0.95, $g_{ww}$= $g_{nn}$ = 0

| $S_{nw}$ | $r_w$ | $r_{nw}$ | $\rho_w$ | $\rho_n$ | $\Delta\rho$ | 1/r | $\Delta P$ |
|---|---|---|---|---|---|---|---|
| 18.70% | 9.9770 | 6.8050 | 0.0914 | 0.1006 | 0.0092 | 0.1192 | 0.0031 |
| 20.23% | 10.1960 | 7.1576 | 0.0918 | 0.0999 | 0.0081 | 0.1152 | 0.0027 |
| 21.74% | 10.4353 | 7.4671 | 0.0922 | 0.1002 | 0.0080 | 0.1117 | 0.0027 |
| 23.21% | 10.7087 | 7.6346 | 0.0926 | 0.1009 | 0.0083 | 0.1090 | 0.0028 |
| 24.67% | 10.9210 | 7.8780 | 0.0931 | 0.1012 | 0.0082 | 0.1064 | 0.0027 |
| 26.10% | 11.0892 | 8.1265 | 0.0935 | 0.1010 | 0.0076 | 0.1041 | 0.0025 |

Where $r_n$, $r_w$, $r_{avg}$ are the estimate of the radius from the non-wetting fluid and the wetting fluid respectively, and $r_{avg}$ = ½($r_w$+$r_n$). All radii are given in lattice lengths. $\rho_w$ and $\rho_n$ are the wetting fluid density and the non-wetting fluids density respectively, $\Delta\rho$ is the density differences $\Delta P$ is the pressure difference, given in lattice pressure units.

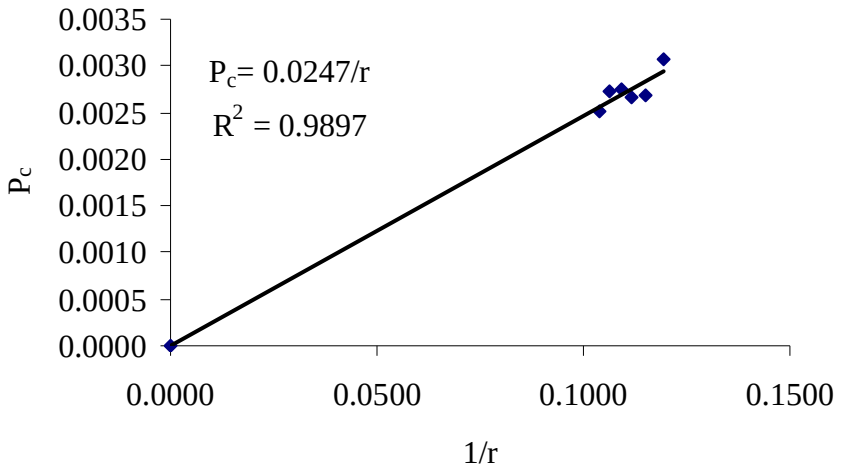


Fig C.4: Pc against 1/r where r = radius of the non-wetting sphere from the Laplace test when g = -0.95, $g_{ww}$ = $g_{nn}$ =0.

Table C.5: Table of results of the Laplace test when g = -1.0, $g_{ww}$= $g_{nn}$ = 0

| $S_{nw}$ | $r_w$ | $r_{nw}$ | $\rho_w$ | $\rho_n$ | $\Delta\rho$ | 1/r | $\Delta P$ |
|---|---|---|---|---|---|---|---|
| 18.70% | 10.0595 | 6.8596 | 0.0914 | 0.1012 | 0.2364 | 0.1182 | 0.0033 |
| 20.23% | 10.2811 | 7.2677 | 0.0919 | 0.1003 | 0.2279 | 0.1140 | 0.0028 |
| 21.74% | 10.5050 | 7.4442 | 0.0923 | 0.1013 | 0.2229 | 0.1114 | 0.0030 |
| 23.21% | 10.7143 | 7.7317 | 0.0927 | 0.1010 | 0.2169 | 0.1084 | 0.0028 |
| 24.67% | 10.8942 | 7.9892 | 0.0931 | 0.1010 | 0.2118 | 0.1059 | 0.0027 |
| 26.10% | 11.1150 | 8.1072 | 0.0935 | 0.1021 | 0.2081 | 0.1040 | 0.0029 |

Where $r_n$, $r_w$, $r_{avg}$ are the estimate of the radius from the non-wetting fluid and the wetting fluid respectively, and $r_{avg}$ = ½($r_w$+$r_n$). All radii are given in lattice lengths. $\rho_w$ and $\rho_n$ are the wetting fluid density and the non-wetting fluids density respectively, $\Delta\rho$ is the density differences $\Delta P$ is the pressure difference, given in lattice pressure units.

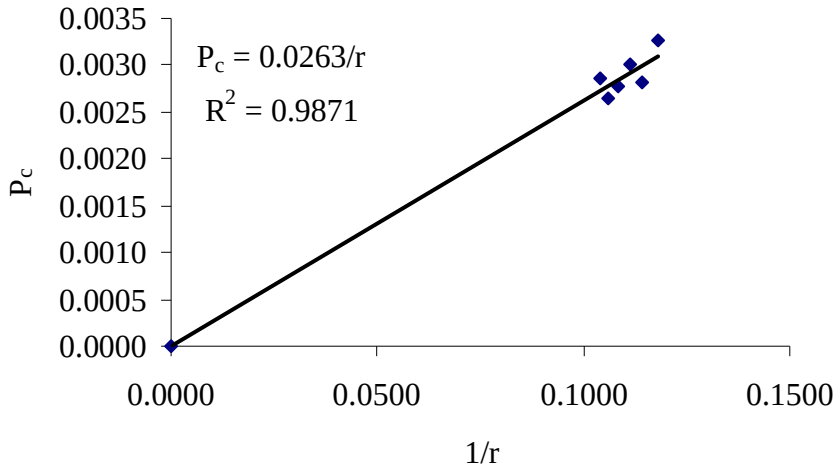


Fig C.5: Pc against 1/r where r = radius of the non-wetting sphere from the Laplace test when g = -1.0, $g_{ww}$ = $g_{nn}$ =0.

Table C.6: Table of results of the Laplace test when g = -1.05, $g_{ww}$= $g_{nn}$ = 0

| $S_{nw}$ | $r_w$ | $r_{nw}$ | $\rho_w$ | $\rho_n$ | $\Delta\rho$ | 1/r | $\Delta P$ |
|---|---|---|---|---|---|---|---|
| 17.15% | 9.8013 | 6.7074 | 0.0911 | 0.1007 | 0.0096 | 0.1211 | 0.0032 |
| 18.70% | 10.0846 | 7.0311 | 0.0915 | 0.1007 | 0.0093 | 0.1169 | 0.0031 |
| 20.23% | 10.3111 | 7.2557 | 0.0919 | 0.1011 | 0.0092 | 0.1139 | 0.0031 |
| 21.74% | 10.5738 | 7.4785 | 0.0923 | 0.1013 | 0.0090 | 0.1108 | 0.0030 |
| 23.21% | 10.7804 | 7.7950 | 0.0927 | 0.1011 | 0.0084 | 0.1077 | 0.0028 |
| 24.67% | 10.9210 | 8.0780 | 0.0931 | 0.1012 | 0.0081 | 0.1053 | 0.0027 |

Where $r_n$, $r_w$, $r_{avg}$ are the estimate of the radius from the non-wetting fluid and the wetting fluid respectively, and $r_{avg}$ = ½($r_w$+$r_n$). All radii are given in lattice lengths. $\rho_w$ and $\rho_n$ are the wetting fluid density and the non-wetting fluids density respectively, $\Delta\rho$ is the density differences $\Delta P$ is the pressure difference, given in lattice pressure units.

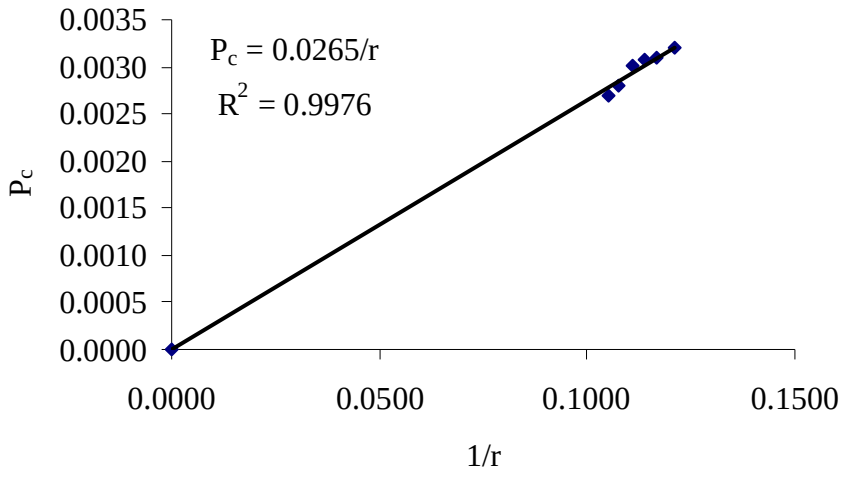


Fig C.6: Pc against 1/r where r = radius of the non-wetting sphere from the Laplace test when g = -1.05, $g_{ww}$= $g_{nn}$ = 0.

Table C.7: Table of results of the Laplace test when g = -0.7 and $g_{ww}$= 0.05, $g_{nn}$ = 0.

| $S_{nw}$ | $r_w$ | $r_{nw}$ | $\rho_w$ | $\rho_n$ | $\Delta\rho$ | 1/r | $\Delta P$ |
|---|---|---|---|---|---|---|---|
| 18.70% | 4.3623 | 2.9796 | 0.2276 | 0.2471 | 0.0195 | 0.2724 | 0.0065 |
| 20.23% | 4.4839 | 3.1169 | 0.2288 | 0.2473 | 0.0184 | 0.2631 | 0.0061 |
| 21.74% | 4.6534 | 3.2041 | 0.2299 | 0.2494 | 0.0196 | 0.2545 | 0.0065 |
| 23.21% | 4.7454 | 3.3447 | 0.2310 | 0.2499 | 0.0190 | 0.2472 | 0.0063 |
| 24.67% | 4.8487 | 3.4840 | 0.2321 | 0.2508 | 0.0187 | 0.2400 | 0.0062 |
| 26.10% | 4.9168 | 3.5951 | 0.2332 | 0.2505 | 0.0174 | 0.2350 | 0.0058 |

Where $r_n$, $r_w$, $r_{avg}$ are the estimate of the radius from the non-wetting fluid and the wetting fluid respectively, and $r_{avg}$ = ½($r_w$+$r_n$). All radii are given in lattice lengths. $\rho_w$ and $\rho_n$ are the wetting fluid density and the non-wetting fluids density respectively, $\Delta\rho$ is the density differences $\Delta P$ is the pressure difference, given in lattice pressure units.

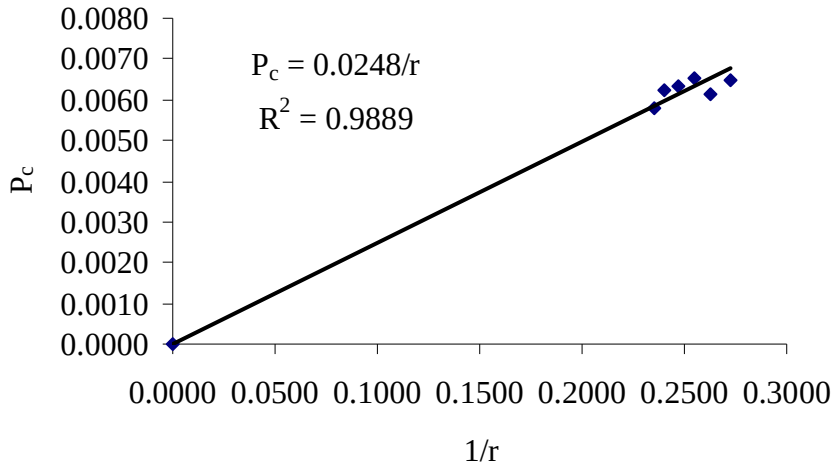


Fig C.7: Pc against 1/r where r = radius of the non-wetting sphere from the Laplace test when g = -0.7 and $g_{ww}$= 0.05, $g_{nn}$ = 0.